Novel Phases and Dynamical Phenomena in Frustrated Magnets

Preetha Saha

Noida, Uttar Pradesh, India

BS-MS Physics, 2015

Indian Institute of Science Education and Research,

Mohali, India

A Dissertation presented to

the Graduate Faculty of the University of Virginia

in Candidacy for the Degree of Doctor of Philosophy

Department of Physics

University of Virginia

November, 2021

ACKNOWLEDGEMENTS

Graduate school has been a tremendous experience. This wonderful journey would not have been possible without the continuous support and help from many people. I would like to take this opportunity to express my sincere thanks to these amazing people who have been by my side throughout my Ph.D.

My utmost gratitude goes out to my advisor, Gia-Wei Chern, for his support and guidance throughout my time at UVa. He provided me the opportunity to work on numerous challenging projects and gave me the freedom to pursue my work without pressure. He has been extremely patient and generous with his time in mentoring me.

I would like to thank my thesis committee members Bellave Shivaram, Seunghun Lee and Mona Zebarjadi for their valuable feedback. I would also like to thank Bellave Shivaram and Simonetta Liuti who have been a part of my research committee for the last four years. Their feedback and questions have helped me a lot. I would like to extend my gratitude to the Peter Cline, Dawn Shifflett and Bryan Wright for their help in navigating so many things throughout my time at UVA.

I want to thank my group members Jing Luo, Zhijie Fan, Depei Zhang, Puhan Zhang, Zhongzheng Tian and Sheng Zhang. We all shared the same office space and got to work on numerous collaborations. They have been great friends and I learnt a lot from them. Next I would like to mention Meng Hua, Siyu Jian, Rajveer Nehra and Sharon Philip whose friendship and solidarity made the graduate years so much enjoyable.

UVa provides us so many opportunities and cultural events to make friends outside of classrooms and departments. The friends I made here, I am going to cherish them for the rest of my life. Devanshi Gupta, Pallavi Patil, Abhiraj Deshpande, Abha Rajan and Sharmistha Sahoo deserve a special mention. The last 6 years have been truly memorable because of their presence. I couldn't have asked for better friends.

I am deeply grateful to my beloved parents Jayanti Saha and P.K. Saha and my brother Neil for their unconditional love and constant support. Thank you for always believing in me. I would not be where I am today without their encouragement and motivation to follow my dreams. I want to thank my other set of parents Neeru and Rajesh Aggarwal for continuously cheering on me.

Lastly this section is incomplete without mentioning my best friend and husband Aaveg Aggarwal. We met 12 years ago and got married in 2019. We started our undergrads together in India and then came to the US for our respective Physics PhDs. I am looking forward to accomplishing many milestones together. He has been my emotional and mental support through all sorts of up and downs. Everytime I had questions he was only a phone call away, patiently explaining me things. Thank you for always, always! having my back.

ABSTRACT

Frustrated magnets are a class of substances in which exchange interactions between neighboring spins (magnetic moments) cannot be simultaneously satisfied, leading to an extensive degeneracy in the ground state manifold. Frustration gives rise to many exotic phenomena, a prominent one being classical spin liquids (CSLs).

In this thesis we present an extensive numerical study on finding a new classical spin liquid in which the collective flux degrees of freedom break the translation symmetry of the honeycomb lattice. This exotic phase exists in frustrated spin-orbit magnets where a dominant off-diagonal exchange, called Γ term, results in a macroscopic ground-state degeneracy at the classical level. We demonstrate that the system undergoes a phase transition corresponding to plaquette ordering of hexagonal fluxes, driven by thermal order-by-disorder at a critical temperature $T_C \sim 0.04|\Gamma|$. We performed extensive Monte Carlo simulations and finite-size analysis to investigate the nature of the plaquette-ordering transition. We also study the dynamical behavior of fluxes and the influence of other types of interactions on the phase transition.

Next we have investigated the spin dynamics of a classical Heisenberg antiferromagnet with nearest-neighbor interactions on a quasi-two-dimensional kagome bilayer. This geometrically frustrated lattice consists of two kagome layers connected by a triangular-lattice layer. We combine Monte Carlo method with precessional spin dynamics simulations to compute the dynamical structure factor of the classical spin liquid and study the thermal and dilution effects. The low frequency and long wavelength dynamics of the classical spin liquid in kagome bilayer is dominated by spin diffusion. We discuss the implications of our work for the glassy behaviors observed in the frustrated magnet $SrCr_{9p}Ga_{12-9p}O_{19}$ (SCGO).

TABLE OF CONTENTS

LIST OF FIGURES

CHAPTER 1

INTRODUCTION

1.1 Overview

The earliest known reference to magnetism comes from 6^{th} century BC, when the Greek philosopher Thales of Miletus tried to explain the magical properties of lodestones (Fe_2O_3) which were known to attract iron and other lodestones. From there, the first documented use of lodestones in the form of compass is attributed to Shen Kuo in 1088. However, the study on the origins of magnetism flourished in the 18^{th} and 19^{th} century with the works by Gauss, Coulomb, Oersted, Ampére, Faraday and Maxwell. The modern understanding of magnetism originates from the work of Marie Curie and Pierre Weiss. While Curie investigated the effects of temperature on magnetic materials, Weiss developed a theory on magnetism based on the micromagnets in magnetic materials. This proceeded with the development of quantum mechanics in the 20^{th} century that laid the foundation for the theory of the motion and interactions of electrons in atoms. The present day understanding of the origins of magnetism is accredited to the theoretical models developed by Ernest Ising and Werner Heisenberg.

Magnetization in materials arise from two kinds of motions of electrons in atoms, one is the orbital motion of electron around the nucleus and other is the spin of the electron around its axis. The electron's orbital and spin motion individually bestow a magnetic moment on the electron causing it to behave as a tiny magnet. Isolated magnetic moments have a much different behavior than a collection of magnetic moments interacting with each other. This combined with the diversity of magnetic interactions present in real materials opens up the possibility of existence of a rich variety of phenomena. For example, localized magnetic moments get parallelly aligned in ferromagnets giving them an observable macroscopic moment. On the other hand, such ordering

is absent in ordered antiferromagnets, which is why they were discovered only in 1949 neutron diffraction measurement of MnO by Clifford Shull and Stuart Smart, long after the development of the microscopic theory of interacting spins by Louis Néel in the 1930's.

Today we have come a long way from the trivial antiferromagntic phenomenon. A very interesting and complex pattern can be illustrated on a triangular lattice housing Ising spins with antiferromagnetic exchange interactions. Two of the spins align themselves in anti-parallel directions to minimize the energy. However, it is impossible to align the third spin such that it minimizes the interaction energy with both the other spins concurrently. This is one of the simplest systems where we see a conflict in the correlations induced by the local interactions and the spatial geometry. Such an occurrence i.e. the absence of a unique ground state is termed as frustration particularly geometric frustration as it originates from the conflict between lattice geometry and spin interactions. It has been observed in the case of Kitaev-type models that frustration can also originate from highly anisotropic exchange interactions. Frustration often gives rise to many exotic phenomena, a prominent one being spin liquids.

The study of frustrated magnets and the search for both quantum and classical spin liquid systems in theory as well as experiments is an actively pursued field of research. Spin liquids may be understood as the study of disordered equilibrium states of spin systems, where the traditional magnetic long range ordered is suppressed due the presence of strong zero point fluctuations even at very low to absolute zero temperatures. Characterizing a spin liquid state emerging in strongly interacting spin systems and constructing the phase diagram requires a thorough manual study of the model. This makes it a very lucrative subject on two fronts. On the applications side, this subject sheds further light on the burgeoning field of identifying potential spin liquid candidates. On the fundamental understanding front, the different correlations and phases seen in frustrated magnets helps us organize their behavior in the variety of materials around us. As discussed above, the spin liquid state in conventional cooperative paramagnets emerges due to geometrical frustration or in the case of Kitaev-type models it originates from highly anisotropic exchange interactions. In

this thesis, I present the study of two very different types of spin systems that exist in the classical spin liquid state originating from the two above mentioned conditions. I have made an extensive search into their collective behavior evident in their correlation functions. Along with these, I have observed the dynamical response of these spin liquids using energy conserving Landau Lifshitz dynamics. Dynamic responses and correlations are usually probed directly in experiments like neutron scattering.

1.2 Thesis Layout

1.2.1 Theory of Frustration and Classical Spin Liquids

Chapter **2** contains a brief overview the origins of frustration in magnets, along with their properties and experimental signatures. These characteristics are elucidated using some of the most well known examples of classical spin liquids systems including the Kitaev model on a honeycomb lattice and antiferromagnetic Heisenberg interaction on both Pyrochlore and Kagome lattices.

1.2.2 Numerical Methods

Chapter **3** explains the details of the simulations and numerical methods. I have used Monte Carlo simulations to sample the degenerate ground state manifold of spin liquids. Here I have explained why and how we can apply the Monte Carlo simulations to these seemingly stochastic systems. I have also discussed the theory explaining precessional dynamics of the spins in presence of magnetic interactions using Landau Lifshitz dynamics.

1.2.3 Classical Spin Liquid System **I**: Off-diagonal Gamma interaction on a Honeycomb lattice

In chapter **4**, we report a new classical spin liquid in which the collective flux degrees of freedom break the translation symmetry of the honeycomb lattice. This interesting phase exists in frustrated spin-orbit magnets where a dominant off-diagonal exchange, called the Γ term, results in an extensive ground-state degeneracy at the classical level. We show that this phase transition corresponds

to plaquette ordering of hexagonal fluxes. We investigate the nature of the phase transition using Monte Carlo simulations and finite-size analysis. We also study the dynamical behavior of fluxes and the influence of other types of interactions on the phase transition. We employ Landau-Lifshitz dynamics to evaluate dynamical spin structure factor and study the excitations in this new classical liquid phase.

1.2.4 Classical Spin Liquid System **II**: Anti-Ferromagnetic Heisenberg interaction on a quasi-2D Kagome bilayer

In chapter **5** we study the spin dynamics of a classical Heisenberg antiferromagnet with nearest-neighbor interactions on a quasi-two-dimensional kagome bilayer. This geometrically frustrated lattice consists of two kagome layers connected by a triangular-lattice linking layer. By combining Monte Carlo simulations with precessional spin dynamics simulations, we investigate the dynamical structure factor, the diffusive behavior and the changes in these behaviors in a site-diluted system.

1.3 Publications

- Hidden Plaquette Order in a Classical Spin Liquid Stabilized by Strong Off-Diagonal Exchange. Phys. Rev. Lett. 122, 257204 (2019)
- Spin dynamics of the antiferromagnetic Heisenberg model on a kagome bilayer. Phys. Rev. B 103, 224402 (2021)
- Honeycomb-lattice Gamma model in a magnetic field: hidden Néel order and spin-flop transition. arXiv:2106.16121 (2021)
- Machine learning dynamics of phase separation in correlated electron magnets arXiv:2006.04205 (2020)

CHAPTER 2

ORIGINS OF MAGNETISM AND FRUSTRATION

This chapter describes the origins of magnetism in materials and frustration in magnets. Here I have discussed in detail about the characterization of spin liquids, their corresponding experimental signatures and their dynamical responses. I have concluded the theoretical overview with some famous examples of classical spin liquid systems.

2.1 Microscopic Origins of Local Magnetic Moments

2.1.1 Single electron spin and magnetic moment

Magnetization in materials arise from electron's orbital motion and its spin about it's axis. Both these motions independently bestow a magnetic moment on the electron causing it to behave as a tiny magnet. We known from Stern-Gerlach experiments that electrons carry a spin $\mathbf{S} = \frac{1}{2}$ and magnetic moment $\mathbf{m}$. For all cases presented in this thesis electron's spins are considered isolated from influence of the nuclei.

(a) Orbital motion magnetic moment:

Magnetic moment $\mathbf{m}$ is one of the most fundamental concept in magnetism. In the classical regime we can equate magnetic moment to a current carrying loop of wire as given in Figure 2.1.

A generalized equation for magnetic moment at distance $\mathbf{r}$ from the loop of current carrying wire [1] is depicted by the following equation,

$$\mathbf{m} = \frac{1}{2} \int \mathbf{r} \times \mathbf{j}(\mathbf{r}) \mathbf{d}^3 r \tag{2.1}$$

where $\mathbf{j}(r)$ represents the current density for a current I per unit area, at a distance r in space. This

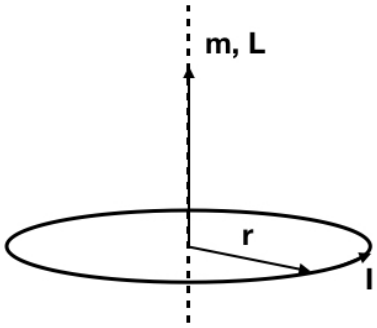

Figure 2.1: Magnetic moment produced by current carrying loop

can be rewritten as follows,

$$\mathbf{m} = \frac{1}{2}\int \mathbf{r} \times \mathbf{I}\mathbf{d}l = I\int d\mathbf{A} \tag{2.2}$$

As a result magnetic moment of the loop is given by $m = I\pi r^2$. When the given current is comprised of a charge *q* of mass *M* moving with velocity *v*, we can rewrite the orbital magnetic moment m_l generated by the dipole as follows,

$$\mathbf{m_l} = \frac{q}{2M}Mrv = \frac{q}{2M}\mathbf{L} = \frac{-e}{2M}\mathbf{L} \tag{2.3}$$

where, L represents the angular momentum. Thus the magnetic moment of an electron carrying loop is antiparallel to the orbital angular momentum. In quantum mechanics, the orbital angular momentum is quantized in units of $\hbar$, where we define the "Bohr magneton" μ_B as,

$$\mu_B = \frac{e\hbar}{2M} \tag{2.4}$$

and hence,

$$\mathbf{m_l} = -\mu_B\frac{L}{\hbar} \tag{2.5}$$

The orbital angular momentum $\mathbf{L}$ is given by, $\hbar\sqrt{l(l+1)}$ where l (= 0,1,2,....) represents the orbital quantum number.

(b) Spin magnetic moment:

Electrons carry a magnetic moment $\mathbf{m_s}$ and an intrinsic angular momentum $\mathbf{S}$, even when they move in a straight line or, are present in the atomic s-state (l=0). Classically origins of such intrinsic magnetic moment could be attributed to the spinning charged body. Similar to the orbital angular momentum L, S is given by $\hbar\sqrt{s(s+1)}$ where s represents the spin quantum number. The total angular momentum of atomic state is given by $\mathbf{J} = \mathbf{L} + \mathbf{S}$, which is essentially the sum of total orbital angular momentum and total spin angular momentum. But the total magnetic moment is given by $m = -\frac{\mu_B}{\hbar}\mathbf{L} + 2\mathbf{S}$.

In magnetic atoms with many electrons, the spin and orbital angular momentum couple due to spin orbit interactions like $\lambda\mathbf{L}\cdot\mathbf{S}$. As a result the total magnetic moment ($\mathbf{L} + 2\mathbf{S}$) can be expressed in the form of $\mathbf{J}$ as,

$$\mathbf{m_s} = -g_j\mu_B\frac{J}{\hbar} \tag{2.6}$$

where g_j is called the Landé g-factor,

$$g_j = 1 + \frac{j(j+1) + s(s+1) - l(l+1)}{2j(j+1)} \tag{2.7}$$

$g_j \approx 2$ for spin only (l=0) cases. The factor of 2 can be derived from relativistic Dirac quantum theory and $g_j = 1$ for pure orbital (s = 0) motion.

2.1.2 Magnetic moment in applied field

Induced magnetic field $\mathbf{B}$ is linearly related to applied magnetic field, $\mathbf{H}$ in vacuum as given by $\mathbf{B} = \mu_0\mathbf{H}$. Where $\mu_0 = 4\pi \times 10e - 7NA^{-2}$ is the permeability of free space. Magnetization $\mathbf{M}$ known as magnetic moment per unit volume is given by, $\mathbf{B} = \mu_0(\mathbf{H} + \mathbf{M})$. Magnetization is directly proportional to applied magnetic field in linear materials $\mathbf{M} = \chi\mathbf{H}$, where χ is a dimensionless quantity called susceptibility. As a result induced magnetic field can be rewritten as $\mathbf{B} = \mu_0(1+\chi)\mathbf{H} = \mu_0\mu_r\mathbf{H}$, where μ_r is the relative permeability of the material.

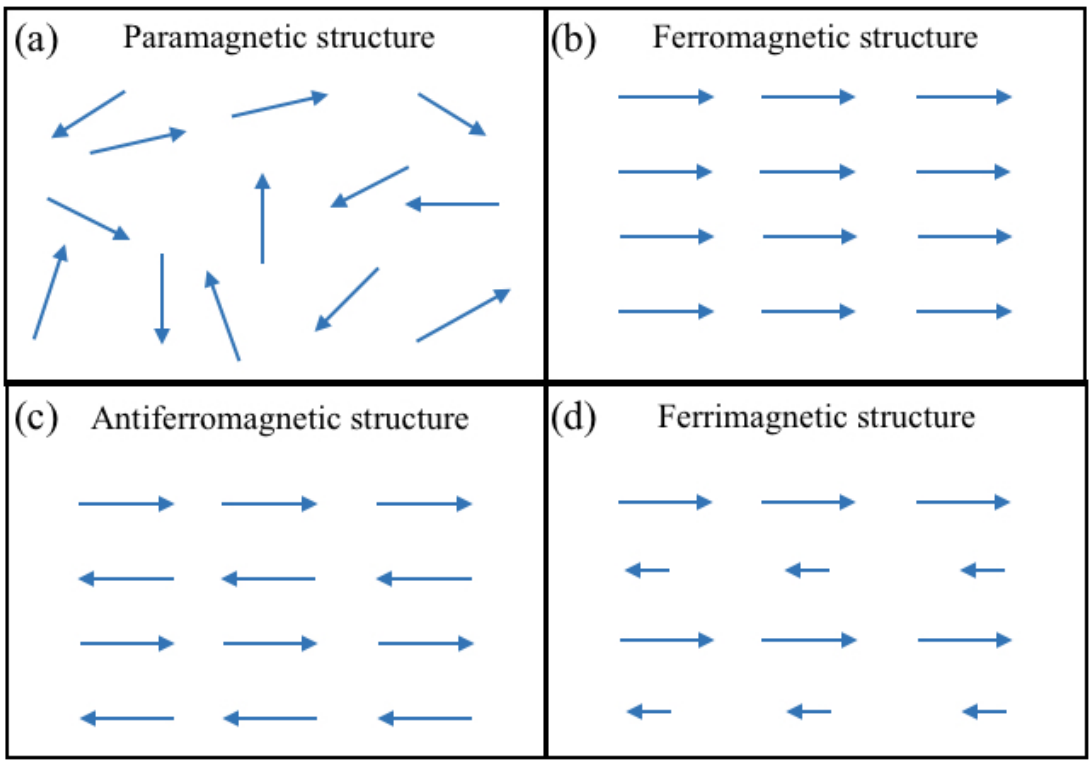

Figure 2.2: Different types of magnetic ordering (a) Paramagnetism, (b) Ferromagnetism, (c) Anti-Ferromagnetism and (d) Ferrimagnetism.

The energy of a material of magnetic moment μ in a field $\mathbf{B}$ is given by,

$$E = -\mu \cdot \mathbf{B} \tag{2.8}$$

The value depends on the relative direction of the magnetic moment w.r.t to the applied field.

2.2 Magnetic Interactions

The different kinds of interaction between magnetic moments, leads to a variety of ordered phases like ferromagnetism, anti-ferromagnetism and ferrimagnetism as shown in Figure 2.2. These interactions at the quantum scale are a result of electrons being indistinguishable and following Fermi Dirac statistics. Some of the examples of such interactions are,

Direct exchange: Orbital overlap between two atoms leads to correlation in their electrons. Such

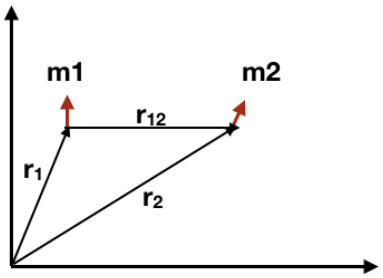

Figure 2.3: Dipole magnetization

an interaction is termed as direct exchange. Here Coulomb repulsion is minimum and electrons are spatially separated and antiparallel thus satisfying the Pauli's exclusion principle.

Superexchange: An interaction facilitated by intermediate ligand or anion is termed as a superexchange interaction. They are usually antiferromagnetic in nature. The nature of the interaction depends on the nature of the geometry and alignment of the orbitals. Such interactions are short ranged and limited within closest range of nearest neighbors.

Dipole-Dipole interaction In the regime of classical electromagnetism, dipole dipole interaction is a long range interaction.

$$m = -\frac{\mu_0}{4\pi|\mathbf{r_{12}^3}|}(3(\mathbf{m_1}\cdot\hat{\mathbf{r_{12}}})(\mathbf{m_2}\cdot\hat{\mathbf{r_{12}}}) - (\mathbf{m_1}\cdot\mathbf{m_2})) \tag{2.9}$$

The energy diminishes rapidly as a function of $1/r_{ij}^3$. Atomic distances are at the scale of $\mathring{A}$ and the energy scales are in the range of 10^{-4} eV. These energy scales are much smaller than inter-atomic interaction energies. We see the effects of dipole dipole interaction at very small temperatures $(T < 1K)$. Most known magnetic ordering occurs at much higher temperatures of $T > 300K$, by effective coupling of neighbouring ions from quantum effects emanating from exchange interactions.

2.3 Magnetic Ordering: Collective Magnetic Structures

As discussed dipole-dipole interaction between the magnetic moments of electrons is too weak [2] to explain magnetic order at high temperatures. Origin of the interactions that causes the neighboring magnetic dipoles to affect each other's orientation comes from the interplay of Coulomb interaction and Pauli's exclusion principle. The magnetic materials are further classified to into types based on their response to external magnetic field and the relative orientation of the spins in different temperature regimes.

Diamagnetism

Diamagnetism is a property of all materials. Its contribution to the material's response in a magnetic field is negligible. In diamagnetic materials all electrons in the outer orbit are paired. As a result, they have a zero net magnetic moment. In presence of an applied magnetic field, the induced magnetic field (magnetization **M**) is in the opposite direction of the applied field causing a repulsive force. Figure 2.4 for magnetization with external field **H** shows a negative susceptibility. Susceptibility in diamagnetic materials is independent of temperature T.

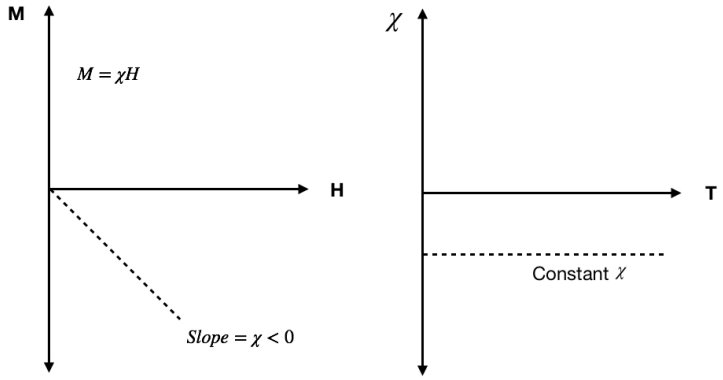

Figure 2.4: Magnetization and Susceptibility in Diamagnetic materials

Paramagnetism

Paramagnetism in materials originates form partially filled orbitals. As a result they have a net magnetic dipole moment and act as tiny magnets, see Figure 2.2(a). These dipole moments do not

interact with each other. In an external magnetic field the electron spins partially align themselves parallel to the applied field resulting in a positive magnetization and positive susceptibility, thereby causing a net attraction force.

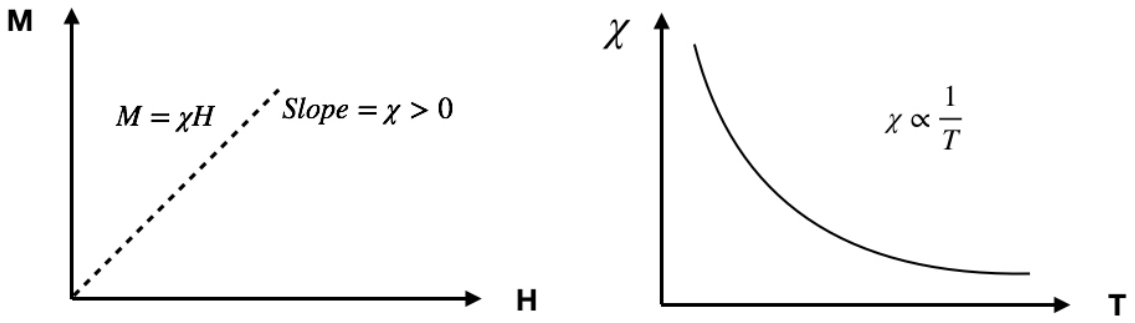

Figure 2.5: Magnetization and Susceptibility in Paramagnetic materials

At sufficiently high temperatures, the thermal energy can disturb the magnetic dipole alignment of the spins. This means susceptibility depends on temperature. The relation between susceptibility and temperature is given by Curies's law, where susceptibility is inversely proportional to the absolute temperature as shown in Figure 2.5.

Curie's Law :

$$\chi = \frac{N_A g_j^2 \mu_B^2}{3k_B T} J(J+1) \tag{2.10}$$

Where N_A is the Avogadro's number, k_B represents the Boltzmann constant and J represents the total angular momentum.

Ferromangetism

Atomic moments in ferromagnets strongly interact with their neighboring moments as opposed to those in paramagnets. Their respective electronic exchange interactions result in parallel or antiparallel alignment of atomic moments, see Figure 2.2(b). These exchange forces are of the order of 1000 Tesla. Magnetic fields are quantum mechanical in nature due to the relative alignments of electron spins. In Ferromagnetic materials the atomic moments parallelly align resulting in a high net magnetization. Susceptibility is large and consequently magnetization increases massively

with applied field **H** intensity. Despite very large electronic exchange forces in ferromagnets, at higher temperatures, thermal energy eventually overcomes the exchange interaction energy and produces a randomizing effect and the material starts exhibiting paramagnetic behavior. The transition temperature is called the Curie temperature (T_C). Curie-Weiss law describes the behavior of the ferromagnets in the paramagnetic regime.

Curie-Weiss Law:

$$\chi = \frac{C}{T - \theta_W} \tag{2.11}$$

where C represents the Curie constant given by $C = N_A\mu^2/3k_B$, with μ given by $\mu = g_J\sqrt{J(J+1)}\mu_B$. θ_W is the Weiss constant, with same dimensions as that of temperature. For $\theta_W > 0$ magnetic interactions in the material lies in the ferromagnetic regime, whereas for $\theta_W < 0$ magnetic interactions are antiferromagnetic in nature. $\theta_W = -T_N$ represents the Néel temperature.

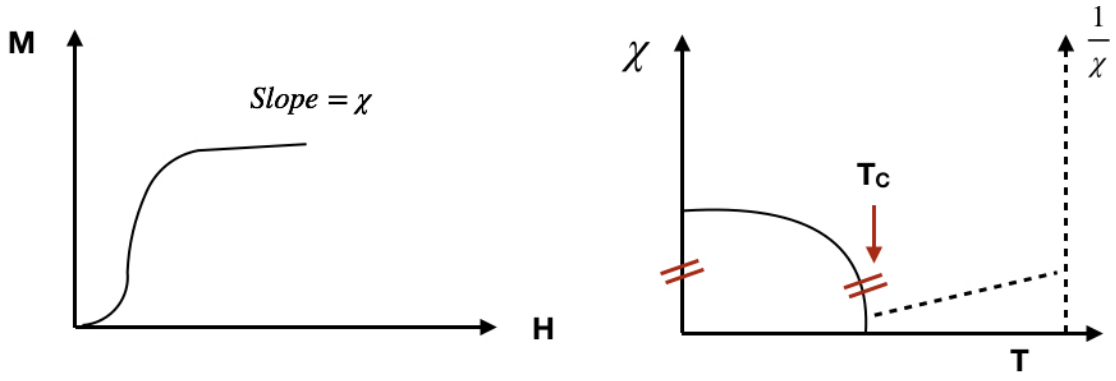

Figure 2.6: Magnetization and Susceptibility in Ferromagnetic materials. It behaves as a paramagnet above Curie temperature T_C.

Antiferromagnetism

Antiferromagnets behave like paramagnets above a critical temperature called Néel temperature T_N, but with a negative intercept indicating negative exchange interactions. Below T_N the susceptibility is small, where the temperature dependence is very different from paramagnets as shown in Figure 2.7. In an antiferromagnetic material if there are two sublattices A and B, the moments

align themselves opposite to each other such that the net moment is zero, see Figure 2.2(c).

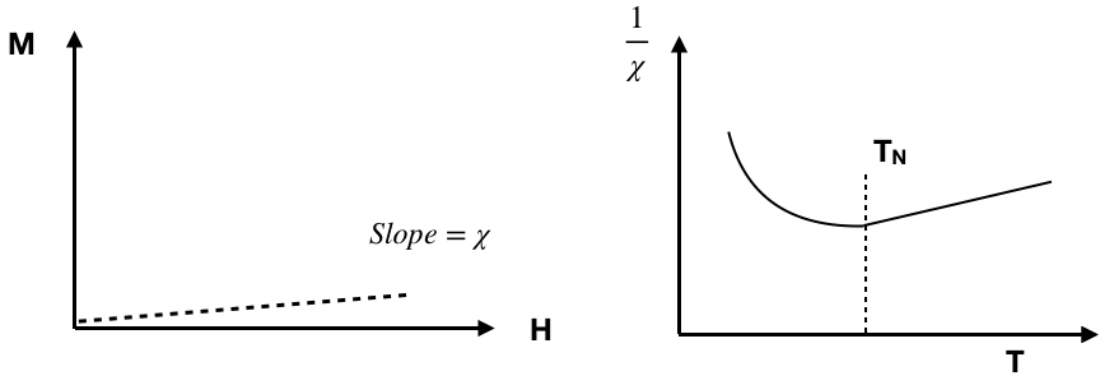

Figure 2.7: Magnetization and Susceptibility in antiferromagnetic materials. Susceptibility is small below T_N

Ferrimagnetism

In ferrimagnetic materials, if there are two sublattices A and B, the moments align themselves opposite to each other such that there exists a net moment, see Figure 2.2(d). As a result they behave similar to ferromagnets including spontaneous magnetization, hysteresis, Curie temperature behavior etc, but with a different magnetic ordering and smaller effects. The $1/\chi$ values are almost negligible below the critical temperature called Neél temperature T_N.

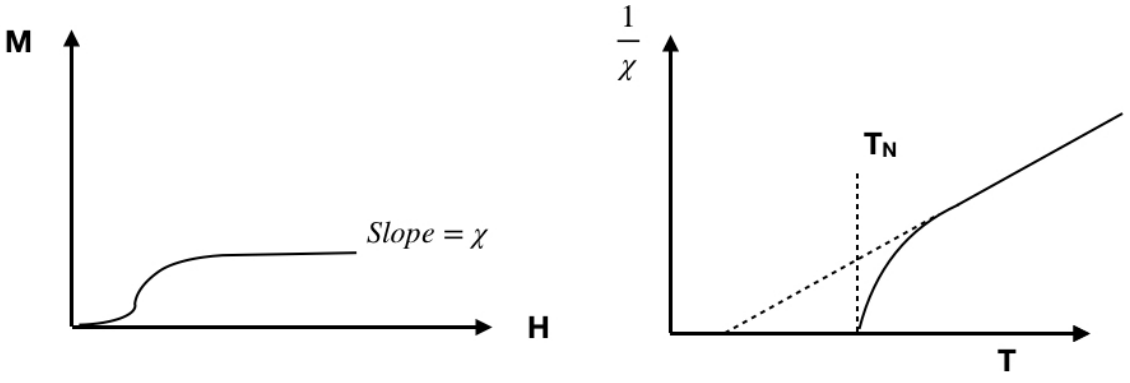

Figure 2.8: Magnetization and Susceptibility in in Ferrimagnetic materials. $\frac{1}{\chi}$ is very close to zero below the Néel temperature.

2.4 Frustration

As we saw in the previous sections, magnetic interactions often lead to ordering in a system. Thermal fluctuations at high temperatures above a certain critical temperature T_C can break ordering and project the system into a paramagnetic state. However, fluctuations can also have different origins that lead to destruction or repression of order, that consequently contributes to frustration in a system.

In the field of magnetism the word frustration was first introduced to describe the impossibility of simultaneously satisfying all competing exchange processes between localized magnetic moments or spins [3]. This leads to macroscopic degeneracy in ground state configurations. This may lead to formation of fluid like states of matter called spin liquids. Degeneracy is considered to be a defining trait of frustration.

The word fluctuation refers to random reorientation of the spin with time. These can be thermal or quantum in nature. Classical spins are identified as spins with larger magnitude($S >> \frac{1}{2}$). In the classical regime, the thermal excitations drive the spins to move around in the degenerate ground state configurations. At very low temperatures T and consequently at low energies K_BT classical fluctuations die away and the spins freeze or reach an ordered state. For very small spins $S \sim \frac{1}{2}$ fluctuations fall under the quantum regime where the uncertainty principle produces zero-point motion which perseveres down to $T = 0K$. Quantum fluctuations result in a state called quantum spin liquid which is a superimposed state in which spins point in multiple directions at the same time. In summary fluctuations in spin liquids persists down to absolute zero temperature. In spite of the persisting frustration, constituent spins in a spin liquid are highly correlated as their movement is restricted inside the the ground state manifold.

The term spin liquid is coined to draw an analogy between the different phases of matter and states of magnet. For example a paramagnet which occurs at higher temperatures with uncorrelated constituent spins can be related to the gaseous phase of matter. Similarly at low temperatures Néel state can be represented as analogous to solid state of matter in relation to the broken isotropic

symmetry, distinguished by a local order parameter and existence of long range order. Following the same trend, we expect that local correlations in spin liquids similar to their classical fluid counterparts. However as we will observe spin liquids exhibit far more interesting features and long range correlation behaviors.

Frustration in antiferromagnets usually have simple geometric origins like triangular lattices where it is impossible to have a single unique minimum energy configuration with anti aligned Ising spins satisfied for each neighboring pair of spins. Whereas more exotic Hamiltonians with anisotropic exchange interactions between nearest neighbor spins can also contribute to the degeneracy in ground states and thereby frustration in the system like well know Kitaev Model on the Honeycomb lattice [4]

Research has shown that solid state materials known as Mott insulators are great candidates for the presence of spin liquids states. With the presence of high spin orbit coupling the electrons in them are the localized to the individual atomic or molecular orbitals.

2.5 Geometric Frustration

Geometrically frustrated magnets, the term coined by Ramirez [5] are a class of materials that exhibit frustration effects originating from the contradiction between the lattice geometry and energy minimizing long range magnetic order. A lattice is a collection of sites housing the spins connected to each other by bonds (exchange interactions).

In this section we see the effect of antiferromagnetic exchange interaction between Ising spins on two types of lattices, bipartite lattices and lattices formed by triangular motifs called simplex structures. A lattice is bipartite when it can be divided into sublattices such that spins in one sublattice only interacts with the spins in the other sublattice and simplexes are defined as a unit of three spins on a triangular lattice or a unit of four spins forming a tetrahedron on a corner sharing three dimensional lattice. Properties of Ising antiferromagnets on simplexes, in triangular or tetrahedral lattices differ from their counterparts on bipartite lattices (cubic, honeycomb etc).

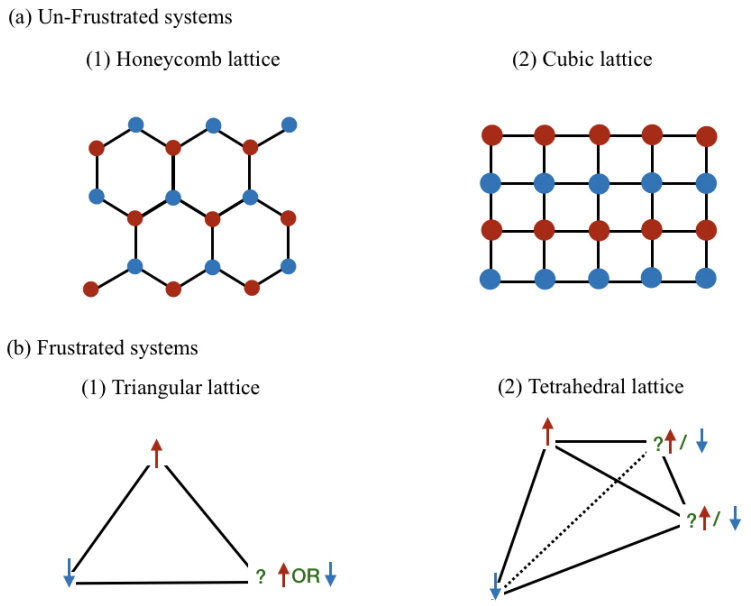

Figure 2.9: Frustration: Ising spins with antiferromagnetic nearest neighbor interaction (a) Unfrustrated (1) honeycomb and (2) square lattice. (b) Frustrated systems: (1) Triangular lattice: 6 equivalent ground state configurations. (2) Tetrahedral lattice: 6 equivalent ground states

As depicted in Figure 2.9, we have several examples of lattices where the nearest neighbor Ising spins on each of the lattices experience antiferromagnetic exchange interaction. Anti-parallel alignment of the adjacent spins minimizes the energy of each bond. The spins on the bipartite lattices as shown in Figure 2.9 (a) can get ordered in a Néel state [6], thus giving rise to a long range ordered unfrustrated system with one unique ground state. Whereas in the triangular and tetrahedral lattices, formation of Néel state is not possible. We see in Figure 2.9 (b)-(1), all three pairs of spins on the triangular simplex cannot be simultaneously antiparallel and we end with 6 equivalent ground state configurations. In Figure 2.9 (b)-(2) we can observe a similar frustration effect in the three dimensional system of four antiferromagentic Ising spins on a tetrahedron. There are 6 degenerate ground state configurations. Each minimum energy state consists of 2 spins pointing up and 2 spins pointing down, such that for each state we have 2 satisfied bonds (antiparallel spins) and 1 unsatisfied bond (parallel spins). On two dimensional and three dimensional systems (with simplex building blocks), these degeneracies keep multiplying and lead to large scale frustrated

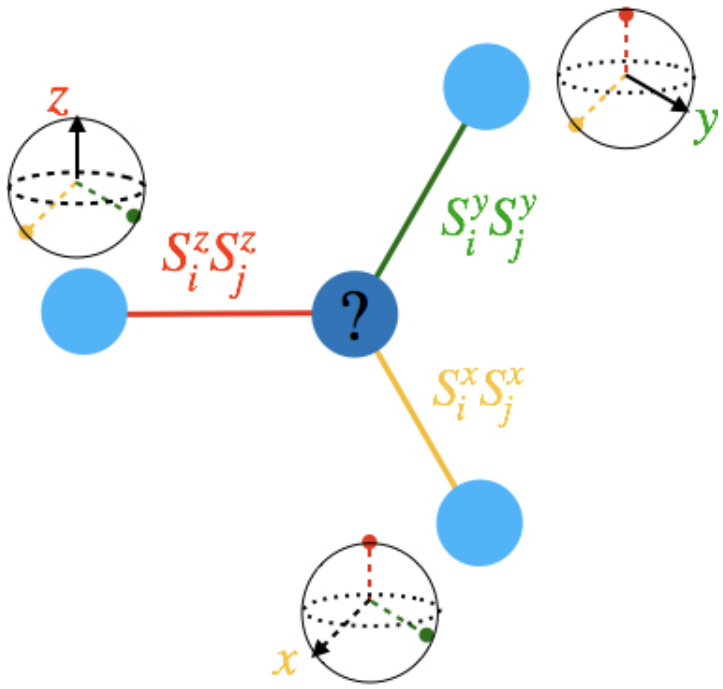

Figure 2.10: Spin Orbit facilitated anisotropic bond directional exchanges. Here the exchange interaction depends on the spatial orientation direction of the bond. The spins cannot orient amongst themselves to simultaneously minimize all interactions, thus gicing rise to frustration.

systems with intensified fluctuations and repressed magnetic ordering.

2.6 Frustrated Magnetism from Anisotropy in Exchange Interactions

Instead of frustration originating from lattice geometry, anisotropy in exchange interaction can also contribute to frustration in a system. An example of such an interaction is shown in Figure 2.10, where Ising spins have ferromagnetic exchange interaction. Spin exchange energies are dependent on spatial directions of the bonds along the orthogonal axes and cannot all be satisfied simultaneously, thus leading to a frustrated system. Kitaev materials are famous examples of such frustrated system .

2.6.1 Spin-orbit interaction driven Mott insulators

Partially filled 4^d and 5^d shells in transition metal oxides lead to very interesting interactions between spin, electronic and orbital degrees of freedom. These interplay appear as a result of spin

orbit interactions, crystal field effects and electronic correlations [7]. Every material may vary in its bias towards the stronger effect exhibited by any of the above three different kinds of interactions. Mott insulators have local magnetic moments arising from high spin orbit coupling, which collectively give rise to unconventional phases in magnetic materials, including spin liquid states. Experimentally **j = 1/2** Mott insulators[8] that exhibit bond directional exchange interactions are good likely candidates to look for spin liquids, as the electrons are localized and isolated to their atomic or molecular orbitals and maintain their spin degrees of freedom.

2.6.2 Bond directional exchange interactions

All Kitaev materials represent a class of materials containing bond directional exchange interactions, which dominate over all other coupling exchange energies. These interactions are much similar to the interaction shown in Figure 2.10 where we see direction dependent Ising interactions. Like geometric frustration, anisotropic exchange interaction leads to frustration arising from bonds that cannot be simultaneously satisfied. These further contribute to inhibit magnetic ordering and consequently degeneracy in ground states, that gives rise to a phase called spin liquid. For example, the classical Kitaev model on the honeycomb lattice does not undergo any phase transition at finite temperatures [9, 10], however it exhibits an extensively degenerate ground state manifold at absolute zero temperature [11].

The microscopic origins of the bond directional exchange interactions in $\mathbf{d^5}$ transitional metals has been extensively studied by Khaliullin [12] and later for Kitaev materials specifically by Jackeli and Khaliullin [13]. The Hamiltonian describing the interactions in Kitaev materials that includes several terms between magnetic moments in Mott insulators (**j = 1/2**), is given by the following equation,

$$\mathcal{H} = -\sum_{\gamma-bonds} J\mathbf{S}_i\mathbf{S}_j + K\mathbf{S}_i^{\gamma}\mathbf{S}_j^{\gamma} + \Gamma(\mathbf{S}_i^{\alpha}\mathbf{S}_j^{\beta} + \mathbf{S}_j^{\alpha}\mathbf{S}_i^{\beta}) \tag{2.12}$$

where the summation is over all nearest neighbor spins forming the bonds $\langle i, j\rangle$, along the di-

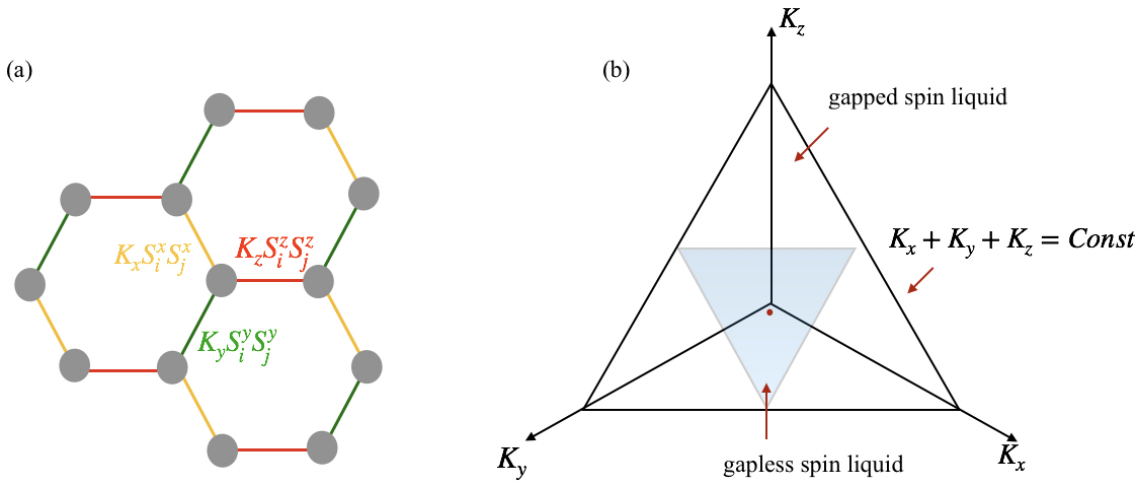

Figure 2.11: (a) Kitaev Model with K_x, K_y and K_z interaction strengths along the 3 different bonds. (b)Schematic phase diagram of the Kitaev model. Depending on the relative strength of the interaction constants, the matter fermion excitations either form gapped spin liquid phase or a gapless spin liquid phase(blue shaded region). The gapless phase emerges around the red point of isotropic interactions $K_x = K_y = K_z$.

rections where each bond direction is represented by $\gamma = (\mathbf{x}, \mathbf{y}, \mathbf{z})$. The Heisenberg exchange interaction strength is given by **J** and the bond-directional interactions include two terms with **K** representing the strength of Kitaev interaction, where the γ components of the nearest neighbor spins interact with each other along a γ-bond and $\mathbf{\Gamma}$ represents the strength of the off diagonal exchange between nearest neighbors. The relative strengths for the interactions vary in materials. For Kitaev materials like **j = 1/2** Mott insulators, we have $K > J, \Gamma$ and $|K/J| \sim 4$. In this thesis, I present the study of the pure Gamma model, with $\Gamma = 1$ and $J = K = 0$, where we see the emergence of a unique classical spin liquid phase.

2.6.3 Kitaev model

The pure Kitaev model consists of nearest neighbor spins coupled in bond directional interactions exchanges given by the following Hamiltonian.

$$\mathcal{H}_{Kitaev} = -\sum_{\gamma-bonds} K_\gamma \mathbf{S}_i^\gamma \mathbf{S}_j^\gamma \tag{2.13}$$

The spin $\mathbf{S = 1/2}$ model as studied by Alexei Kitaev is defined on a honeycomb lattice as shown in Figure 2.11(a). It is also a rare microscopic model that is exactly solvable using fermionisation procedure, where spin 1/2 moments are expressed in terms of Majorana fermion operators [4]. In the honeycomb lattice, we can see one spin engaged in three kinds of bonds. It is very evident that the system is frustrated from the anisotropic interaction exchanges, such that it is impossible for a spin at one site to simultaneously satisfy three different energies on three different bonds. The model contains both gapped and gapless spin liquid phases, depending on the relative strength of the coupling interactions of the three bond types, see Figure 2.11. The Majorana fermions exist in a gapless state called *Majorana metal* near the point of equal interaction strength in the three different bonds($K_x = K_y = K_z$). In a honeycomb lattice with Kitaev interaction this Majorana metal state is a semi metal state displaying Dirac cone dispersion. On the other hand if one of the interaction exchanges is dominant, e.g. K_z along the line $K_z = K_x + K_y$, a new gapped spin liquid phase emerges. There is an active pursuit for Kitaev materials in lieu of synthesising new spin liquid materials. A classical variant of the model with additional terms, like a Heisenberg-Kitaev model has also been extensively studied [10, 14–16].

2.7 Properties of Frustration

This section highlights some of the common traits exhibited by frustrated magnetic systems.

2.7.1 Ground state degeneracy

Extensive ground state degeneracy is an identifying trait in frustrated magnets. The existence of degeneracy is not a consequence of symmetry. The degree of degeneracy varies with different geometries and different natures of spins (Ising, Heisenberg). An Ising spin as discussed above has 2 states (+ve or -ve) and we get a discrete number of ground states, whereas a Heisenberg spin can take any direction in the three dimensional space, as a result we have continuous degrees of freedom within the ground state manifold. We saw in the previous section that a lattice is composed of a cluster of spins called simplexes. In 2 dimensional systems like triangular or

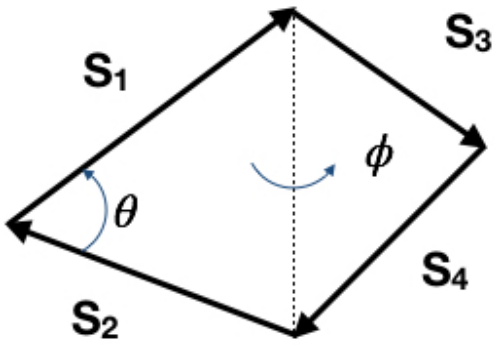

Figure 2.12: A ground state configuration with zero total magnetic moment for a frustrated simplex of four classical Heisenberg spins

kagome lattices the simplexes are triangles, whereas in a pyrochlore lattice the simplex structure is a tetrahedron. Intuitively, minimizing the energy of each unit separately should give us a minimum energy configuration of the whole lattice.

$$\mathcal{H} = J \sum_{<ij>} \mathbf{S}_i \mathbf{S}_j = \frac{J}{2} \sum_{\alpha}^{N_\alpha} \mathbf{L}^2 + \text{const.} \qquad \text{where } \mathbf{L} = \sum_{i=1}^{q} \mathbf{S}_i \tag{2.14}$$

Let say we have a Heisenberg interaction between spins given by equation 2.14. This can be rewritten in terms of the sum total of squares of the net magnetization of spins of each simplex given by $\mathbf{L}_\alpha$, where q represents the numbers of spins on a simplex and N_α is the number of simplexes in the lattice. For $J < 0$ (antiferromagnetic interaction), having the net magnetization $\mathbf{L}_\alpha = 0$ for each simplex gives us the energy minimizing condition for the whole lattice. For simplexes with spins $q > 2$, it becomes impossible to minimize the interaction ($J\mathbf{S}_i\mathbf{S}_j$) between all pairs simultaneously. For example, in a system with antiferromagnetic interaction between Heisenberg spins on a tetrahedron simplex, the ground state condition is given by $\mathbf{L} = \sum_{i=1}^{4} \mathbf{S}_i = \mathbf{S}_1 + \mathbf{S}_2 + \mathbf{S}_3 + \mathbf{S}_4 = 0$. The Figure 2.12 represents an arrangement of spins such that the net moment is zero. There can be many different ways to achieve this ground state constraint. Overall the system possesses two internal degrees of freedom θ and ϕ and three rotational degrees of freedom due to the symmetry of the Hamiltonian. To scale this circumstantial existence of ground state degeneracy from a simplex structure to an extended lattice, we enumerate the degrees of

freedom (d.o.f) in the system [17, 18]. The d.o.f in a ground state configuration *D* are given by subtracting all energy minimizing constraints *K* from the total degrees of freedom *F*. Each spin has $F = N_S(d-1)$ degrees of freedom, d is the dimension of each spin and N_S is the total numbers of spins. If q spins form a corner sharing cluster or a simplex, the number of clusters N_C is given by $N_c = \frac{2N_S}{q}$. The ground state constraint of $L_\alpha = 0$ gives $K = dN_C$. We can solve for D by satisfying these constraints simultaneously provided they are linearly independent.

$$D = F - K = [\frac{q}{2}(d-1) - n]N_C \tag{2.15}$$

For Heisenberg spins with $d = 3$ and $q = 4$, We have $F = 2N_S$. Then the number of degrees of freedom in the ground state manifold are $D = F - K = N_C = \frac{N_S}{2}$. In summary, D is extensive.

2.7.2 Experimental signatures of frustration

We learnt in the preceding sections that, frustration leads to extensive degeneracy in ground states which in turn prevents long range ordering or reduces it even at very low temperatures. Experimentally, we can see the presence of frustration while measuring temperature dependence of magnetic susceptibility [5]. Susceptibility χ is defined as the ratio of magnetization w.r.t the strength of applied magnetic field. χ at higher temperatures is given by the Curie-Weiss law eq 2.16, where θ_{CW} determines the energy scale of magnetic interactions. $\theta_{CW} > 0$ in ferromagnets and $\theta_{CW} < 0$ in antiferromagnets. The system exists in a paramagnetic phase for temperatures $T > \theta_{CW}$. In an antiferromagnetic system in absence of frustration, we observe a phase transition from paramagnetic state to long range ordered at Néel state. The onset of Néel order appears at temperature $T_N \sim |\theta_{CW}|$. Whereas in a frustrated phase, the ordering either doesn't happen or the system remains paramagnetic upto very low temperatures $T_N << |\theta_{CW}|$.

$$\chi = \frac{1}{T - \theta_{CW}} \tag{2.16}$$

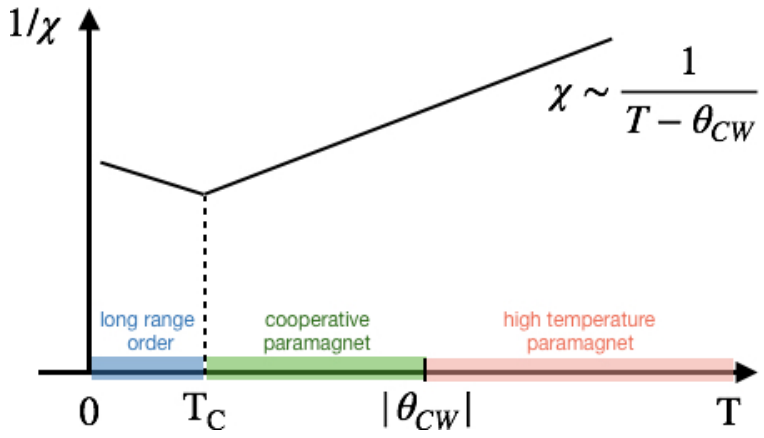

Figure 2.13: Experimental χ characteristics of geometrically frustrated systems

We define T_C as the transition temperature at low temperatures for any kind of ordering or freezing. Then the ratio f [5] gives us a measure of the extent of frustration.

$$f = -\frac{|\theta_{CW}|}{T_C} \tag{2.17}$$

A frustrated system in the range of temperatures $\theta_{CW} > T > T_C$ exists in a strongly fluctuating but correlated state called *cooperative paramagnet* [19] or a “spin liquid". In an ideal spin liquid where there is no ordering even at $T = 0K$, the ratio f indicates the degree of frustration is infinite.

2.7.3 Order-by-disorder

The word fluctuation denotes changes in spin configuration that deviates it from the ground state. Zero mode refers to frequencies in which fluctuations are within harmonic approximation around a ground state configuration. While soft modes refers to non zero frequencies with higher order (anharmonic) orthogonal fluctuations.

In frustrated magnets, where the degeneracy is not a consequence of symmetry, the fluctuation spectrum around each ground state varies. It is highly probable for ground states with smallest excitation frequency and high density of soft modes around it to be selected, because such states are characterized with minimal energy and highest entropy. As a result in presence of fluctuations

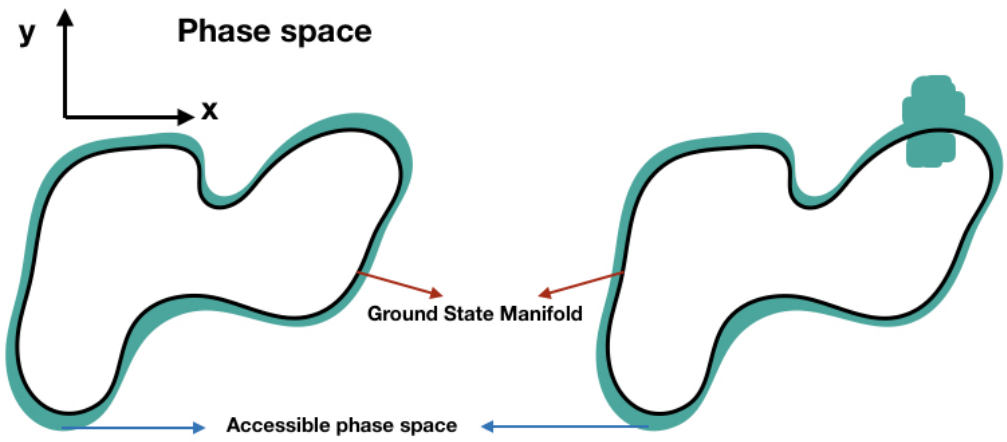

Figure 2.14: Schematic view of the phase space. X and Y represent the coordinates parallel and perpendicular to the black curve that represents the ground state manifold

instead of suppressing order, the system is inclined to stay near a ground state with largest number of soft modes, thereby promoting an ordered configuration, a phenomenon referred to as order-by-disorder [20, 21].

We can understand order-by-disorder from Figure 2.14. On the left side we have a schematic representation of the phase space. The solid line in black represents the ground state manifold. A narrow band in color around the ground state manifold represents the accessible states at low temperatures. Similarly on the right we have the same conventions representing the accessible ground state manifold. Here some of the accessible states are concentrated in a bulge with high density of soft modes and rest of them are distributed around the ground state manifold. When the fluctuations select the ground states near the bulge, we see order-by-disorder that can be tested using Monte Carlo simulations.

2.7.4 Ground state correlations in frustrated magnets and pinch points

Geometrically frustrated magnets like classical Heisenberg model on a Pyrochlore lattice do not undergo order-by-disorder and move around in the entire ground state manifold. We find that the fluctuations in the ground state manifold lead to long range correlations amongst the ground states of frustrated magnets. The existence of long range interactions between the ground states sounds

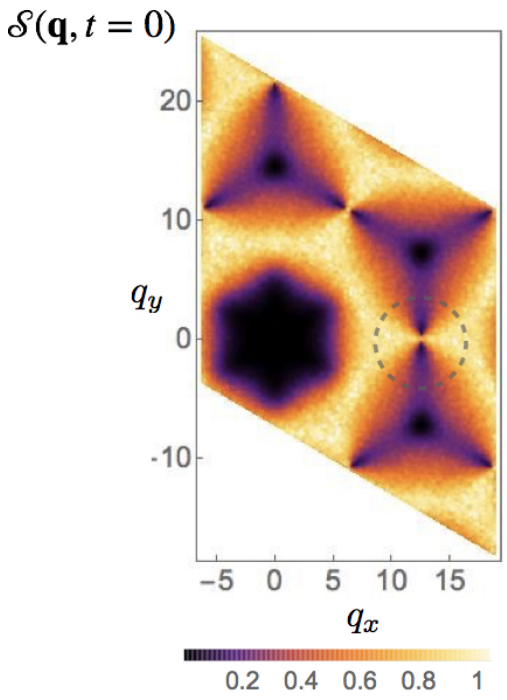

Figure 2.15: Pinch point (denoted by the circle) observed in a dynamic correlation function in an antiferromagnetic Heisenberg system in a quasi-2D Kagome bilayer lattice

counter intuitive because of the presence of large number of ground state degrees of freedom. But it has been observed that there are indeed long range correlations in models with bipartite lattices[18], like in the pyrochlore lattice. At finite temperatures thermal fluctuations out of ground state manifold have a correlation length ξ. The value for ξ at low temperatures varies as $\xi \sim T^{1/2}$ in a Heisenberg model and exponentially in an Ising model. These correlations give rise to sharp features, termed as pinch points in the reciprocal space correlation functions. The source of these singularities can be attributed to the ground-state constraints Eq. (2.14), which translates into a solenoid condition $\nabla \cdot \mathbf{B} = 0$ for an emergent “magnetic" or flux field that is a coarse-grained representation of the spin configuration. This in turn gives rise to an anisotropic dipolar-like correlation of the flux field, which manifests itself as the pinch-point singularity in the reciprocal space [22–24].

We can measure reciprocal space correlations in diffusion neutron scattering experiments where the partial cross section is directly proportional to the spin-spin correlations (section 2.10). The

pinch point features distinguishes the diffraction patterns of frustrated system from a paramagnet and are relatively weaker than the Bragg peaks arising from Néel order. One such example of pinch points is observed in a spin-spin correlation in momentum space defined by dynamic correlation function ($S(\mathbf{q}, t)$), see Eq. 2.18. We have an instance of the dynamic correlation function at time $t = 0$ in an antiferromagnetic Heisenberg system, in a quasi-2D Kagome bilayer lattice given in Figure 2.15 that clearly shows the sharp pinch point features.

$$\mathcal{S}(\mathbf{q}, t) = \langle \mathbf{S}_{\mathbf{q}}(t) \cdot \mathbf{S}^*_{\mathbf{q}}(0) \rangle \tag{2.18}$$

where $\mathbf{S}_{\mathbf{q}}(t) \equiv \sum_i \mathbf{S}_i(t) \exp(i\mathbf{q} \cdot \mathbf{r}_i)/\sqrt{N}$ is the spatial Fourier transform of the instantaneous spin configuration, and $\langle \cdots \rangle$ denotes the ensemble average over independent initial states of a given temperature. At finite temperatures the width of the pinch points are inversely proportional to the correlation length.

2.8 Examples of Geometrically Frustrated Systems

Some very well known examples of frustrated magnetic lattices with 2D and 3D triangular motifs.

1. Triangular lattice

A ground state in a triangular lattice with Heisenberg antiferromagnetic interactions between spins must satisfy the condition given by Eq. 2.14, i.e. energy minimization requires

$$\sum_{i \in \triangle} \mathbf{S}_i = 0 \tag{2.19}$$

This condition manifests into a ground state called "$\sqrt{3} \times \sqrt{3}$" depicted in Figure 2.16. In this particular ground state, the lattice can be described as a composition of three different sublattices with a lattice constant $\sqrt{3}$ times the lattice constant of the original lattice. A system is called

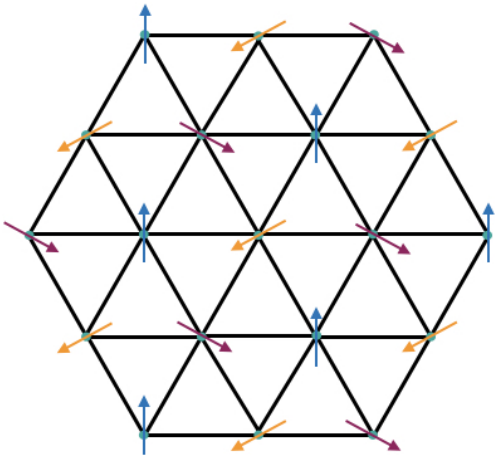

Figure 2.16: $\sqrt{3} \times \sqrt{3}$ Ground state in a Triangular lattice

frustrated in the presence of extensive degeneracy of ground states. Our next step is to check the degeneracy in the $\sqrt{3} \times \sqrt{3}$ state shown in Figure 2.16.

In a generic ground state, every spin on any triangular simplex in the lattice is at 120° degrees to each other and lie on the same plane to satisfy the constraint in Eq. 2.19. In a minimum energy configuration, the spins on the entire lattice are universally coplanar and fixing the spins on one triangle, uniquely determines all the spins on the lattice. The degrees of freedom for such a ground state are the choice of chirality(selecting from two possible orientations) and the common plane angle for the spins. Other than them, $\sqrt{3}\times\sqrt{3}$ state is unique and does not posses extensive ground state degeneracy. In summary, lacking extensive ground states degeneracy, an antiferromagnetic Heisenberg triangular lattice is not frustrated. Interestingly, Ising spins however, on a triangular lattice gives rise to an extensively degenerate ground state [25].

2. Kagome lattice

Similar to the triangular lattice, the constraint Eq. 2.14 applies to the ground states of Heisenberg antiferromagnet Hamiltonian on a Kagome lattice. As a result, for each triangular simplex, the spins are at 120° with each other. However unlike in a triangular lattice, adjacent triangles only share one spin. Therefore, in a ground state configuration, two neighboring triangular plaquettes need not share a universal common plane. We also see the existence of nonplanar ground state

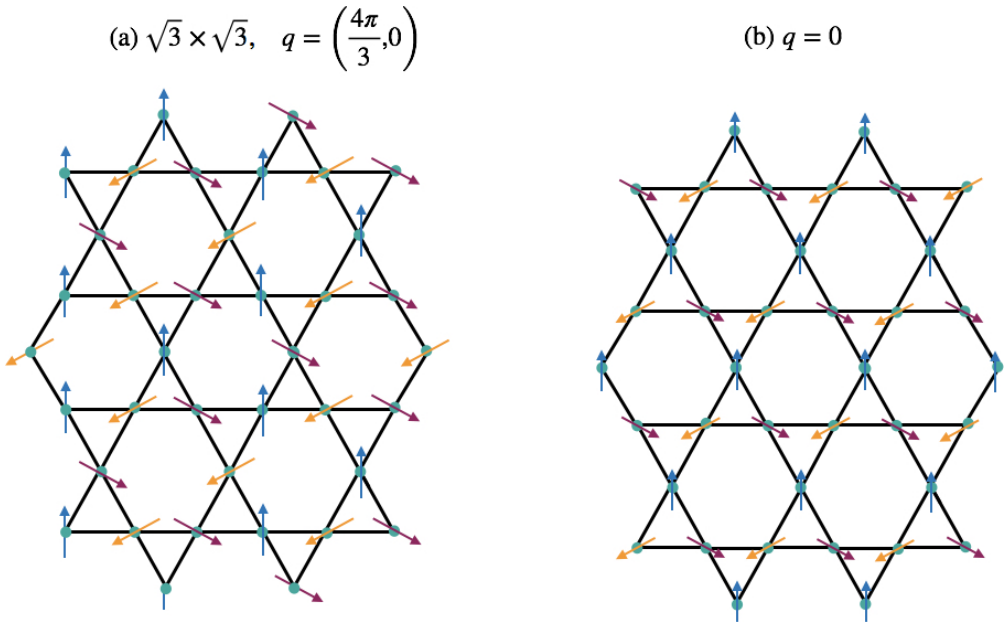

Figure 2.17: Coplanar Ground state configurations in a antiferromagnetic Kagome Heisenberg model

configurations in the Kagome lattice, unlike the definite coplanar order in triangular lattice, where all triangles have the same plane even at long distances.

There are two coplanar chiral states depicted in Figure 2.17 which can be described by a single wave vector $\mathbf{q} = \mathbf{0}$ state and $\sqrt{3} \times \sqrt{3}$ state with $\mathbf{q} = (\frac{4\pi}{3}, 0)$. These two states out of the many coplanar ground states were hypothesized to be selected by order-by-disorder [26] at even lower temperatures. However simulations revealed that the ground state spins configurations move to a non chiral spin configuration from any of $\mathbf{q} = \mathbf{0}$ or $\sqrt{3} \times \sqrt{3}$ states [27].

2.9 Spin Dynamics

Frustrated magnet in a cooperative paramagnetic phase moves around in its ground state manifold. An imminent question arises about its dynamics, that how do the spins move in time to shift from one ground state configuration to the next. We can use harmonic spinwave theory on a ground state configuration to analyse the low temperature dynamics.

Spin excitations in the ground state configurations in an ordered magnetic system can be interpreted

as oscillations of the spin vectors within the harmonic approximation i.e. around their equilibrium positions. These oscillations are brought about by small spin deviation, orthogonal to the equilibrium spin direction. These quantized fluctuations of the spins called magnons have translational symmetry that gives them wave like spatial composition, propagating through the system. Figure 2.18 shows such an oscillation in a Ferromagnetic system, where all spins are parallel in its ground state. The dispersion frequency of the oscillation can be calculated from the spin Hamiltonian using torque equations for spin angular momentum from classical mechanics.

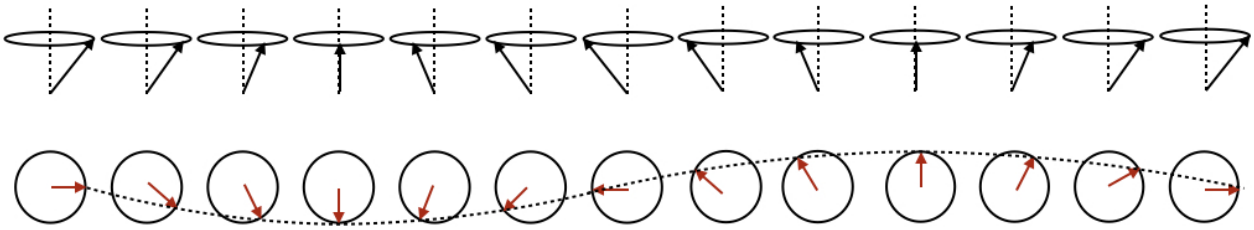

Figure 2.18: A schematic view of a spin wave.

Ground state spin configurations in frustrated systems usually do not have long range order. Therefore spinwave dynamics like need to numerically simulated. In frustrated systems, the excitations in the harmonic approximation limit predicts two range of frequencies. While one frequency type is for the frequency spectrum similar to conventional magnets with an upper limit of $f \sim \mathcal{O}(JS/\hbar)$, the other frequency spectrum are associated to the zero modes associated to the ground state fluctuation in the $\mathbf{x}$-direction Figure 2.14.

To numerically predict the time dependent motion of the interacting spins, we first calculate the effective field on each spin in the presence of exchange field set up by its nearest neighbors.

$$\mathcal{H}_{eff,i} = -(\nabla E_{total})_i = -\frac{\partial \mathcal{H}}{\partial \mathbf{S}_i} \tag{2.20}$$

If we have a energy conserving system, the spin trajectory of i_{th} spin in time t is given by the

Landau Lifshitz equation,

$$\frac{d\mathbf{S}_i(t)}{dt} = -\mathbf{S}_i(t) \times \mathcal{H}_{eff,i}(t) \tag{2.21}$$

Details regarding the derivation and conditions are explained in section 3.2

Time dependent behavior of correlation functions in frustrated systems have many exciting characteristics, as opposed to ordered magnetic systems. For example correlations relax far more rapidly on a Heisenberg antiferromagnetic system on a Kagome lattice as opposed to that on a square lattice. In cooperative magnets, fluctuation from one ground state to another(movement along x direction in the ground state phase space Figure 2.14) occurs at relatively short time scales. On the other hand in ordered magnets, dynamics (excitations around an ordered state) i.e. reorienting an existing magnetic ordering happens at much longer time scales.

As explained above, the ground state oscillations have zero frequency in the harmonic approximation. On considering anharmonic effects (soft modes: excitations along the y-direction in Figure 2.14), at low temperatures we see three important separation of time scales, the excitation spectrum width ($1/J$), excitation lifetime ($1/\sqrt{TJ}$) and the relaxation time of the Autocorrelation function ($\tau = 1/T$) [17]. The dynamics in such systems is identical to diffusion dynamics, where the Autocorrelation functional Eq. 2.22 is exponential.

$$\langle \mathbf{S}(t)\mathbf{S}(0) \rangle = exp(-cTt) \tag{2.22}$$

where $\langle ... \rangle$ denotes the statistical average over starting points i.e. large number of ground state configurations.

2.10 Neutrons as Probe

Neutrons are electrically neutral, which lets them penetrate into materials. Their magnetic moments can however interact with magnetic materials. As a result neutron scattering is a great experimental technique to study correlated magnetic materials. The partial differential scattering cross section also called the neutron scattering cross section is proportional to the dynamic structure factor ($S(\mathbf{q},\omega)$) which is the Fourier transform in space and time of spin-spin correlation function.

The partial neutron scattering cross section is defined as the total number of neutron scattered per unit time by the sample, into a unit solid angle $d\Omega$ in a particular direction. It is given by $\frac{d^2\sigma}{d\Omega dE_f}$, where σ represents total number of neutrons scattered per unit time by the sample, the $d\sigma/d\Omega$ gives the differential cross section, which is a time averaged position of all nuclei in the sample and dE_f represents the change in neutron energy. Static structure factor($S((q),t)$) is given by Fourier transform of summation of the spins into momentum space.

$$S((q),t) = \int d\mathbf{r} e^{\mathbf{q}\cdot\mathbf{r}} M(\mathbf{r},t) \tag{2.23}$$

where Magnetization density is $M(\mathbf{r},t) = \sum_i S_i(t)$ is the summation of all spins.

The dynamic structure factor is given by,

$$S((q),\omega) = \int dt e^{-i\omega t} \langle M(-\mathbf{q},0) \cdot M(\mathbf{q},t) \tag{2.24}$$

We see characteristics of ordered moments from neutron elastic scattering, while inelastic scattering shows us fluctuating(frustrated) moments. Features seen in the dynamic structure factor $S(\mathbf{q},\omega)$ have important experimental relevance. For example, as seen in Figure 2.19, we see a plot for frequency ω dependence of $S(\mathbf{q},\omega)$ and its respective Fourier transformation that indicate their spin-spin correlation behavior. Figure 2.20 shows the plot for $\mathbf{Q}$ dependence of $S(\mathbf{q},\omega)$. It shows

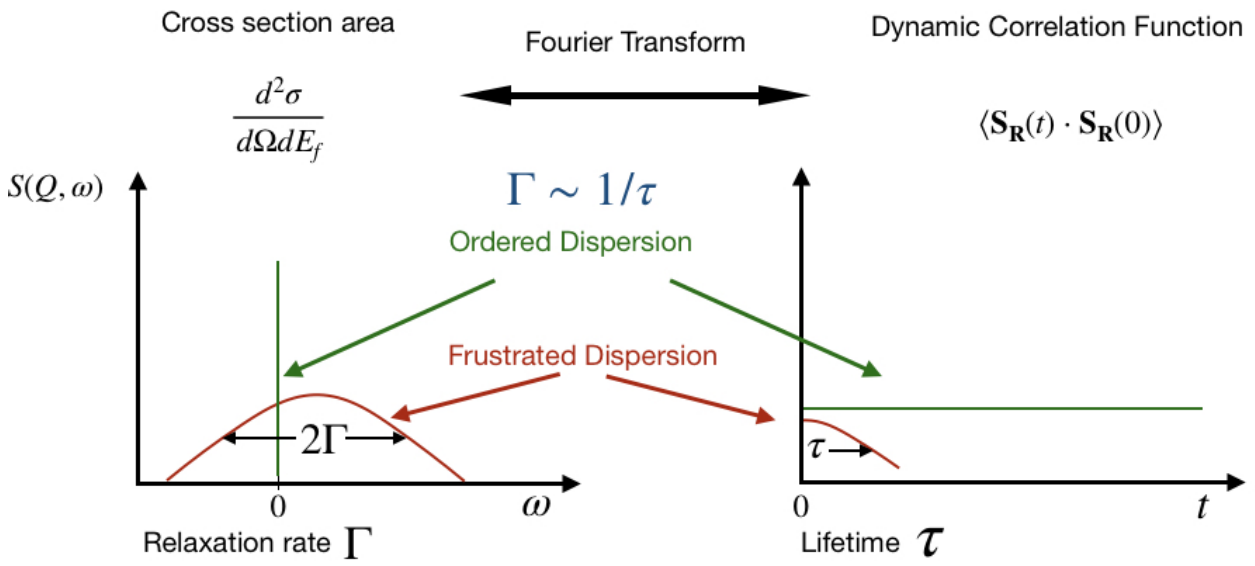

Figure 2.19: Time dependent Spin spin correlation characteristics as inferred from neutron scattering cross section. The relaxation time Γ in the energy spectrum of $\mathbf{S}(Q,\omega)$ is inversely related to the lifetime of the excitation τ.

that we can predict the spatial dependence of the correlations by observing the $\mathbf{Q}$ dependence of $S(\mathbf{q},\omega)$. Correlation length is inversely proportional to the $\mathbf{Q}$- width of $S(\mathbf{q},\omega)$. As a result if $S(\mathbf{q},\omega)$ is broader than the $\mathbf{Q}$ - resolution, then correlations are short ranged. Whereas a narrow $\mathbf{Q}$ - width $S(\mathbf{q},\omega)$ would indicate long ranged spatial correlations.

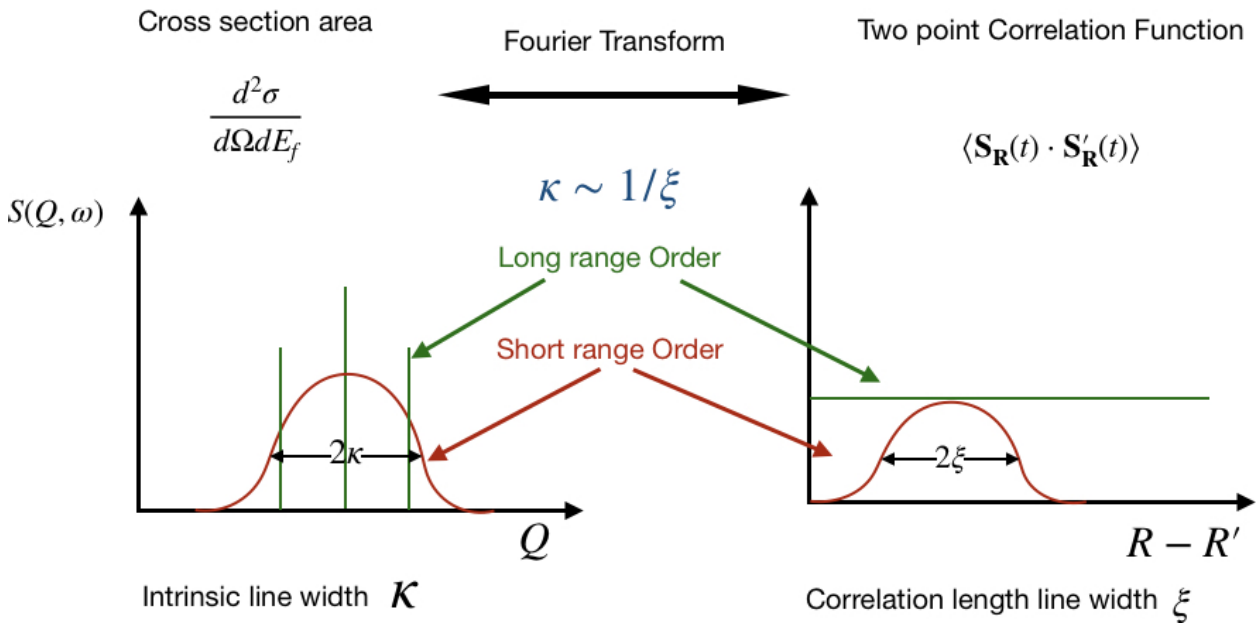

Figure 2.20: Two point Spin spin correlation characteristics as inferred from neutron scattering cross section. The linewidth κ in momentum exchange of $\mathbf{S}(Q,\omega)$ is inversely proportional to the correlation length ξ.

CHAPTER 3

NUMERICAL METHODS

In this chapter I have introduced the numerical methods used in the simulation of spin configurations. We use Monte Carlo algorithms to attain the spin configurations in frustrated magnets and Landau Lifshitz dynamics to calculate the spin trajectory in time. We have used a very fast and stable semi implicit integration algorithm to calculate the spin dynamics. The following sections explain the spin update schemes used in the Monte Carlo simulations and the steps of the integration algorithm.

3.1 Monte Carlo Simulations

Monte Carlo simulations [28] use statistical sampling to explore the states of exotic systems from the Boltzmann distribution of the problem.

3.1.1 Markov chain Monte Carlo

Lets denote a spin configuration of an entire system at a given instant by vector $\mathbf{X}$.

$$\mathbf{X}_{(0)} \rightarrow \mathbf{X}_{(1)} \rightarrow \quad . \ . \ . \ \mathbf{X}_{(a)} \rightarrow \mathbf{X}_{(b)} \rightarrow \quad . \ . \ . \quad \rightarrow \mathbf{X}_{(N_{MC})} \tag{3.1}$$

To get a required target spin configuration according to thermal distribution $p(\mathbf{x})$ we implement a stochastic process that takes a randomly generated initial spin configuration through series of Monte Carlo N_{MC} steps to reach the desired state. At each update from a state a we probabilistically generate a new state b. This process is called a Markov chain process [29], if the transition probability $P(a \rightarrow b)$ does not depend on the previous history of system prior to its state a and depends solely on the states a and b. A Markovian chain process satisfies two properties - ergodicity

and detailed balance.

Ergodicity ensures that all possible states of a system are reachable during the Monte Carlo process through any sequence of transitions. Say at an instant in time, the state represented by $\mathbf{X}_{(a)}$ has a distribution p_a. After one Markovian update the new distribution will be $p_a^{'}$. Therefore,

$$p_a^{'} = p_a + \sum_j [p_j P(X_j \rightarrow X_a) - p_a P(p_a \rightarrow X_j)] \tag{3.2}$$

Here the terms in the right side of the Eq. 3.2 represents the influx and exflux to and from the current configuration $\mathbf{X}_{(a)}$. If the system is in equilibrium in Monte Carlo simulations, the configurations are sampled in a stationary thermal distribution form. This ensures that the net flux is zero and we end up with a detailed balance condition that balances each update with its reverse as shown below.

$$p_j P(X_j \rightarrow X_i) = p_i P(p_i \rightarrow X_j) \quad \forall i \neg j \tag{3.3}$$

In classical systems, Boltzmann distribution is used to describe the equilibrium distributions where energy of the system is temperature dependent. Using the Maxwell-Boltzmann statistics, the probability of a system existing in a state a with internal energy E_a at equilibrium is given by,

$$p_a = \frac{1}{Z} e^{-\beta E_a} \tag{3.4}$$

Where $\beta = \frac{1}{kT}$, $k = 1.38e^{-23} JK^{-1}$ is the Boltzmann constant and $Z = \sum_a e^{-\beta E_a}$ is the partition function. The expectation value of an observable quantity $\mathcal{O}$ studied in classical systems is an average of the values of the observables across different states of the system,

$$\langle Q \rangle = \frac{1}{Z} Q_a e^{-\beta E_a} \tag{3.5}$$

Now coming back to our condition of detailed balance given by Eq. 3.3, satisfying the equation following a Boltzmann distribution we have,

$$\frac{P(X_i \to X_j)}{P(X_j \to X_i)} = e^{-\beta(E_i - E_j)} \tag{3.6}$$

Updating a spin configuration from one state to another is guided through selection probabilities and acceptance probabilities for the new configuration. These combined together determine the transition probability, represented as follows,

$$P(X_i \to X_j) = P_{selection}(X_i \to X_j) A_{acceptance}(X_i \to X_j) \tag{3.7}$$

where $P(X_i \to X_j)$ represents the transition probability from state i to state j; $P_{selection}(X_i \to X_j)$ represents the probability of selection of configuration j given the configuration i, based on convenient algorithms to generate possible updates and; $A_{acceptance}(X_i \to X_j)$ represents the fraction of transitions from $i \to j$ that should be accepted. $A_{acceptance}(X_i \to X_j)$ should be as close to 1 as possible while maintaining the detailed balance and Boltzmann distribution as in Eq 3.6.

It is possible to write Eq. 3.2 in matrix format $p^{'} = Tp$, where $T = P(\mathbf{X}_j \to \mathbf{X}_i) > 0$ is the transition matrix. $p = Tp$ represents the equilibrium state and has a non degenerate eigenvalue of 1 with $P(\mathbf{X}_i) > 0 \quad \forall i$. This implies that given any random initial spin configuration the system will converge to the desired configuration at thermal equilibrium. The Monte Carlo time steps for reaching equilibrium is given by the second largest length of the eigenvalue. In simulations, this equilibrium time is determined heuristically.

3.1.2 Metropolis-Hastings algorithm

It is one of the most popular and efficient Markov chain Monte Carlo methods which involve single spin update at every time step. This algorithm ensures ergodicity with the indefinite possibility of updating one spin at a time and reaching any state from any random state. The original algorithm was developed by Nicholas Metropolis in 1953 [29, 30] using Boltzmann distribution and then extended to general cases of other distributions in 1970 by W.K. Hastings. The $P_{selection}$ mentioned

in Eq. 3.7 is a random selection of spin site chosen for possible update. Given the sites are all equivalent, $P_{selection} = \frac{1}{N}$ with N being the total spins in the system. We rename the probability of selection of a state as function g i.e. $g \equiv P_{selection}$. One Monte Carlo step constitutes running the single spin update step N times. Then from the condition of detailed balance in Eq. 3.3 and transition probability in Eq. 3.7 we get,

$$\frac{P(X_i \to X_j)}{P(X_j \to X_i)} = \frac{g(X_i \to X_j)A_{acceptance}(X_i \to X_j)}{g(X_j \to X_i)A_{acceptance}(X_j \to X_i)} = \frac{A_{acceptance}(X_i \to X_j)}{A_{acceptance}(X_j \to X_i)} = e^{-\beta(E_i - E_j)} \tag{3.8}$$

The ratio of the acceptance probabilities can be set to anything as long as they together satisfy the detailed balance Eq. 3.8. Very small acceptance ratios would lead to wasted computation. To avoid that, the larger acceptance probability is set to 1 and the other is balanced accordingly.

With every spin update attempt, we have three possible scenarios. One where $\Delta E = E_i - E_j > 0$, $\beta = 1/kT > 0$ leads to $e^{\beta \Delta E} < 1$. As a result, since $P(X_j \to X_i) > P(X_i \to X_j)$ we set $P(X_j \to X_i) = 1$. On the other hand if $\Delta E < 0$ we can set $P(X_i \to X_j)$ to 1. In the last possible scenario there is no change in energy i.e. $\Delta E = 0$. If $\Delta E < 0$, the possible spin update causes a decrease in energy, the acceptance probability for the new spin is 1. However if the spin update cause increase in energy of the system, the new spin has a weighted w acceptance probability with $w = e^{-\beta \Delta E}$. To implement this acceptance probability, we generate a random number r between $0 \leq r < 1$, such that we accept the new spin if $r < w$.

To summarise, the entire Metropolis algorithm step by step consists of the following,

1. Compute the energy of the system given a spin configuration.

2. Random selection of a site of the lattice.

3. A new spin vector $\mathbf{S}_i'$ is proposed, with conserved length and changed orientation.

4. We calculate the ΔE. If $\Delta \leq 0$, we accept the new spin configuration.

5. If $\Delta > 0$, we define weight $w = e^{-\beta \Delta E}$ and generate a random number r such that $0 \leq r <$

1.

6. We accept the new spin if $r < w$. Otherwise we make no change in the configuration. All these conclude one metropolis step.

We repeat the above steps N = Total spins times to complete One Monte Carlo step. Number of Monte Carlo steps to thermalise a system at a given temperature T is determined heuristically such that when the energy of the system stops changing and decreasing with consequent Monte Carlo steps, we have reached equilibrium.

Calculating ΔE for the entire lattice at every Metropolis step is computationally expensive. The Only change if energy comes for the nearest neighbors. To save computation time over unused calculations, we calculate the change in energy coming for the k number of nearest neighbors of the i_{th} random chosen spin for possible update. An example of energy change in case of Heisenberg interaction is given in Eq. 3.9.

$$\Delta E = -J \sum_{k} \mathbf{S}_i' \mathbf{S}_k - (-J \sum_{k} \mathbf{S}_i \mathbf{S}_k) \tag{3.9}$$

In case of a system with Ising spin, the proposed new spin vector is randomly selected between +1 and -1. While in an Heisenberg spin the new spin $\mathbf{S}_i'$ update is generated as follows,

$$\mathbf{S}_i' = \begin{bmatrix} \sqrt{1-\cos^2\theta}\cos\phi \\ \sqrt{1-\cos^2\theta}\sin\phi \\ \cos\theta \end{bmatrix} \tag{3.10}$$

Where the angles are randomly generated according to $\phi \in \text{Uniform}(0, 2\pi)$ and $\theta \in \text{Uniform}$ $(\cos\theta_0, 1)$. When we generate a new spin at low temperatures, we don't want a high energy difference as that would lower acceptance rates and cause a significant slow down in reaching a temperature appropriate thermal equilibrium ground state configuration. To avoid this slowing down,

we can propose an updated new spin $\mathbf{S}_i'$ inside a cone around the original spin $\mathbf{S}_k$ with an angular deviation of $2\theta_0$, such that $|\mathbf{S}_i' - \mathbf{S}_i| = 2\sin\frac{\theta_0}{2}$. A smaller deviation would give larger acceptance rates.

3.1.3 Measurement statistics

The common quantities that are measured at one particular temperature T at a time during the Monte Carlo simulations include energy, magnetization, specific heat and susceptibility. As discussed previously, we define one Monte Carlo step as a metropolis sweep over N lattice sites for spin updates. Say the total number of Monte Carlo steps used is $\mathrm{MCS_T}$. Out of these steps, some initial Monte Carlo steps $\mathrm{MCS_0}$ which are about 10% of the total are discarded. Using the remaining Monte Carlo steps $\mathrm{MCS_n}$, values of energy and magnetization are calculated by accumulating their values after every Monte Carlo step. This gives the expectation value of any measurable quantity $\langle\mathcal{O}\rangle$ averaged over $\mathrm{MCS_n}$ steps.

The **Magnetization** $M(T)$ at a temperature T for a lattice of N total spins calculated per spin is defined as follows,

$$M(T) = \frac{1}{N}\left\langle\left|\sum_{i=1}^{N}\mathbf{S}_i\right|\right\rangle \tag{3.11}$$

Magnetic **Susceptibility** per spin is defined as,

$$\chi(T) = \beta N(\langle M(T)^2\rangle - \langle M(T)\rangle^2) \tag{3.12}$$

Specific heat capacity per spin is defined as,

$$C(T) = \frac{\beta^2}{N}(\langle E(T)^2\rangle - \langle E(T)\rangle^2) \tag{3.13}$$

3.1.4 Phase transitions and critical phenomenon

Phase transitions are one of phenomenon studied using Monte Carlo Algorithms. A phase transition is defined as the change in phase of a thermodynamic system in presence of external stimuli in form of pressure or temperature. Transitions between states of matter like solid, liquid and gas, between magnetic states like paramagnetic and ferromagnetic are some common examples of phase transitions.

The free energy before and after the transition are described by two different functions. As a result the energy dependent thermodynamic observables have different properties before and after the transition. Consequently near the transition point, we observe unusual behavior, like in divergence of observed quantities and critical slowing down. Such behavior is frequently observed in the measurement of heat capacity in form of sudden infinite values, erratic jumps or discontinuity in the derivative of specific heat capacity.

Phase transitions are broadly divided into two categories - first order transition and second order transition. In first order transitions, properties like density, magnetization or energy as a function of either pressure or temperature while crossing the transition point have sudden discontinuity. During such transitions, the system undergoes a change in internal energy either by loosing or absorbing a definite amount of energy in the form of latent heat. While the system undergoes transfer of heat, it exists in a mixed phase regime. On the other hand, in second order transitions a system changes from one state to another without any discontinuity or sudden erratic behavior in the above properties. These continuous phase transitions are characterised by critical exponents usually associated with broken symmetry before and after the phase transition. The number attached to the order type of phase transition comes from the count of derivative of free energy which shows the first discontinuous behavior.

Phase transitions are characterized by order parameters such that as a system goes from un-ordered phase to an ordered phase, a particular defined property called order parameter goes from zero value to a non zero value.

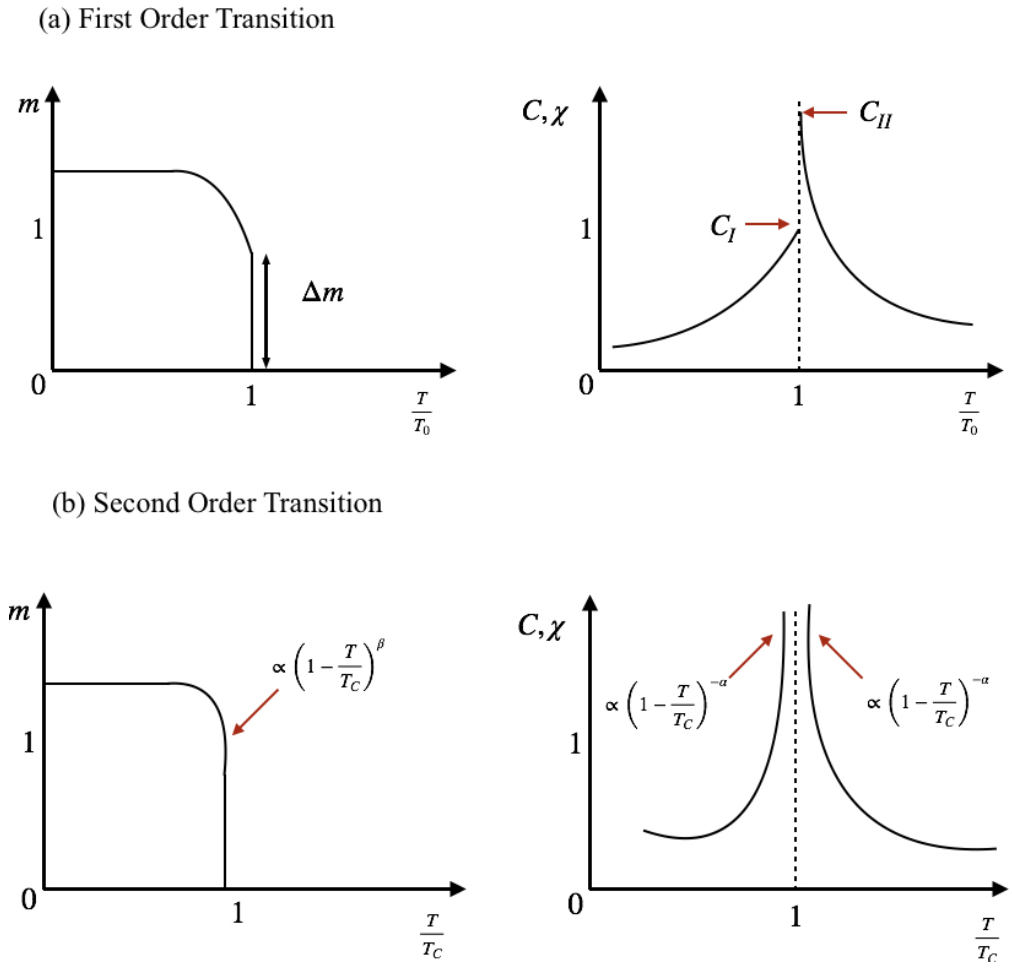

Figure 3.1: Characteristics of magnetization m, specific heat capacity C and susceptibility χ in (a) First Order phase transition: Discontinuity in magnetization curve with a sudden jump of Δm, discontinuity and in specific heat/ susceptibility curves with different amplitudes before and after the transition. (b) Second Order phase transition: Smooth magnetization curve, No change in amplitude for C or χ at the transition

Correlation functions have interesting properties near phase transitions. We measure the spatial correlation between regions separated by a distance r using a function given by,

$$\mathcal{C}_{\mathbf{S}} = \langle \mathbf{S}(0)\mathbf{S}(r) \rangle \tag{3.14}$$

which is the probability of finding a quantity $\mathbf{S}$ with same value at two different lattice sites separated by distance r. Correlation length ξ diverges near the critical point that points to the presence of long wavelength fluctuations. Consequently, the divergence of ξ also leads to a phenomenon called critical slowing down near the phase transition, where the system takes a long time to change from one configuration to another. This time is defined as the relaxation time τ. Near the phase transition we have long relaxation time proportional to some power of ξ. We can describe the critical slowing down with the following equations.

$$\tau \propto \xi^z \tag{3.15}$$

where z is the dynamical critical exponent [28]. Correlation length ξ is dependent on the lattice size L such that, in a lattice of finite length L, the correlation length and decorrelation time both display peaks with steep slopes near the critical point.

$$\tau \propto L^z \tag{3.16}$$

Near the phase transition critical temperature T_C the temperature varying properties like magnetization M, specific heat C_V and susceptibility χ can be described by the following power law equations.

$$M = M_0 \varepsilon^\beta \tag{3.17}$$

where M_0 is a constant, β is the critical exponent and $\varepsilon = |1 - T/T_C|$. Similarly, in some systems the discontinuity in internal energy w.r.t temperature near the phase transition manifests itself as

sharp peaks in the specific heat curve that can be characterised by critical exponent α (see Figure 3.1).

$$C_V = C_0 \varepsilon^{-\alpha} \tag{3.18}$$

The magnetic susceptibility in absence of external magnetic field is given by,

$$\chi = \chi_0 \varepsilon^{-\gamma} \tag{3.19}$$

and the correlation length follows,

$$\xi = \xi_0 \varepsilon^{-\nu} \tag{3.20}$$

3.1.5 Finite size scaling

So far we have considered the expected behavior of the systems in the thermodynamic limit $L^{-1} \to 0$, where L is the linear size of a system. In such systems, we expect the occurrence of singularity at the critical temperature T_C where the correlation length $\xi \to \infty$. In practise simulating very large systems that can mimic the behavior of infinite systems is computationally prohibitive. In most cases, we encounter finite size effects while simulating finite L systems like difficulty in identifying the power law behavior of the observables, very subtle or non existence of sharp peaks at the discontinuities existing near critical temperatures. The observables like magnetisation, susceptibilty and specific heat capacity as seen in Figure 3.2 (a), (c) and (e) can be scaled appropriately and are used to estimate the critical exponents and critical temperatures.

Finite size scaling is a way of extracting values for the critical exponents and estimate the critical temperature T_C. In finite size systems, as the correlation length approaches L, the susceptibility also gets cut-off. Therefore as long as $\xi \ll L$, the finite system size will not effect the behavior of observations as compared to the systems close to thermodynamic limit. Since correlation length in limited by system size, if we have $\xi \equiv L$ finite size effects become more apparent.

Near the transition temperature T_C, the role of correlation length in scaling formulas like Eq. 3.17,

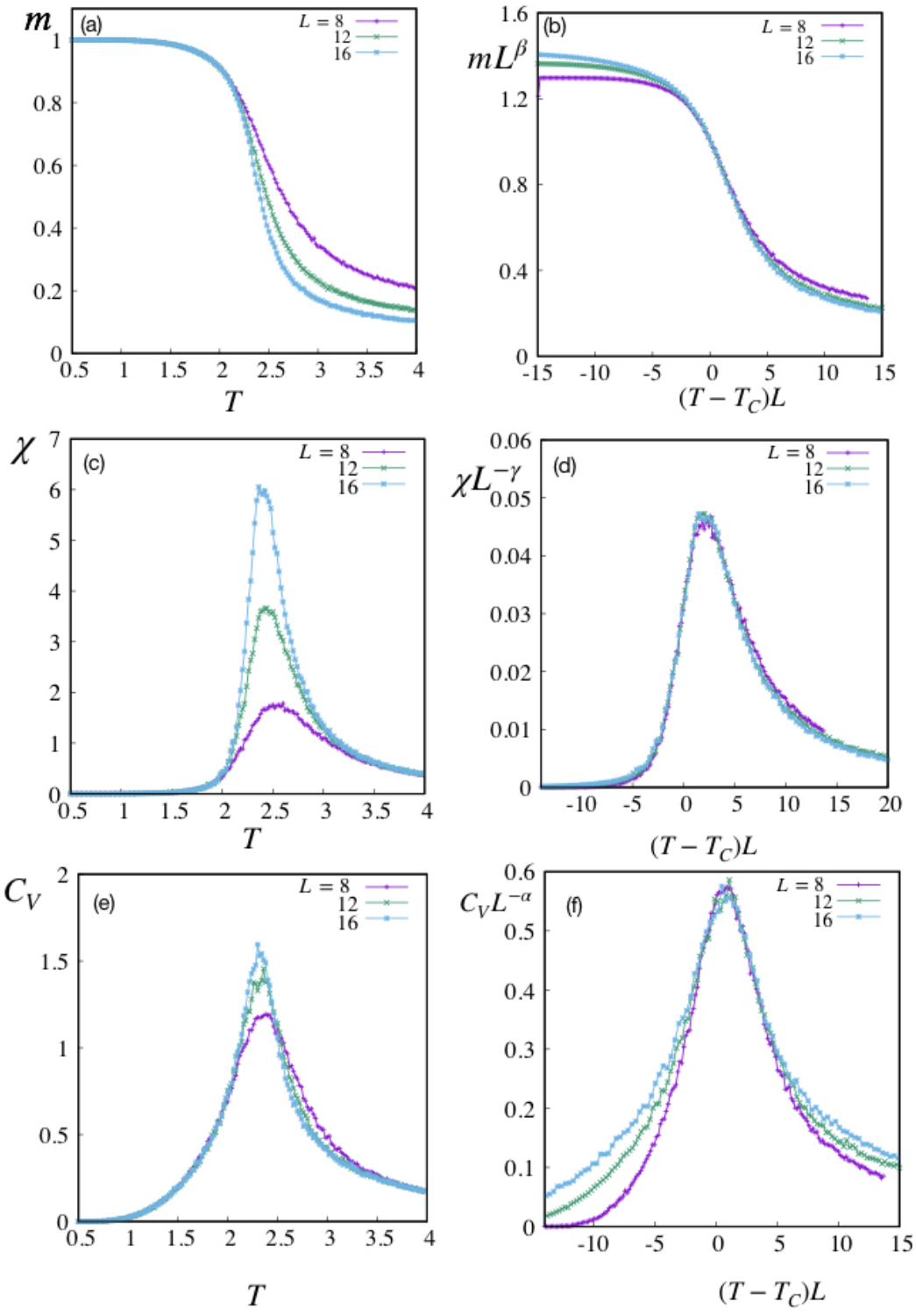

Figure 3.2: Critical exponents for phase transition in an Ising model on a 2D square lattice. Simulations for lattice sizes $L = 8, 12, 16$. Transition temperature $T_C = 2.269$ (a) and (b) Magnetization m:$\beta = \frac{1}{8}$,(c) and (d) Susceptibility χ:$\gamma = \frac{7}{8}$, (e) and (f) Specific heat capacity: $\alpha = 0$

3.18 and 3.19 becomes dependent on the finite system size L. We can write Eq. 3.20 in terms of L where $\varepsilon = |1 - T/T_C| \propto \xi^{-1/\nu} \rightarrow L^{-1/\nu}$. As a result we can rewrite the scaling laws in terms of L. This concept is familiarly called finite size scaling. For example $\chi(T, L)$, a function of temperature and system size can be written in terms of the scaling variable $x = (1 - T/T_C)L^{1/\nu}$ where $T - T_C$ is called the reduced temperature such that $\chi(T, L) = L^{\gamma/\nu} f(x)$. As a direct consequence of this scaling, plots of $\chi(T, L)L^{\nu/\gamma}$ w.r.t to the scaling variable x for different temperatures T and system size L collapse on a single curve. Similar scaling observation is seen for specific heat $C_V L^{\nu/\beta}$ vs x and magnetization $mL^{\nu\beta}$ vs x. This scaling behavior is verified in Figure 3.2 for Ising model on a 2D square lattice.

3.2 Spin Dynamics

3.2.1 Spin trajectory: Landau-Lifshitz equation

To simulate the trajectories of spin vectors in time, we need to solve for the equations of motion for the spins. The starting point of the semiclassical equations of motion for a spin in the presence of exchange field is set up by its nearest neighbors. This nearest neighbor field on i_{th} spin $\mathbf{S}_i$ is called the effective Hamiltonian.

$$\mathcal{H}_{eff,i} = -(\nabla E)_i = -\frac{\delta \mathcal{H}}{\delta \mathbf{S}_i} \tag{3.21}$$

where $\mathcal{H}$ is the system spin interaction Hamiltonian and E gives the energy of the spin configuration. Quantum mechanical operator that governs the dynamics of a spin vector $\mathbf{S}$ is given by the commutator,

$$i\hbar \frac{\partial \mathbf{S}}{\partial t} = [\mathbf{S}, \mathcal{H}] \tag{3.22}$$

The classical regime equivalent that defines the commutator for the spin system is given by Poisson

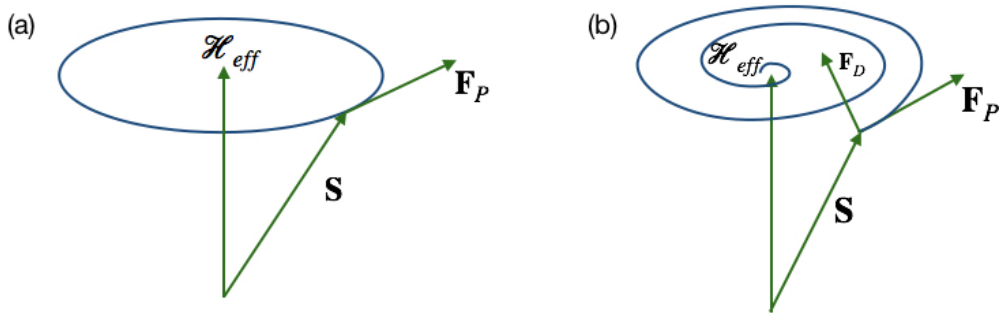

Figure 3.3: Lamor Spin precessional motion.Spin precesses around the effective field H_{eff} (a) Undamped - Energy conserving (b)Damped

bracket relations.

$$\left\{S_i^\alpha, S_j^\beta\right\} = \epsilon_{\alpha\beta\gamma}\delta_{ij}S_i^\gamma \tag{3.23}$$

Using the above commutator equation in conjunction with the Hamiltonian $\mathcal{H}$ we get a vector component α wise equation,

$$\left\{S_i^\alpha, \mathcal{H}\right\} = \hbar\frac{\partial S_i^\alpha}{\partial t} = \sum_{j=1}^{N}\epsilon_{\alpha\beta\gamma}\delta_{ij}\frac{\partial \mathcal{H}}{\partial S_j^\beta}S_i^\gamma = \left(\frac{\partial \mathcal{H}}{\partial \mathbf{S}_i} \times \mathbf{S}_i\right)^\alpha \tag{3.24}$$

Using the equation for the net effective Hamiltonian on each spin as a result of its nearest neighbors from Eq. 3.21 we get

$$\hbar\frac{\partial \mathbf{S}_i}{\partial t} = -\frac{\partial \mathcal{H}}{\partial \mathbf{S}_i} \times \mathbf{S}_i = -\mathbf{S}_i \times \mathcal{H}_{eff,i} \tag{3.25}$$

Eq. 3.25 gives a trajectory of spin motion which is described in Figure 3.3 (a). The energy conserving motion where the spin vector changes direction on a circular path while the its magnitude is conserved in time is called Larmor precession.

However to simulate more realistic physical behavior, it requires a damping term that mimics the energy dissipation behavior. Landau and Lifshitz introduced the damping term of strength λ to the spin equation of motion as given below,

$$\frac{\partial \mathbf{S}_i}{\partial t} = \frac{1}{\hbar}(\mathcal{H}_{eff,i} \times \mathbf{S}_i) + \frac{\lambda}{\hbar}(\mathcal{H}_{eff,i} \times \mathbf{S}_i) \times \mathbf{S}_i \tag{3.26}$$

The damped spin motion is described in Figure 3.3 (b) The damping force F_D points towards the local minimum along the the direction of effective field $\mathcal{H}_{eff,i}$.

I study spin dynamics in presence of two different types of interaction Hamiltonians on two different lattices. One of them is the Gamma model on a Honeycomb lattice 4.1 and the other one is antiferromagnetic Heisenberg interaction on a Kagome bilayer 5.1. Each of them have a well defined effective Hamiltonian based on their nearest neighbor interactions, which helps us easily formulate the equations of motion for spin dynamics.

3.2.2 Numerical implementation: Semi implicit integration of Landau-Lifshitz equation

There are many different ways of solving a partial differential equation using either analytical or numerical solution. While analytical solution gives us the exact answer, it is complicated and sometimes impossible to find a closed explicit analytical solution for complex interactions and N-body problems. As a result N-body differential equations like Landau-Lifshitz are solved numerically.

There are many numerical integration methods to simulate the time dynamics. While we evaluate a method to use, the foremost characteristics that render weight to any integration method are stability and speed(less iterations). An ideal technique will give a stable and precise solution as well use less iteration steps(larger dt). Explicit integration methods are easy to implement and faster than their implicit counterparts but less stable. The deterministic Landau-Lifshitz equation in form of dimensionless i_{th} spin vector variable $(S)_i$ is given by,

$$\frac{\partial \mathbf{S}_i}{\partial t} = -\mathbf{S}_i \times \mathcal{H}_{eff,i} - \alpha \mathbf{S}_i \times [\mathbf{S}_i \times \mathcal{H}_{eff,i}] \quad i = 1, 2, ...n \text{ spins} \tag{3.27}$$

Where the B_i is the effective field and α is the damping factor. Writing this in differential form we get,

$$d\mathbf{S}_i = \mathbf{S}_i \times \mathbf{a_i}(\mathbf{S})dt \tag{3.28}$$

where $a_i(\mathbf{S})$, $\mathbf{S} \in \mathbb{R}^{3n}$, is 3 dimensional vector function of $\mathbf{S}$ defined in Eq. 3.31.

I have used a semi implicit (SIB) method introduced by Mentink et al [31]. in 2010. While standard mid point implicit integration methods have high stability, they are very slow as it requires solving 3N coupled questions in three dimensions. Here's where the semi implicit method is advantageous that is appropriately stable even over comparatively larger time steps. The method has some unique properties like it conserves the spin length and solves the 3 linear coupled equations at every time step.

The SIB method is two step integral solver. The first step is called a predictor followed by a corrector step. The predictor step follows after the Euler method and is modified to intrinsically preserve the spin length. In the next steps we will use the following convention to represent the spins. The i_{th} spin vector ($\mathbf{S}_i = (S_i^x, S_i^y, S_i^z)$) at time step k is $\mathbf{S}_k^i$. The intermediate predictor at time k step is the spin vector $\mathbf{P}_i^k$

$$\mathbf{P}_i^k = \mathbf{S}_i^k + h\frac{\mathbf{S}_i^k + \mathbf{P}_i^k}{2} \times \mathbf{a}_i^k(\mathbf{S}_i^k) \tag{3.29}$$

Then we have the corrector step and the updated spin vector at time step $k+1$ becomes,

$$\mathbf{S}_i^{k+1} = \mathbf{S}_i^k + h\frac{\mathbf{S}_i^k + \mathbf{P}_i^{k+1}}{2} \times \mathbf{a}_i^k\big(\frac{\mathbf{S}_i^k + \mathbf{P}_i^k}{2}\big) \quad i = 1, 2, ...\text{n spins}, \quad k = 1, 2, ...\text{N time steps} \tag{3.30}$$

where $a_i(\mathbf{S})$ is a function of vector $\mathbf{S}$ and $\mathcal{H}_i(\mathbf{S})$ is the effective field at spin i which is also a function of the variable $\mathbf{S}$.

$$\mathbf{a}_i^k(\mathbf{S}_i^k) = -\mathcal{H}_{i,eff}(\mathbf{S}_i^k) - \alpha\mathbf{S}_i \times \mathcal{H}_{i,eff}(\mathbf{S}_i^k) \tag{3.31}$$

$$\mathbf{a}_i^k\big(\frac{\mathbf{S}_i^k+\mathbf{P}_i^k}{2}\big) = -\mathcal{H}_{i,eff}\big(\frac{\mathbf{S}_i^k+\mathbf{P}_i^k}{2}\big) - \alpha\big(\frac{\mathbf{S}_i^k+\mathbf{P}_i^k}{2}\big) \times \mathcal{H}_{i,eff}\big(\frac{\mathbf{S}_i^k+\mathbf{P}_i^k}{2}\big) \tag{3.32}$$

We represent $\mathbf{a}_i^k(\mathbf{S}_i^k)$ at the predictor step as $\mathbf{a}_P$ and at the corrector step as $\mathbf{a}_C$. Then we can rewrite Eq. 3.29 in the matrix format (Eq. 3.33) to get the predictor step spin vector $\mathbf{P}_i^k$ at time step k and Eq. 3.30 in the matrix format (Eq. 3.34) to get an updated spin vector $\mathbf{S}_i^{k+1}$ at time step $k+1$.

$$\begin{bmatrix} P_{i,x}^k \\ P_{i,y}^k \\ P_{i,z}^k \end{bmatrix} = \begin{bmatrix} 1 & -\frac{h}{2}a_{Pi,z} & \frac{h}{2}a_{Pi,y} \\ \frac{h}{2}a_{Pi,z} & 1 & -\frac{h}{2}a_{Pi,x} \\ -\frac{h}{2}a_{Pi,y} & \frac{h}{2}a_{Pi,x} & 1 \end{bmatrix}^{-1} \begin{bmatrix} 1 & \frac{h}{2}a_{Pi,z} & -\frac{h}{2}a_{Pi,y} \\ -\frac{h}{2}a_{Pi,z} & 1 & -\frac{h}{2}a_{Pi,x} \\ \frac{h}{2}a_{Pi,y} & -\frac{h}{2}a_{Pi,x} & 1 \end{bmatrix} \begin{bmatrix} S_{i,x}^k \\ S_{i,y}^k \\ S_{i,z}^k \end{bmatrix} \tag{3.33}$$

$$\begin{bmatrix} S_{i,x}^{k+1} \\ S_{i,y}^{k+1} \\ S_{i,z}^{k+1} \end{bmatrix} = \begin{bmatrix} 1 & -\frac{h}{2}a_{Ci,z} & \frac{h}{2}a_{Ci,y} \\ \frac{h}{2}a_{Ci,z} & 1 & -\frac{h}{2}a_{Ci,x} \\ -\frac{h}{2}a_{Ci,y} & \frac{h}{2}a_{Ci,x} & 1 \end{bmatrix}^{-1} \begin{bmatrix} 1 & \frac{h}{2}a_{Ci,z} & -\frac{h}{2}a_{Ci,y} \\ -\frac{h}{2}a_{Ci,z} & 1 & -\frac{h}{2}a_{Ci,x} \\ \frac{h}{2}a_{Ci,y} & -\frac{h}{2}a_{Ci,x} & 1 \end{bmatrix} \begin{bmatrix} S_{i,x}^k \\ S_{i,y}^k \\ S_{i,z}^k \end{bmatrix} \tag{3.34}$$

Dynamics in this thesis is energy conserving and doesn't involve any damping factor. As a result we use $\alpha = 0$ in Eq. 3.27 to simulate our spin dynamics.

CHAPTER 4

HIDDEN PLAQUETTE ORDER IN CLASSICAL SPIN LIQUID STABILIZED BY STRONG OFF-DIAGONAL EXCHANGE

4.1 Results summary

- We report a new classical spin liquid in which the collective flux degrees of freedom break the translation symmetry of the honeycomb lattice.
- This exotic phase exists in the frustrated spin-orbit magnets where a dominant off-diagonal exchange, called the Γ term, results in a macroscopic ground-state degeneracy at the classical level.
- This phase transition is driven by thermal order-by-disorder at a critical temperature $T_c \approx 0.04|\Gamma|$. The transition reduces the emergent spherical spin-symmetry to a cubic one: spins point predominantly toward the cubic axes, yet seem to remain disordered at $T < T_c$.
- We show that the phase transition corresponds to a hidden plaquette ordering of hexagonal fluxes which explicitly breaks the cubic symmetry. Our results are confirmed by extensive Monte Carlo simulations.
- We further compute the dynamical structure factors of the spin-liquid phase and reveal unusual dynamical properties of the hexagonal flux parameters.

4.2 Introduction

Mott insulators with strong spin-orbit coupling have generated considerable interest recently [32]. The local magnetic degrees of freedom in such materials are entities with significant orbital character. This special property leads to effective interactions that exhibit strong anisotropy in both

real and pseudo-spin spaces, as described by novel Hamiltonians such as quantum compass or 120° models [33, 34]. A new type of magnetic frustration [35–37], which is different from the well studied geometrical frustration [18, 26, 38, 39], originates from the nontrivial interplay between lattice geometry and anisotropic spin-orbital exchange. One recent representative example is the spin-1/2 honeycomb Kitaev model [4] with Ising-like interactions involving different spin components on the three distinct nearest-neighbor bonds. Remarkably, the Kitaev model is exactly solvable and exhibits a quantum spin-liquid ground state with fractionalized excitations [4, 40, 41]. The classical limit of the Kitaev Hamiltonian also exhibits a macroscopic ground-state degeneracy and interesting order-by-disorder phenomena [9, 14, 42, 43].

The recent enormous interest in frustrated spin-orbit magnets is triggered by the realization that spin interactions in certain $4d$ and $5d$ Mott insulators are dominated by the anisotropic Kitaev-type exchange [13, 44–46]. The presence of other spin interactions, notably the isotropic Heisenberg exchange, in these compounds eventually drives the system into a magnetically ordered state despite a dominate Kitaev term [47–58].

Nevertheless, the search for spin liquids in frustrated spin-orbit magnets continues. Experimentally, tuning spin interactions by applying magnetic field [59–61] or pressure [62, 63] has been attempted to suppress the magnetic order. On the theoretical side, it has been pointed out that the off-diagonal exchange anisotropy, the so-called Γ term, plays a crucial role in the magnetic behaviors of these spin-orbit Mott insulators [64–70]. In fact, the suppression of long-range order in some compounds is suspected to be due to the increased strength of Γ interaction, instead of the enhanced Kitaev-type exchange [71, 72]. This experimental tendency can be understood from a recent theoretical work that shows a new classical spin liquid in the idealized Γ model on the honeycomb lattice and its three-dimensional variants [73]. The rest of the work is organized as follows. In section 4.3, we investigate the ground-state manifold of Γ-model on the honeycomb lattice and discuss the results of the Monte Carlo simulation to investigate the thermodynamic behaviors of the model at low temperatures. In section 4.4 we characterize the continuous degenerate

ground-state manifold. In the proceeding section 4.5, we investigate the emergent phase at low temperatures that is facilitated by thermal order by disorder. Section 4.6 shows our calculations of the zero modes and their relation to the specific heat of the degenerate manifold. In section 4.7, we characterize the phase transition and the corresponding order parameter using Monte Carlo simulations and finite size scaling. In sections 4.8 and 4.9, we compute the static and dynamic structure factors and study the dynamical behavior of fluxes. We have also investigated the influence of magnetic field on the Γ-model. The summary of the results are presented in section 4.10. We have discussed the set up of the Honeycomb lattice for the implementation of the numerical methods in Sec. 4.11. We conclude in Sec. 4.12 with a brief summary and outlook on future work. Our results are published in [74].

4.3 Model and method

We investigate the thermodynamic behavior of the Γ model at low temperatures and demonstrate a phase transition driven by order-by-disorder at $T_c \approx 0.04\,|\Gamma|$. Importantly, we show a hidden plaquette order that breaks the lattice transition symmetry below T_c. To begin with, we consider the Γ model on the honeycomb lattice, in which nearest-neighbor (NN) spin interaction is dominated by the off-diagonal exchange term. It involves different spin-components on the three inequivalent NN bonds, denoted as x, y, and z (see Fig. 4.1), on the honeycomb lattice:

$$\begin{aligned}\mathcal{H} &= \Gamma \sum_{\langle ij\rangle \| x} (S_i^y S_j^z + S_i^z S_j^y) + \Gamma \sum_{\langle ij\rangle \| y} (S_i^z S_j^x + S_i^x S_j^z) \\ &\quad + \Gamma \sum_{\langle ij\rangle \| z} (S_i^x S_j^y + S_i^y S_j^x). \end{aligned} \tag{4.1}$$

Here $\langle ij\rangle \parallel \xi$ denotes NN pairs along bond of type-ξ. Both signs of Γ are considered here, although energetically the two cases are equivalent due to the bipartite nature of honeycomb lattice.

The classical ground states of Γ model are extensively degenerate [73], giving rise to a new type of classical spin liquid which is different from the familiar cases in geometrically frustrated mag-

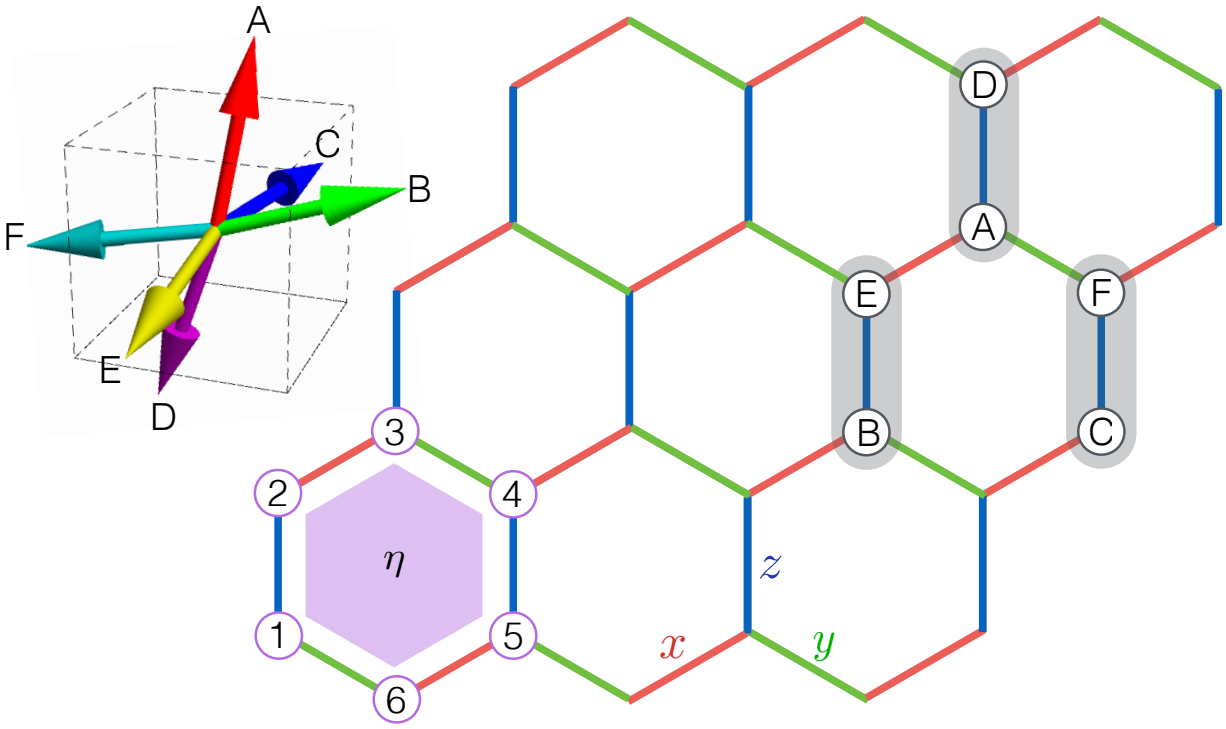

Figure 4.1: Ground states of the Γ model on a honeycomb lattice. A generic ground state is characterized by a directional vector $\hat{\mathbf{n}} = (a, b, c)$ and a set of Ising variables $\{\eta_\alpha\}$ defined on individual hexagons. To construct a ground state, first we build a perfect $\sqrt{3} \times \sqrt{3}$ order based on the six inequivalent spins of the tripled unit cell: $\mathbf{S}_{\rm A} = (a, b, c)$, $\mathbf{S}_{\rm B} = (c, a, b)$, $\mathbf{S}_{\rm C} = (b, c, a)$, $\mathbf{S}_{\rm D} = \zeta(b, a, c)$, $\mathbf{S}_{\rm E} = \zeta(a, c, b)$, and $\mathbf{S}_{\rm F} = \zeta(c, b, a)$. Here $\zeta = -\mathrm{sgn}(\Gamma)$. Next, go through every hexagon and modify the component of its six spins: $S_1^x \to \eta S_1^x$, $S_2^y \to \eta S_2^y$, $S_3^z \to \eta S_3^z$, $S_4^x \to \eta S_4^x$, $S_5^y \to \eta S_5^y$, and $S_6^z \to \eta S_6^z$. In the example shown above, $\zeta = -1$. The spins of shaded hexagon at the lower left corner are: $\mathbf{S}_1 = (a, b, c)$, $\mathbf{S}_2 = \zeta(b, a, c)$, $\mathbf{S}_3 = (b, c, a)$, $\mathbf{S}_4 = \zeta(a, c, b)$, $\mathbf{S}_5 = (c, a, b)$, and $\mathbf{S}_6 = \zeta(c, b, a)$.

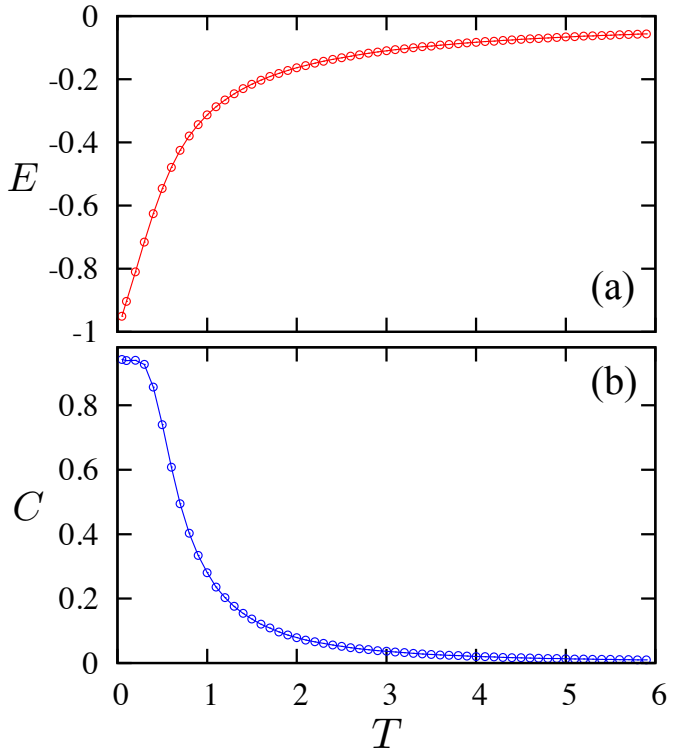

Figure 4.2: (a) Energy density and (b) specific heat vs temperature of the Γ model down to temperature $T \sim 0.05$. Here both energy and temperatures are expressed in units of $|\Gamma|$.

nets.

We use Monte Carlo simulation to investigate the thermodynamic behaviors of the Γ model at low temperatures. Standard Metropolis-Hastings algorithm based on local updates is used to sample spin configurations in thermal equilibrium. Our MC simulations over a wide temperature range show no sign of phase transition down to $T \sim 0.05|\Gamma|$ (Figure. 4.2).

Fig. 4.2 shows the energy density E and specific heat C versus T over a wide temperature range. There is no sign of a phase transition down to temperatures as low as $T \sim 0.05|\Gamma|$. The energy density gradually approaches its minimum $E_0 = -|\Gamma|$, while the specific heat shows a plateau-like feature at $T \lesssim 0.1\,|\Gamma|$.

The static structure factor for $\Gamma > 0$ exhibits a broad minima at $\mathbf{q} = 0$ at $T = 0.05|\Gamma|$ (Figure 4.11). The absence of Bragg peaks is consistent with the spin-liquid picture. The fact that there

is no pinch-point singularity, which is a unique feature of spin liquids in geometrically frustrated magnets [22–24], also points to a different nature of the macroscopic degeneracy in Γ model. MC simulations further find extremely short-ranged spin-spin correlation, which is similar to that seen in Kitaev spin liquid [4, 42], but different from that of geometrically frustrated systems.

4.4 Ground state degeneracy

The characterization of the degenerate ground-state manifold has been discussed in great detail in Ref. [73]. A generic ground state is specified by a directional vector $\hat{\mathbf{n}} = (a, b, c)$ and a set of Ising variables $\{\eta_\alpha\}$ defined on individual hexagons; see Fig. 4.1.

In the classical limit, or without consideration of dynamical effects, these Ising variables are pure gauge degrees of freedom and will remain disordered at all temperatures. An explicit procedure for constructing the ground state is as follows. First, we use the unit vector $\hat{\mathbf{n}}$ to derive six inequivalent spins $\mathbf{S}_\mathrm{A}$, $\mathbf{S}_\mathrm{B}$, $\cdots$, $\mathbf{S}_\mathrm{F}$ for the tripled unit cell of a perfect $\sqrt{3} \times \sqrt{3}$ long-range order. Next, we go through every hexagon α in this periodic structure and modify the spin components: $S_1^x \to \eta S_1^x$, $S_2^y \to \eta S_2^y$, $S_3^z \to \eta S_3^z$, $S_4^x \to \eta S_4^x$, $S_5^y \to \eta S_5^y$, and $S_6^z \to \eta S_6^z$, where $\mathbf{S}_{1,\cdots,6}$ are the six spins surrounding the α-th hexagon. Note that the eight directions $(\pm a, \pm b, \pm c)$ correspond to the same $\hat{\mathbf{n}}$ as they are related by flipping the η variable. It is thus similar to the director in nematic liquid crystal.

Since different ground states are labeled by discrete Ising variables $\{\eta_\alpha\}$, it raises the question whether the ground-state manifold is fully connected. The issue here is how one can move from one ground state *continuously* to another, as simply changing η requires flipping spin component which is a discrete process. It turns out continuous transformation of $\{\eta_\alpha\}$ can be achieved with the aid of the directional vector $\hat{\mathbf{n}} = (a, b, c)$. To see this, we first note that each η_α is associated with only *one* component of the unit vector $\hat{\mathbf{n}}$ in the ground state. Take the hexagon shown in Fig. 4.1 as an example. According to the ground-state rule, the local η only controls the 'a'-component of the six spins in this hexagon. As a result, all η-variables can be divided into three groups: type-A

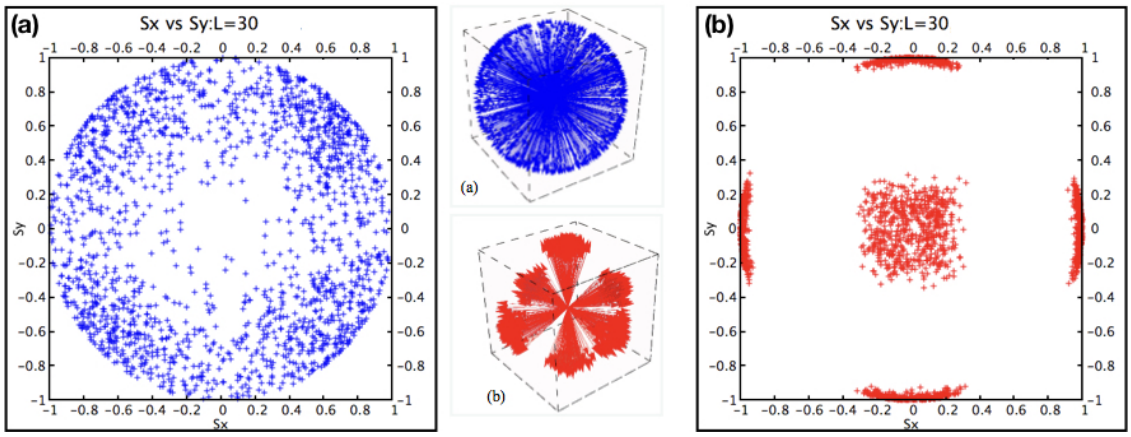

Figure 4.3: Snapshots of spin configurations above and below $T_c = 0.0401|\Gamma|$: (a) $T = 0.05$ and (b) $T = 0.03$. In the low-T phase, spins predominately point toward the six cubic directions.

(respectively, B and C) for spin-components controlled by a (respectively, b and c). When one of the component of $\hat{\mathbf{n}}$ vanishes, 1/3 of the η becomes idle. This feature allows us to construct a continuous path from one set of η to another one η' by rotating $\hat{\mathbf{n}}$ according to the sequence: $(a, b, c) \to (0, b', c') \to (a'', 0, c'') \to (a''', b''', 0) \to (a, b, c)$. After the first rotation, the vanishing a component allows us to change 1/3 of the η variables (those associated with a-component) to their counterpart in η'. Repeating similar process for the other two sets of η then completes the transformation from η to η' while keeping the $\hat{\mathbf{n}}$ vector in the same direction.

4.5 Emergent phase: Order by disorder

The above discussion also shows that without the rotational symmetry of $\hat{\mathbf{n}}$, different $\{\eta_\alpha\}$ becomes disjoint from each other. Interestingly, our MC simulations find a freezing phenomenon of the vector $\hat{\mathbf{n}}$ at a very low temperature $T_c \approx 0.04\,|\Gamma|$, as demonstrated in Fig. 4.3. At $T > T_c$, the spins and $\hat{\mathbf{n}}$ exhibit an emergent spherical symmetry even at temperatures well below the exchange energy scale $|\Gamma|$. This rotational symmetry is lost below T_c, and spins mainly point toward the six cubic axes, or equivalently the directional vector freezes to one of the cubic directions, i.e. $\hat{\mathbf{n}} \sim (1, 0, 0)$, $(0, 1, 0)$, or $(0, 0, 1)$. As states parameterized by different $\hat{\mathbf{n}}$ are degenerate at the mean-field level, the cubic directions are selected by thermal fluctuations through the order-by-disorder mechanism. This can also be viewed as the entropic selection, resulting from an effective

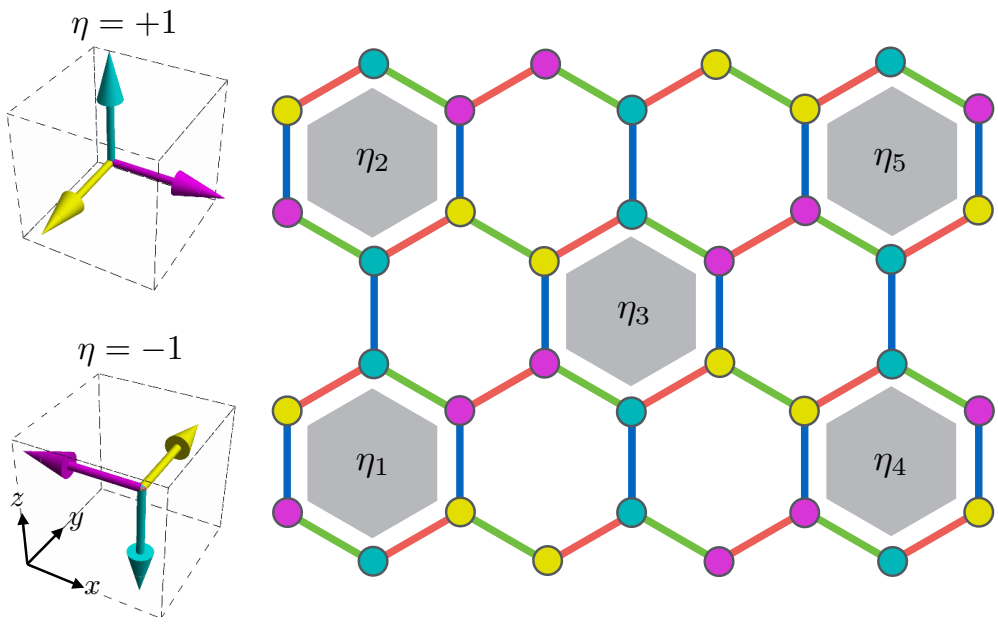

Figure 4.4: Plaquette order of hexagonal fluxes on honeycomb lattice. Shaded hexagons have nonzero flux $W \sim 1$, while empty hexagons have a vanishing W. Spins are orthogonal to each other (with left handedness for $\zeta = -1$) on each shaded hexagon; their specific directions depend on the local η, as specified in the insets. The arrangement of hexagons with finite W corresponds to the famous $\sqrt{3} \times \sqrt{3}$ long-range order. Spins remain disordered due to uncorrelated η_α on the shaded hexagons.

free energy $\mathcal{F}_{\text{ani}} \propto -(a^4 + b^4 + c^4)$. Indeed, simple analysis in section 4.6 shows that these cubic directions allow for the largest number of zero modes at the harmonic level. We note that similar cubic anisotropy is also generated by quantum fluctuations [73].

As discussed above, there is a phase transition driven by thermal order-by-disorder at a low temperature $T \approx 0.04$. However, this is a rather weak phase transition over a narrow temperature window. Numerically, it is quite easy to miss this transition in Monte Carlo simulations. Our first hint of a possible phase transition at low temperatures is from the analysis of the autocorrelation function defined as

$$A(t) = \frac{1}{N} \sum_{i}^{N} \langle \mathbf{S}_i(t) \cdot \mathbf{S}_i(0) \rangle. \tag{4.2}$$

Here time t is measured in Monte Carlo sweeps. Fig. 4.5 shows the auto-correlation function obtained from Monte Carlo simulations at various temperatures. At small t, the auto-correlation function $A(t)$ decays exponentially. We then fit the different auto-correlation curves with the

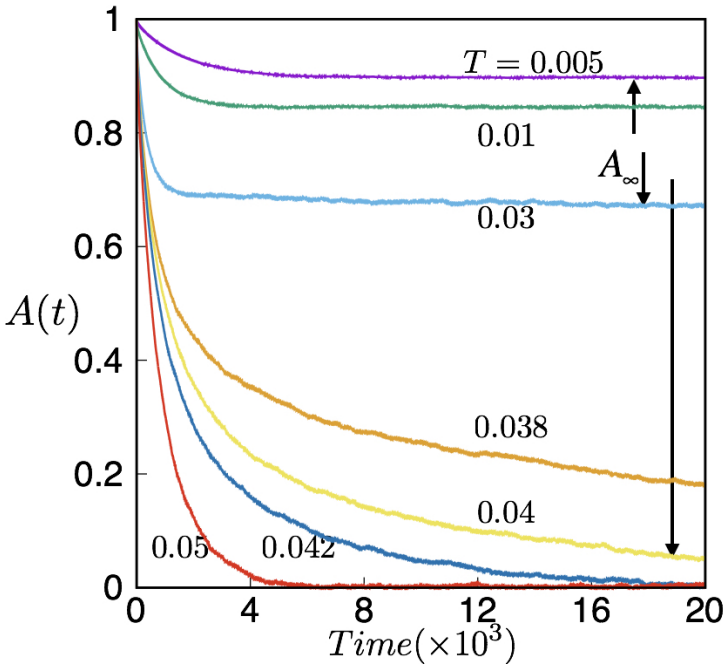

Figure 4.5: Auto-correlation function $A(t)$ obtained from Monte Carlo simulations at different temperatures. A_∞ represents the steady-state value at large t, which corresponds to 20,000 Monte Carlo sweeps numerically.

following simple function: $A(t) = A_\infty + B\,\exp(-t/\tau)$, where A_∞ is the steady-state value as $t \to \infty$, and τ is a relaxation time. The temperature dependence of A_∞ is shown in Fig. 4.6. For $T > T_c$, we find $A(t) \to 0$ at large time $t \to \infty$. On the other hand, for $T < T_c$, the auto-correlation function approaches a finite steady-state value A_∞, indicating the presence of long-range order.

4.6 Zero Mode and Specific Heat

For a given ground-state configuration $\{\mathbf{S}_i\}$, we introduce local reference frame $(\hat{\mathbf{e}}_i^x, \hat{\mathbf{e}}_i^y, \hat{\mathbf{e}}_i^z)$, such that $\hat{\mathbf{e}}_i^z$ is parallel to the spin direction $\mathbf{S}_i$. Next we consider small transverse spin fluctuations parameterized by $\sigma_i = (\sigma_i^x, \sigma_i^y)$ such that

$$\mathbf{S}_i \approx S(1 - |\sigma_i|^2/2S^2)\,\hat{\mathbf{e}}_i^z + \sigma_i^x\,\hat{\mathbf{e}}_i^x + \sigma_i^y\,\hat{\mathbf{e}}_i^y. \tag{4.3}$$

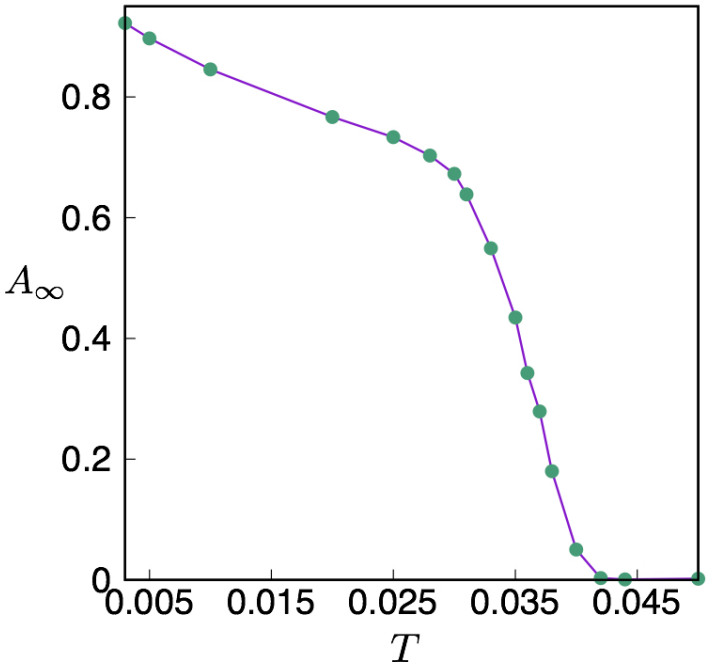

Figure 4.6: Temperature dependence of A_∞ (See in Fig:4.5). The finite value A_∞ decreases with increasing temperature and goes to zero at the transition temperature T_C.

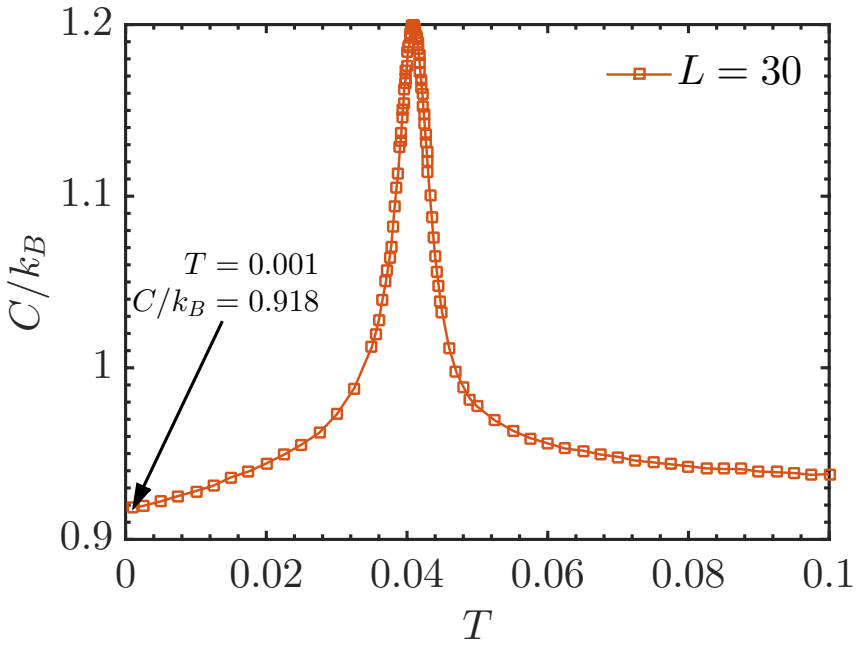

Figure 4.7: Temperature dependence of specific heat C obtained by Monte Carlo simulations.

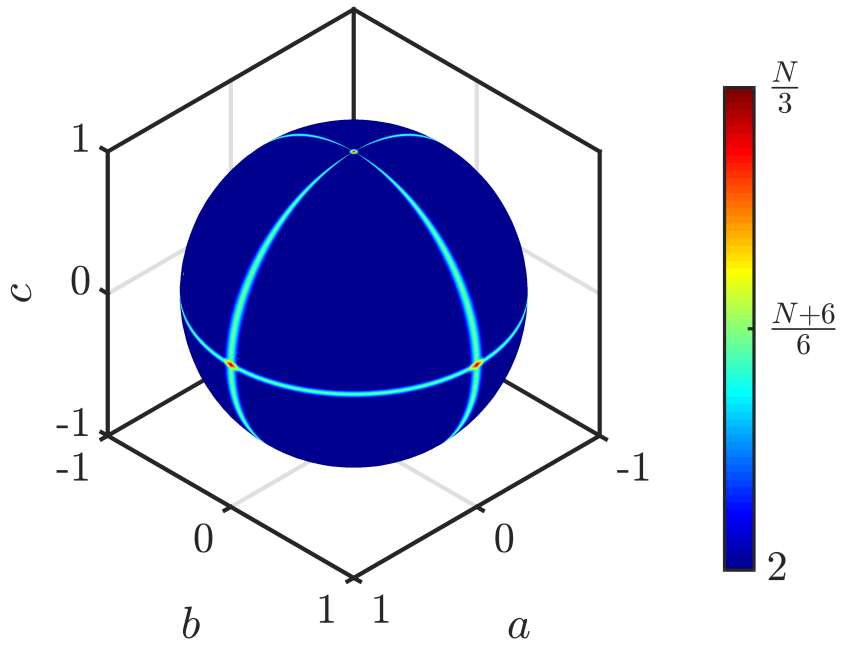

Figure 4.8: Zero mode number, $\mathcal{N}_0$, as a function of ground state parameters (a, b, c).

Substituting this expansion into the Hamiltonian, the energy of the system can be expressed, up to quadratic order in σ:

$$E(\sigma_i) = -N\Gamma + \sum_{im,jn} M_{i\alpha,j\beta}\, \sigma_i^m\, \sigma_j^n, \tag{4.4}$$

where $N = 2L^2$ is the total number of spins in the $L \times L$ honeycomb lattice and M is a $2N \times 2N$ matrix representing interactions of the spin fluctuations σ_i.

The spectrum $\{\varepsilon_\ell\}$ of the harmonic fluctuations is obtained by diagonalizing the M matrix. Here we are particularly interested in the number $\mathcal{N}_0$ of zero modes ($\varepsilon_\ell = 0$), since this number provides a measure of the softness of spin fluctuations around a given ground state. As discussed in the before, a ground state of the Γ model is parameterized by a unit vector $\hat{\mathbf{n}} = (a, b, c)$ and a set of Ising variables $\{\eta_\alpha\}$. The discrete Ising variables correspond to Gauge degrees of freedom and do not affect the energy of the system (However, they do affect the dynamics of the system). Consequently, in the following we set $\eta_\alpha = +1$ and only consider the dependence of fluctuation spectrum

on the orientation of the directional vector $\hat{\mathbf{n}} = (a, b, c)$. By direct diagonalisation of M for a finite lattice, the number of zero modes $\mathcal{N}_0$ in the degenerate ground-state manifold parametrized by (a, b, c) is shown in Fig. 4.8.

Three different cases can be identified in Fig. 4.8: (1) if $a, b, c \neq 0$, then $\mathcal{N}_0 = 2$, which corresponds to the trivial 2-dimensional global rotation of $\hat{\mathbf{n}} = (a, b, c)$. (2) if two of a, b, c are nonzero while the third one vanishes, then $\mathcal{N}_0 = 2 + \frac{N-6}{6}$. And finally, (3) if only one of a, b, c is nonzero, then the number of zero modes is $\mathcal{N}_0 = 2 + 2\frac{N-6}{6}$. The additional degeneracies in cases (2) and (3) are related to the number of hexagons with idle η. In such situations, a local zero mode is associated with each idle hexagon. This simple analysis shows that the cubic directions $\hat{\mathbf{n}} = (1, 0, 0)$, $(0, 1, 0)$, and $(0, 0, 1)$ have softer spin fluctuations and will be favored entropically.

The number of zero modes is also related to the specific heat of the degenerate manifold. According to equipartition theorem, each harmonic mode contributes $k_B/2$ to the heat capacity. On the other hand, the zero modes discussed above are obtained within the harmonic approximation. Taking into account higher order terms, these modes are expected to behave generically according to $\epsilon(x) \sim kx^4$, where x is the mode amplitude. Direct calculation shows that such soft mode contributes $k_B/4$ to the heat capacity [17]. Consequently, the specific heat is given by

$$\frac{C}{k_B} = \lim_{N\to\infty} \left(\frac{2N - \mathcal{N}_0}{N} \frac{1}{2} + \frac{\mathcal{N}_0}{N} \frac{1}{4} \right) \tag{4.5}$$

When $T \to 0$, cubic axes are preferred, $\mathcal{N}_0 = 2 + 2\frac{N-6}{6}$, thus $C/k_B = \frac{11}{12} \approx 0.917$, which is consistent with the simulated value, 0.918 at $T = 0.001$ (Fig. 4.7).

4.7 Emergent plaquette Order

It is crucial to note that although the spin-symmetry is seemingly reduced from spherical to cubic when crossing T_c, this cannot be viewed as a true reduction of symmetries as the Γ model itself is already cubic-symmetric. The apparent spherical symmetry at $T_c < T < |\Gamma|$ is an *emergent* property of the phase, which is due to spatial fluctuations of directional vector $\hat{\mathbf{n}}(\mathbf{r})$. Another im-

portant observation is that while the degeneracy associated with $\hat{\mathbf{n}}$ is lifted by thermal fluctuation, a discrete macroscopic degeneracy persists due to the Ising gauge symmetry of $\{\eta_\alpha\}$, especially for classical spins. Consequently, spins remain disordered at $T < T_c$.

To resolve this issue and investigate the nature of the low-T phase, we first note that the cubic spin-orbital symmetry of the Γ model is indeed broken below T_c, yet in a complicated pattern: local spins have to pick one of the six cubic directions in a coordinated way while preserving the gauge symmetry of $\{\eta_\alpha\}$. A convenient local quantity to characterize the broken symmetry is the flux variable defined on each hexagon [4]:

$$W_\alpha = S_1^x\, S_2^y\, S_3^z\, S_4^x\, S_5^y\, S_6^z, \tag{4.6}$$

where $\mathbf{S}_{1,\cdots,6}$ are the six spins around the α hexagon. These fluxes play an important role in the spin-1/2 Kitaev model as they are "integrals of motion" of the Hamiltonian [4]. In our case, the flux W_α is similarly a gauge-invariant variable, that is independent of η_α. On the other hand, it can be used to characterize the ordering of $\hat{\mathbf{n}}$. To see this, we note that in the ground state, they only take on three different values [73]: $W_{\rm A} = \zeta a^6$ for hexagons whose η is associated with component a, and similarly $W_{\rm B} = \zeta b^6$ and $W_{\rm C} = \zeta c^6$ for the other two sets of hexagons, where $\zeta = -\mathrm{sgn}(\Gamma)$. As $\hat{\mathbf{n}}$ freezes to one of the cubic directions, 2/3 of the fluxes also vanish. Since hexagons of a given type form an enlarged triangular lattice, the flux patten of the low-T phase, e.g. $W_A \approx 1$, and $W_B \approx W_C \approx 0$, corresponds to a broken translation symmetry; see Fig. 4.4. Importantly, the uncorrelated η_α on hexagons with nonzero W give rise to a disordered spin configuration. We note in passing that plaquette orders with similar spatial pattern also exist as ground state in J_1-J_2 quantum $S = 1/2$ and $S = 1$ honeycomb Heisenberg model [75–78]. Our finding shows a rare example of plaqutte ordering hidden in a classical spin liquid on honeycomb lattice.

The arrangement of hexagons with nonzero W shown in Fig. 4.4 suggests an order parameter

$$\tilde{W}(\mathbf{Q}) = \frac{1}{N}\sum_\alpha W_\alpha\, e^{i\mathbf{Q}\cdot\mathbf{r}_\alpha}, \tag{4.7}$$

which is the Fourier transform at wavevector $\mathbf{Q} = (4\pi/3, 0)$, corresponding to $\sqrt{3} \times \sqrt{3}$-order, for characterizing the broken translation symmetry. A scalar order parameter is computed from the Monte Carlo average of the Fourier component $\tilde{Q}(\mathbf{Q})$:

$$\Phi = \langle |\tilde{W}(\mathbf{Q})| \rangle, \tag{4.8}$$

We then performed extensive Monte Carlo simulations on systems with different size L = 30, 60, 90, 120 and 150 at temperatures around T_c to examine the critical behaviors; the results are summarized in Fig. 4.9 reveal a clear phase transition. The specific heat shows clear finite-size effect. Here the specific heat is computed according to the variance of energy $\mathcal{H}$ obtained from Eq. 4.1 as given in eq 4.9.

$$C = \frac{\langle \mathcal{H}^2 \rangle - \langle \mathcal{H} \rangle^2}{NT^2} \tag{4.9}$$

The bracket $\langle ... \rangle$ donates the Monte Carlo average.

The susceptibility and Binder cumulant of the order parameter are defined as

$$\chi = N \frac{\langle |\tilde{W}(\mathbf{Q})|^2 \rangle - \langle |\tilde{W}(\mathbf{Q})| \rangle^2}{T} \tag{4.10}$$

$$B_4 = 1 - \frac{\langle |\tilde{W}(\mathbf{Q})|^4 \rangle}{3 \langle |\tilde{W}(\mathbf{Q})|^2 \rangle^2} \tag{4.11}$$

In the ground state, it is expected that $\Phi = 1/3$ and $B_4 = 2/3$. This was confirmed by our simulation at low temperature. The specific heat C and the susceptibility χ exhibit finite size effects, where the peaks grow with increasing lattice size L.The scalar order parameter exhibits characteristics of a second-order phase transition. The growth of the order parameter Φ below T_c becomes sharper for large L systems, characteristic of a second-order phase transition. The crossing point of the Binder cumulant curves indicates that $T_c \simeq 0.0402|\Gamma|$, which further confirms

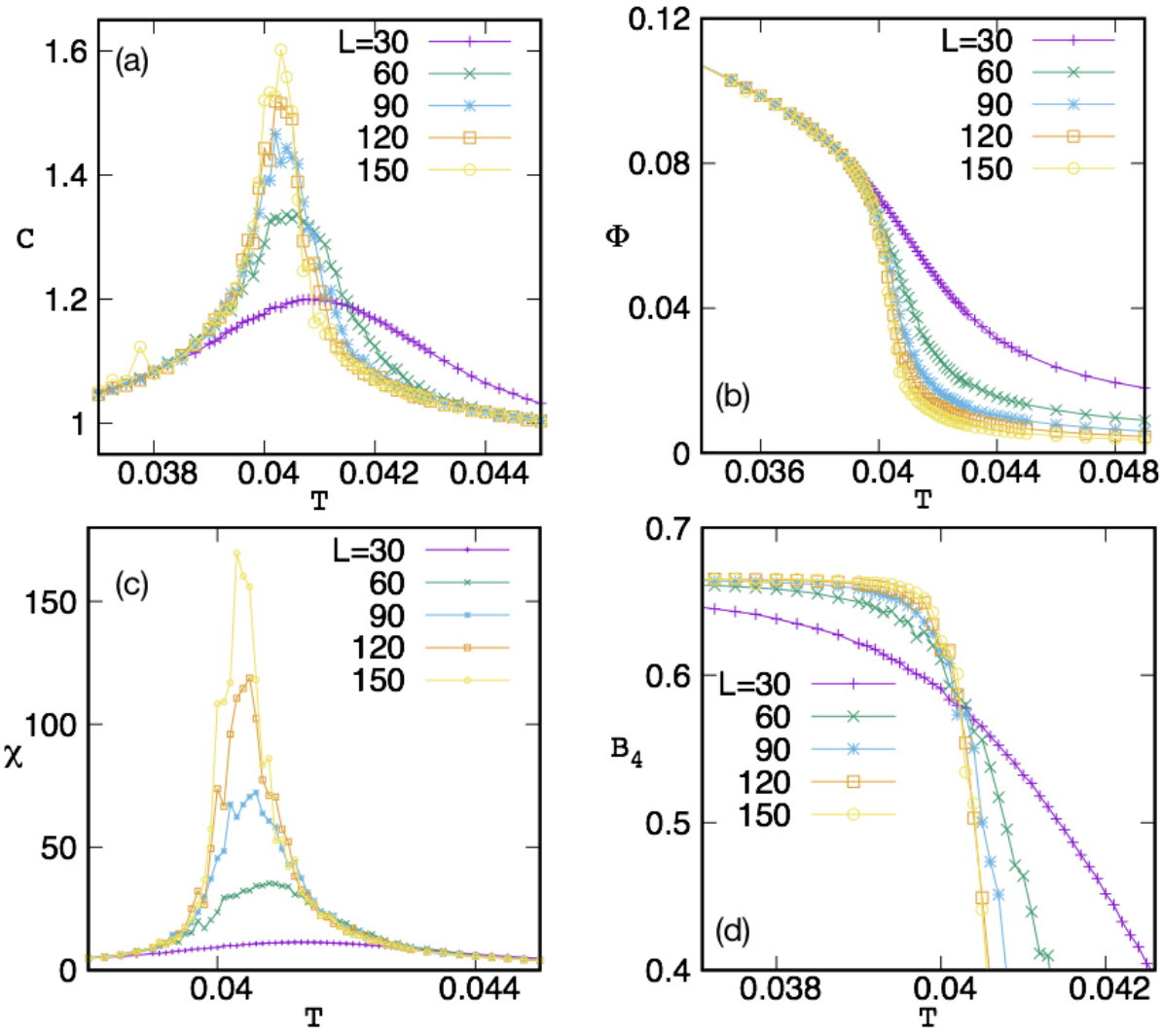

Figure 4.9: Monte Carlo simulation of the translation symmetry breaking of flux variables. (a) specific heat C, (b) order parameter $\Phi = \langle|\tilde{W}(\mathbf{Q})|\rangle$. The crossing point of the Binder curves gives an estimate of $T_c \approx 0.0402$. Critical exponents of the transition are obtained from finite-size scaling: $\alpha = 0.167$, $\beta = 0.177$, $\gamma = 1.47$, and $\nu = 0.863$.

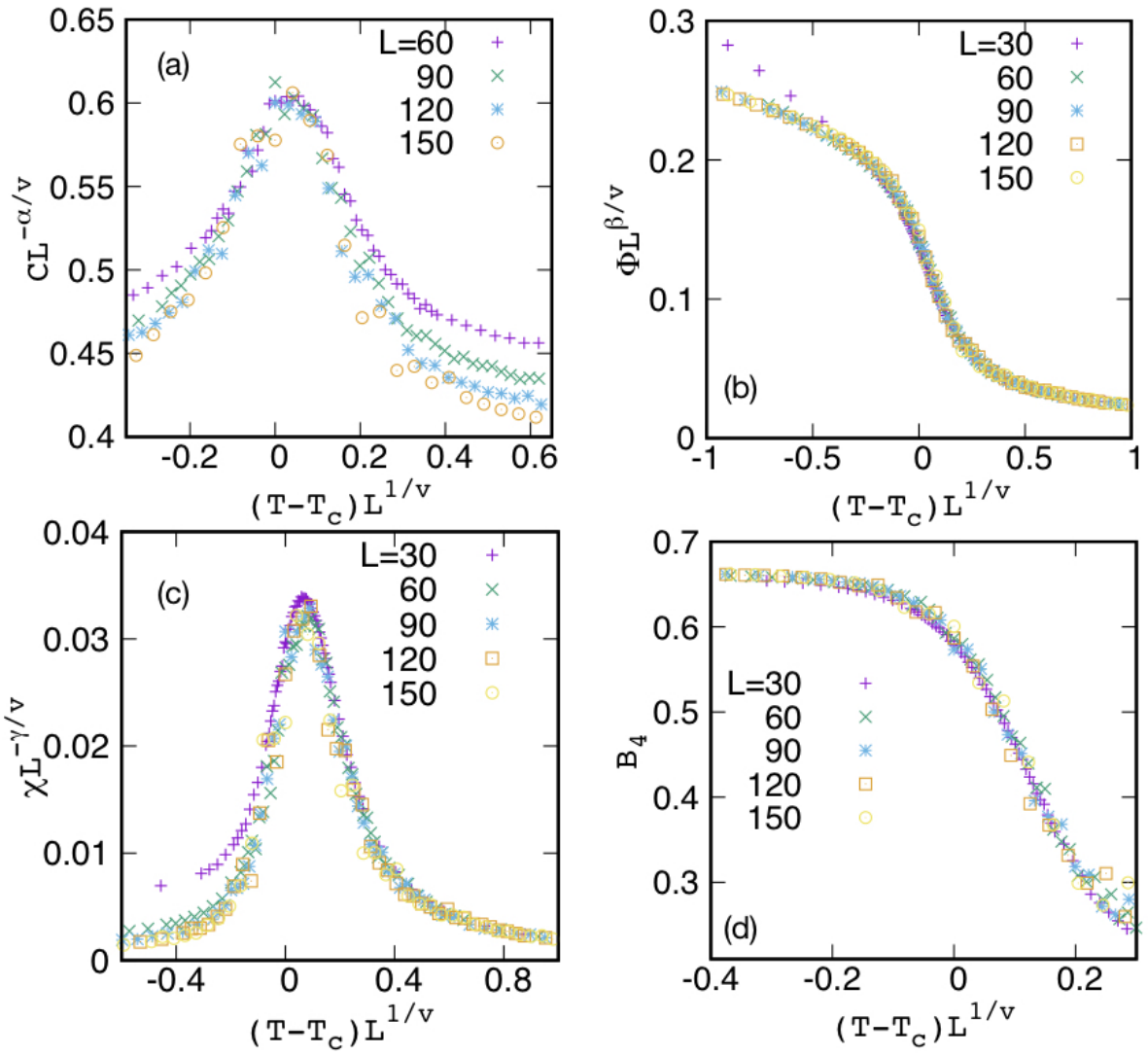

Figure 4.10: Collapsing of the finite size scaled data. (a) specific heat C, (b) order parameter Φ (c) the corresponding susceptibility χ, (d) Binder cumulant B_4 as functions of scaled temperature.

a continuous phase transition see Figure 4.10.

Our finite-size scaling analysis produces fairly reasonable data-points collapsing (Figure 4.10), further supporting a second-order phase transition at T_c. The critical exponents of this phase transition are determined from finite size scaling analysis by following standard procedures. Results of the scaled data shown in Fig. 4.10. For example, the exponent ν can be determined from the data collapsing of B_4 versus scaled temperature $L^{1/\nu}(T - T_c)$. The slope of linear fitting the maximum values of specific heat $C_{\max}$ as a function of lattice size L gives the value of α/ν. The ratios γ/ν

and β/ν are obtained similarly from the χ and Φ curves. We obtain the following critical exponents: $\alpha = 0.167$, $\beta = 0.177$, $\gamma = 1.47$, $\nu = 0.863$. These exponents also satisfy the hyperscaling relation $\alpha + 2\beta + \gamma = 2$. As shown in Fig. 4.10, fairly nice data collapsing is obtained using this set of critical exponents. Since the plaqute-ordering is intimately related to a broken Z_3 symmetry, some of the critical exponents, e.g. ν and γ, obtained from finite-size scaling, shown in caption of Fig. 4.10, are consistent with the 2D 3-state Potts universality class [79], although others show noticeable deviations. This discrepancy could be due to the gauge degrees of freedom $\{\eta_\alpha\}$, which might have nontrivial effects on the critical behavior.

4.8 Static Structure Factor simulations

We can describe the static structure factor by the following correlation function,

$$\mathcal{S}(\mathbf{q}, 0) = \langle \mathbf{S}_\mathbf{q}(0) \cdot \mathbf{S}^*_\mathbf{q}(0) \rangle \tag{4.12}$$

where $\langle \cdots \rangle$ denotes the ensemble average over independent initial states of a given temperature. and $\mathbf{S}_\mathbf{q}$ represents the spatial Fourier transform of the instantaneous spin configuration in three dimensional complex vector form.

$$\mathbf{S}_\mathbf{q} = \frac{1}{\sqrt{N}} \sum_i \mathbf{S}_i(t=0) \exp(i\mathbf{q} \cdot \mathbf{r}_i) = \mathbf{C} + i\mathbf{S} \tag{4.13}$$

Then,

$$\mathcal{S}(\mathbf{q}, 0) = \langle \mathbf{C} - i\mathbf{S} | \mathbf{C} + i\mathbf{S} \rangle \tag{4.14}$$

The structure factor is computed from the Fourier transform of the spin configuration, i.e. $\mathcal{S}(\mathbf{q}) = |\frac{1}{N} \sum_i \mathbf{S}(\mathbf{q}) \exp(i\mathbf{q} \cdot \mathbf{r}_i)|^2$. We plot the ensemble average of $\mathcal{S}(\mathbf{q}) = \mathbf{C}^2 + \mathbf{S}^2$. Where $\mathbf{q} = \frac{m}{L}\mathbf{b_1} + \frac{n}{L}\mathbf{b_2}$ the reciprocal lattice wave vectors and position vector of each spin $\mathbf{r}$ gives us the phase values $\exp(i\mathbf{q} \cdot \mathbf{r}_i)$ corresponding to each $\mathbf{q}$. Both m and n belong in the range $0 \leq m < L$ and $0 \leq n < L$ where L is the linear honeycomb lattice size.

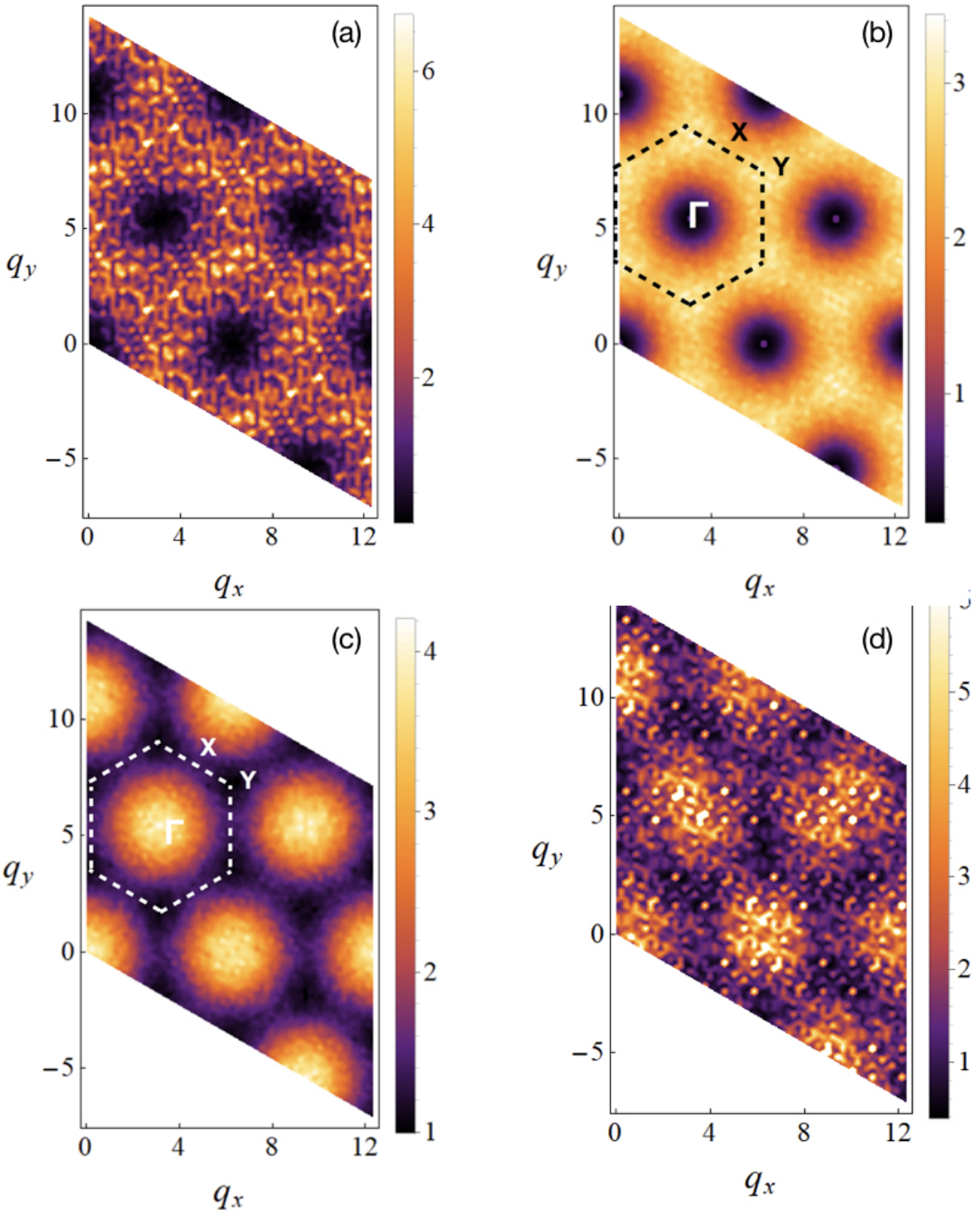

Figure 4.11: Static structure factor $\mathcal{S}(\mathbf{q})$ in the extended Brillioun zone for the Γ model at low temperatures obtained from Monte Carlo simulations. Panels (a) and (b) are computed at $T = 0.03$ and $T = 0.05$ respectively for antiferromagnetic $\Gamma > 0$. Similar results for ferromagnetic $\Gamma < 0$ are shown in (c) $T = 0.03$, (d) $T = 0.05$.

Fig. 4.11 shows the static structure factor $\mathcal{S}(\mathbf{q})$ of the Γ model at low temperatures for both antiferromagnetic and ferromagnetic Γ. Importantly, the system exhibits rather distinct structure factors above and below the critical T_c for both signs of Γ. We can see for the antiferromagnetic case i.e. $\Gamma > 0$ (Fig. 4.11(a) and (b)) the minimum spectral weight lies at the Γ point in the brillioun zone(BZ). We see the characteristic development of dark nearly circular patches at the centers of the extended BZ especially at temperatures greater than T_C. Intensity starts to concentrate on the boundaries of the BZ. For $T < T_C$ spectral intensity outside the Γ point dark circular patch looks uniform for rest of the BZ. For $T > T_C$ focusing on the bright BZ boundary regions, the maximum spectral weight is found at the Y point, with a decrease in magnitude as we move towards the X point, and a uniform drop-off as we move from the Y point to the Γ point origin of BZ. Static structure factors for ferromagnetic interaction($\Gamma < 0$) exhibit complete antipodal characteristics from its antiferromagnetic counterpart. We see in Fig. 4.11(c) and (d) spectral intensity has its maxima at the BZ centers. Intensity decreases as we move closer to the edges of the extended BZ. For $T > T_C$ it is clearly visible that towards the edge of the BZ, intensity decreases when we move from X point to Y point.

4.9 Spin dynamics

In this section we will discuss the details of the dynamical behaviors of the spin liquids above and below the critical T_c. To this end, we employ the semiclassical Landau-Lifshitz (LL) dynamics simulation, which has been successfully applied to compute the dynamical structure factor of various classical spin liquids [17, 80, 81]. For $T > T_c$, MC simulations are used to prepare initial states sampled from the Boltzmann distribution. We then perform energy-conserving LL simulation 4.15 to obtain trajectories of spins $\mathbf{S}_i(t)$.

$$\frac{d\mathbf{S}_i}{dt} = -\mathbf{S}_i \times \frac{\partial \mathcal{H}}{\partial \mathbf{S}_i}, \tag{4.15}$$

where $\mathcal{H}$ is the Hamiltonian of the Γ model. Here we do not include dissipation terms such as

the Gilbert damping in our dynamical simulations, since we are interested in the un-damped oscillations of the excited states. The excitation energies can be extracted from these oscillations through simple time-domain Fourier transform. An efficient semi-implicit algorithm [31] is employed to integrate the above LL equation. The high efficiency of the algorithm comes from fact that it preserves the spin length at every time step and the energy values are well conserved with time irrespective of the time length or time step size in the simulation. In our computations of the structure factor, we consider a honeycomb lattice with 2×30^2 spins. A time step $\delta t = 0.005$ is used (with $|\Gamma| = 1$).

The dynamical structure factor $\mathcal{S}^{\alpha\beta}(\mathbf{q}, \omega)$ is computed from the Fourier transform of the real-space correlator $\langle S_i^\alpha(t) S_j^\beta(0)\rangle$, where $\alpha, \beta = x, y, z$, averaged over the initial states. As discussed above, since ground states parameterized by different $\{\eta_\alpha\}$ are disconnected below T_c, an additional average over random $\{\eta_\alpha\}$ is introduced manually to improve the efficiency. It is worth noting that the dependence of $\mathcal{S}(\mathbf{q}, \omega)$ on temperature mainly comes from different initial state sampling.

To compute the $\mathcal{S}(\mathbf{q}, \omega)$ at a given temperature T, we first perform Monte Carlo simulations to sample equilibrium spin configuration at T. These spin states are then used as the initial condition for the LL dynamical simulations, i.e. $\mathbf{S}_i(t = 0) = \mathbf{S}_i^{(\mathrm{eq})}(T)$. Next, we perform dynamical simulations based on LL equation to generate snapshots of the system $\mathbf{S}_i(t_n)$ at different times $t_n = n\,\Delta t$, where $\Delta t = 10\delta t$ is used. From these spin configurations, we compute the space-time Fourier transform:

$$\mathbf{S}(\mathbf{q}, \omega) = \frac{1}{N} \sum_i \int_0^T \mathbf{S}_i(t) e^{i\mathbf{q}\cdot\mathbf{r}_i}\, e^{-i\omega t} dt \tag{4.16}$$

Here the integral over time is approximated by the discrete Riemann summation, and the upper limit $T = 500$ is used. Due to periodic boundary condition used in our finite size simulations, we consider only wavevectors $\mathbf{q} = \frac{m}{L}\mathbf{b}_1 + \frac{n}{L}\mathbf{b}_2$, where m, n are integers and $\mathbf{b}_1$, $\mathbf{b}_2$ are the primitive vectors of the reciprocal lattice.

The diagonal part of the dynamical structure factor $\mathcal{S}(\mathbf{q}, \omega) \equiv \sum_\alpha \mathcal{S}^{\alpha\alpha}(\mathbf{q}, \omega) = |\mathbf{S}(\mathbf{q}, \omega)|^2$ are

shown in Fig. 4.12 for the two spin liquid phases for both ferromagnetic and antiferromagnetic interactions in different temperature regimes along a few high-symmetry directions in the Brillouin zone. The $\mathcal{S}(\mathbf{q},\omega)$ at $T > T_c$ shows broad continuum over a wide energy range in both cases. On the other hand, structures of coherent quasi-particle dispersion can be seen at high energies for $\mathcal{S}(\mathbf{q},\omega)$ in the low-T phase. These coherent excitations in a liquid phase are reminiscent of the electron pseudo-bands observed in liquid metals [82, 83]. Their origin can be traced to the robust local or short-range ordering in a liquid state.

In each figure we have averaged over 100 different initial states for a 30×30 unit cells (1800 spins). It is expected that like the static structure factor graphs which are analogous to $\omega = 0$ we see a minima in spectral weight at Γ point in the BZ for AFM case and a maxima for the FM case. We also see sharp band structure like features at low temperatures which fade away at higher temperatures. For both AFM and FM dynamical structure factors, the intensity accumulates most prominently around the Γ point, and the line towards the K and M from Γ point holds equivalent spectral weight intensity for lower frequency region ($\omega < 1$). For temperatures lower than $T = 0.05$ the spectral intensity rapidly decreases in higher frequency region.

The off-diagonal dynamical structure factors $\mathcal{S}^{\alpha\beta}(\mathbf{q},\omega)$ are simulated from the equations and given in Figure 4.13,

$$\mathcal{S}^{\alpha\beta}(\mathbf{q},\omega) = \int_0^T \mathbf{S}_{\alpha\beta}(\mathbf{q}) e^{-i\omega t} dt \tag{4.17}$$

where $S_{\alpha\beta}(\mathbf{q}) = \mathbf{S}_\alpha(\mathbf{q})\mathbf{S}_\beta(-\mathbf{q}) + \mathbf{S}_\beta(\mathbf{q})\mathbf{S}_\alpha(-\mathbf{q})$.

Interestingly, the logarithmic plot of the off-diagonal $\mathcal{S}^{xy}(\mathbf{q},\omega)$, shown in Fig. 4.14(a), exhibits intriguing excitations associated with the high-symmetry points of the BZ. It is important to note that a large signal also exists at the same high-symmetry points in the *static* structure factor. These quasi-$\mathbf{q}$-independent features thus seem to derive from coherent oscillations of the underlying pla-

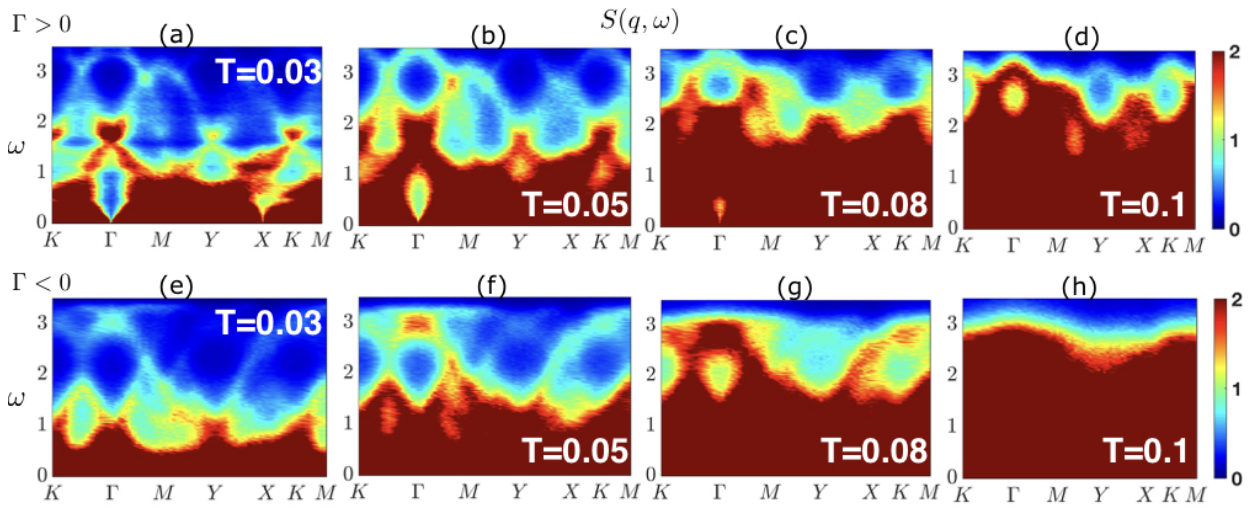

Figure 4.12: The diagonal part of the dynamical structure factor $\mathcal{S}(\mathbf{q},\omega) = \mathcal{S}^{xx}(\mathbf{q},\omega) + \mathcal{S}^{yy}(\mathbf{q},\omega) + \mathcal{S}^{zz}(\mathbf{q},\omega)$ computed from LL simulations for antiferromagnetic (top) and ferromagnetic (bottom) Γ model. Panels (a)-(d) show dynamical structure factors $\mathcal{S}(\mathbf{q},\omega)$ for $\Gamma < 0$ FM regime plotted for $T = 0.03$, 0.05, 0.08, 0.1 (from left to right). Panels (e)-(h) show the $\mathcal{S}(\mathbf{q},\omega)$ for $\Gamma > 0$ AFM regime plotted for same temperature values $T = 0.03$, 0.05, 0.08, 0.1 (from left to right).

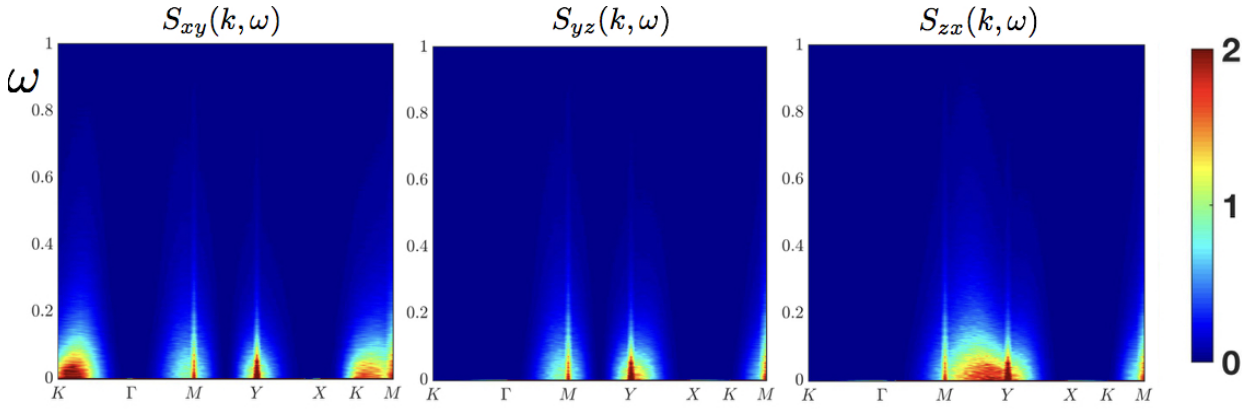

Figure 4.13: Off-diagonal dynamical structure factor $\mathcal{S}^{xy}(\mathbf{q},\omega)$ at T=0.01

quette pattern.

To further investigate the source of these excitations, we compute the dynamical structure factor of fluxes $\mathcal{W}(\mathbf{q},\omega)$, which is defined as the space-time Fourier transform of the correlation function $\langle W_\alpha(t)W_\beta(0)\rangle$ given by equation,

$$\mathcal{W}(\mathbf{q},\omega) = \int_0^T W(\mathbf{q})e^{-i\omega t}dt \tag{4.18}$$

Interestingly, as shown in Fig. 4.14(b), similar momentum-specific excitations are observed in the dynamical structure factor $\mathcal{W}(\mathbf{q},\omega)$. In addition to the long-range order at the K-point, the finite excitations associated with the Γ point result from the non-zero average $\langle W\rangle \approx 1/3$ of the $\sqrt{3}\times\sqrt{3}$ flux patterns, e.g. $W_A \approx 1$, and $W_B \approx W_C \approx 0$. Fig. 4.14(c) and its inset show the ω dependence of the dynamical excitations $\mathcal{W}(\mathbf{Q},\omega)$ with momentum fixed at $\mathbf{Q} = (4\pi/3, 0)$, corresponding to the K point. Significant differences in the overall behavior can be seen in the two temperature regimes above and below the critical T_c, in particular see the inset semi-log plot. Importantly, we find distinct power-law behaviors $\mathcal{W}(\mathbf{Q},\omega) \sim 1/\omega^a$ in the two spin-liquid phases, with the exponent $a \approx 1.5$ at high temperatures, and $a \approx 1.22$ in the flux-ordered phase. These finite energy excitations at the ordering wavevector $\mathbf{Q}$ reflect the composite nature of the flux variables that develop a long range order below T_c. Notably, they are in stark contrast to the dispersive Goldstone modes of simple long-range magnetically ordered states.

Next we examine dynamical structure factors of low-T states that arise from possible quantum order by disorder on the η degrees of freedom. As discussed in Ref. [73], real-space perturbation calculation gives rise to an effective interaction among the Ising variables η_α:

$$\mathcal{H}_{\text{Ising}} = \epsilon\,\Gamma \sum_{\langle\alpha\beta\rangle}{}' \eta_\alpha\,\eta_\beta \tag{4.19}$$

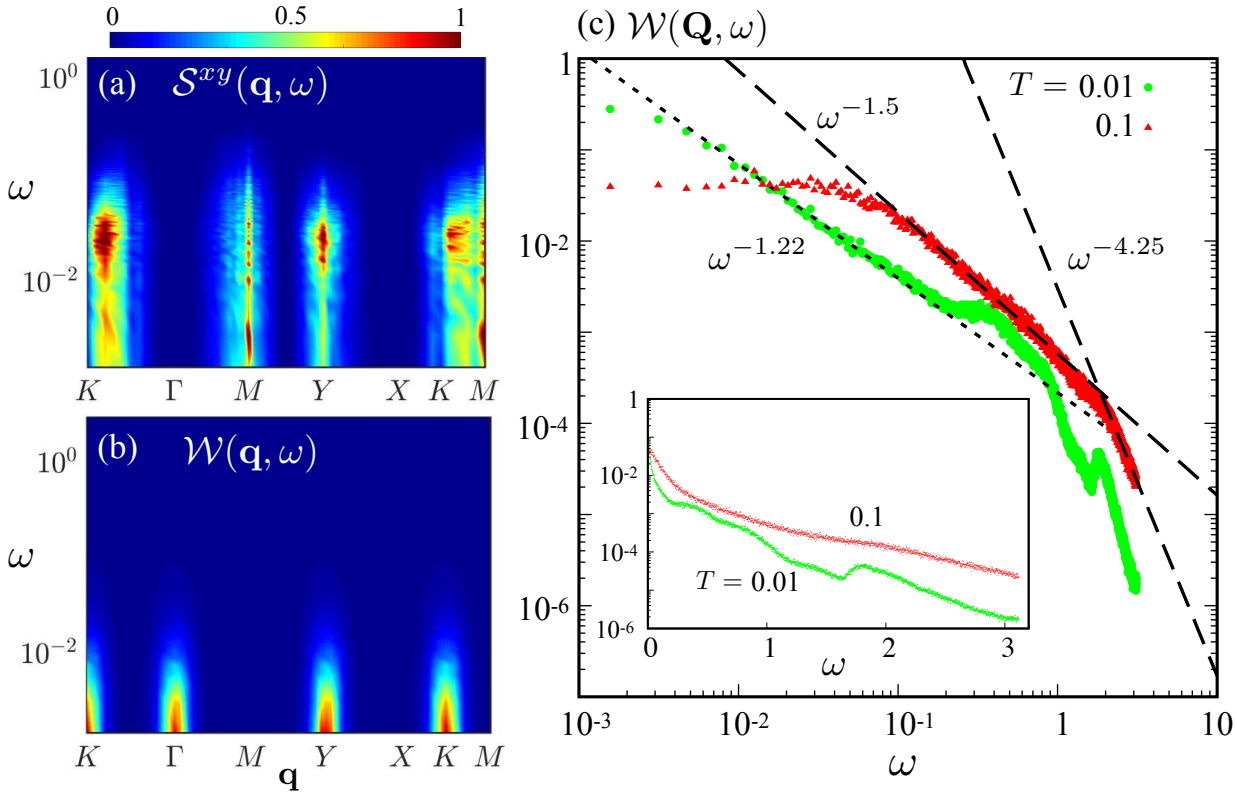

Figure 4.14: (a) Off-diagonal dynamical structure factor $\mathcal{S}^{xy}(\mathbf{q},\omega)$ in logarithmic scale. (b) Dynamical structure factor of flux variables $\mathcal{W}(\mathbf{q},\omega)$ in logarithmic scale. Also note the log-scale for the ω axis. (c) The ω dependence of the flux dynamical structure factor $\mathcal{W}(\mathbf{Q},\omega)$ at the $\sqrt{3}\times\sqrt{3}$ ordering wavevector $\mathbf{Q}$ for both high and low-T spin liquid phases.

Here ϵ is a positive numeric constant, the prime indicates that the summation is over hexagons with *nonzero* average flux, i.e. $\langle W_\alpha \rangle \neq 0$, which form an enlarged triangular lattice, and $\langle \alpha\beta \rangle$ denotes nearest-neighbor pair on the triangular lattice. The triangular lattice formed by hexagons with nonzero W corresponds to the $\sqrt{3} \times \sqrt{3}$ pattern. The above Hamiltonian Eq. (4.19) thus describes an triangular Ising model with effective nearest-neighbor interaction $J_{\text{eff}} = \epsilon\Gamma$.

In the case of *ferromagnetic* $\Gamma < 0$, the effective interaction in Eq. (4.19) leads to a uniform ordering of the η variables, namely all $\eta_\alpha = +1$ or $\eta_\alpha = -1$. The long-range ordering of the Ising variables combined with the plaquette ordering of the fluxes, which is equivalent to the ordering of the directional vector $\hat{\mathbf{n}} = (a, b, c)$, give rise to a long-range spin order of the $\sqrt{3} \times \sqrt{3}$ type. Fig. 4.15 shows the dynamical structure factor $\mathcal{S}(\mathbf{q}, \omega)$ of this $\sqrt{3} \times \sqrt{3}$ spin order with FM Γ-interaction, obtained from our LL dynamical simulations. Small deviations are introduced to the perfect $\sqrt{3} \times \sqrt{3}$ order through Monte Carlo simulations at $T = 10^{-4}$. As expected for a state with long-range spin order, the $\mathcal{S}(\mathbf{q}, \omega)$ shows clear dispersions for the magnon quasiparticle excitations.

On the other hand, the effective Ising model Eq. (4.19) with *antiferromagnetic* $\Gamma > 0$ is a highly frustrated system, which is in fact one of the first studied geometrically frustrated magnets [25]. Essentially, since the AFM interaction between three Ising spins of an elementary triangle cannot be simultaneously satisfied, there is at least a frustrated bond with parallel Ising spins on *every* triangle. The number of degenerate ground states can be exactly computed using the transfer-matrix method [25]; it grows exponentially with the system size, giving rise to a nonzero entropy density of the degenerate ground states.

In order to compute the dynamical structure factor of the AFM Γ model, we perform Monte Carlo simulations on the effective Ising model (4.19) to sample degenerate ground-state configurations of the Ising variables η_α. A spin configuration is then constructed from these Ising variables and a particular choice of the directional vector, say $\hat{\mathbf{n}} = (1, 0, 0)$; see Fig. 4.16 for an example. Next we perform Monte Carlo simulations on the spin Γ-model Eq. (4.1) at $T = 10^{-4}$ in order

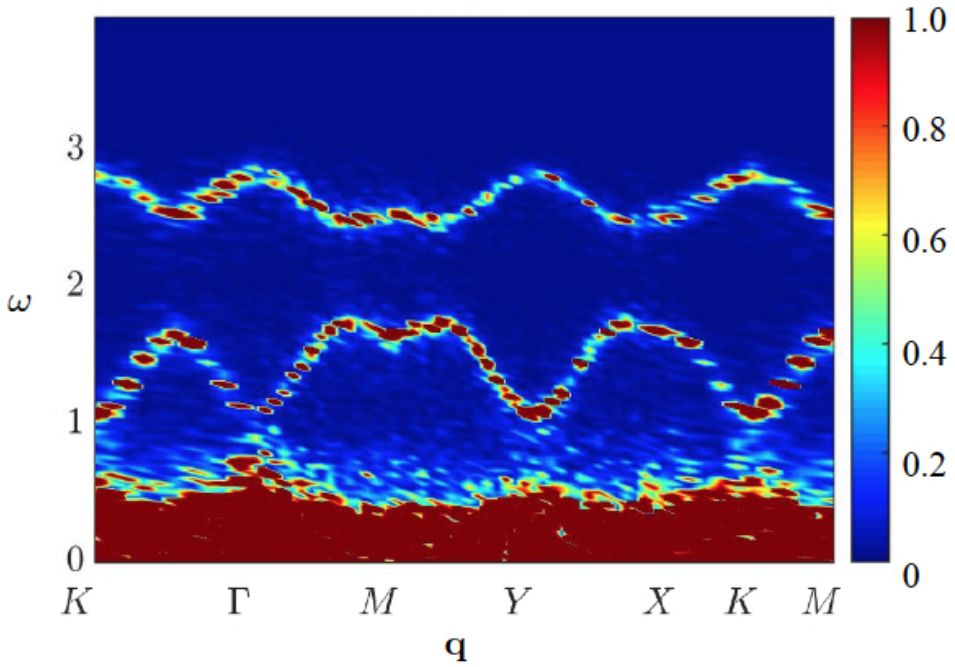

Figure 4.15: Dynamical structure factor at very low temperature $T = 10^{-4}$ of the $\sqrt{3} \times \sqrt{3}$ state with uniform $\eta_\alpha = +1$. This state is the ground state selected by quantum order by disorder in the case of ferromagnetic $\Gamma < 0$.

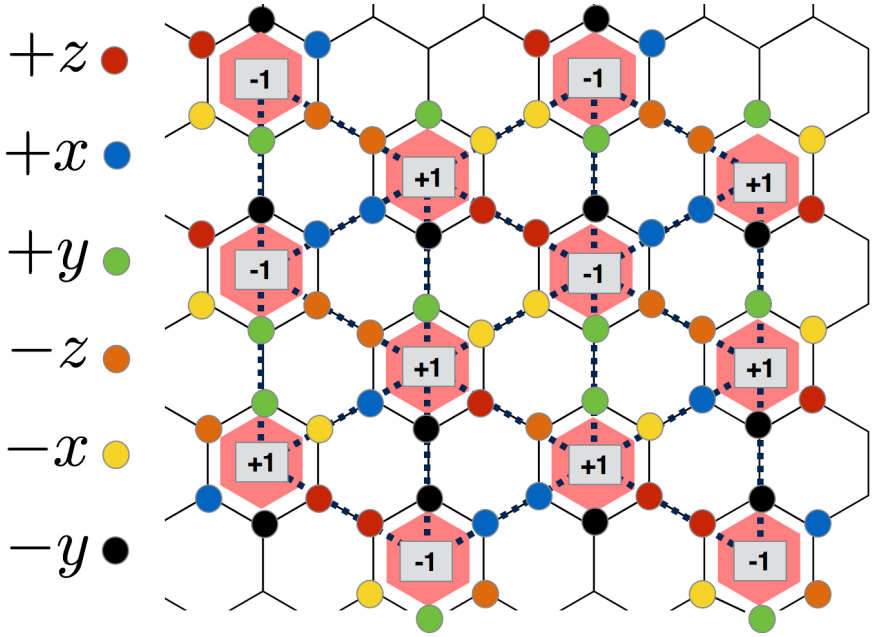

Figure 4.16: Spins have cubic symmetry at low temperature, the resulting non-zero flux parameter hexagons with $W \sim 1$ (shaded) form an Ising triangular lattice. For each triangle made of 3 such hexagons, the corresponding η's are frustrated i.e. $(++-)$ or $(--+)$.

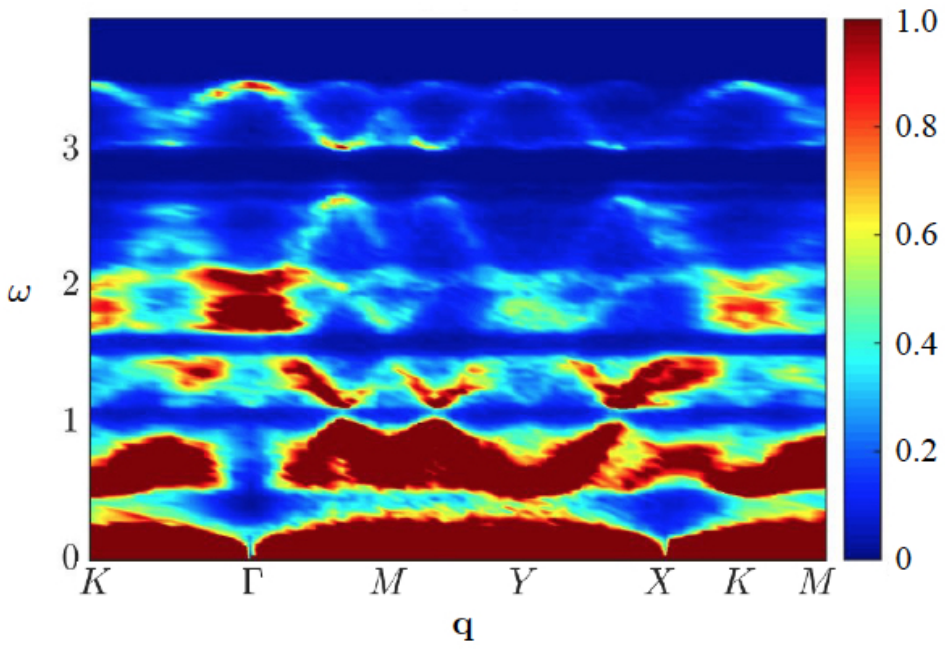

Figure 4.17: Dynamical structure factor of the Gamma model averaged over 100 different $\{\eta_\alpha\}$ configurations that are ground states of the AF Ising model Eq. (4.19); see also Fig. 4.16. Again, a small perturbation is introduced through Monte Carlo simulations at low temperature $T = 10^{-4}$.

to introduce small deviations to the ground state constructed from the η variables. Using this slightly perturbed state as the initial condition, we perform LL dynamics simulations to compute the dynamical structure factor. The resultant $\mathcal{S}(\mathbf{q}, \omega)$ shown in Fig. 4.17 is obtained by averaging over 100 different AFM $\{\eta_\alpha\}$ configurations. We see sharp band structure and band gap like features along the high symmetry line. In the ploted range of ω we can see clear discontinuity (band gap like features) close to $\omega = 1$, $\omega = 1.5$ and $\omega = 3$. These features appear relatively periodic along the high symmetry line at higher ω values close to $\omega \in (3, 3.5)$.

4.10 Gamma model in a magnetic field

I have worked with Zhongzheng Tian and Zhijie Fan to study the effect of introducing magnetic field along with the pure Γ-interaction term [84]. In this section I have highlighted some of the

prominent results from our work. The Hamiltonian is represented by the following equation,

$$\mathcal{H} \;=\; \Gamma \sum_{\gamma} \sum_{\langle ij \rangle \| \gamma} (S_i^{\alpha} S_j^{\beta} + S_i^{\beta} S_j^{\alpha}) - \mathbf{H} \sum_i \mathbf{S}_i. \tag{4.20}$$

where (α, β, γ) are permutations of (x, y, z) and the second term represents the Zeeman coupling to a magnetic field $\mathbf{H} = H\hat{\mathbf{n}}$ in the $\hat{\mathbf{n}} \parallel [111]$ direction.

Frustrated magnets are easily prone to excitations in magnetic field. We found that the presence of magnetic field in the high-symmetry direction lifts the macroscopic classical ground-state degeneracy of the honeycomb Γ model and induces a long-range magnetic order. For the ferromagnetic Γ-exchange we observed that a simple spin-polarized state with spins aligning with the field direction is selected by the external field. Interestingly this particular ferromagnetic state also happens to be one of the ground states of the zero-field Γ model [73]. On the other hand in case of antiferromagnetic interaction a periodic $\sqrt{3} \times \sqrt{3}$ magnetic order is selected by magnetic field. This tripled unit cell has an exotic spin structure that can be described by a magnetic moment vector and a hidden Néel order parameter, which is a spin-flop state of a bipartite antiferromagnet [84]. As a result, we can classify this as a spin-flop transition from plaquette-ordered spin liquid at low field to a field driven long-range magnetic order.

The Néel vector is accompanied with $\mathcal{O}(2)$ degeneracy originating from its rotation symmetry. Thermal or quantum fluctuations fractures this degeneracy into a six-fold degenerate ground state. At sufficiently high fields, the ground-state $\mathcal{Z}6$ symmetry breaking is attributed to two Berezinskii-Kosterlitz-Thouless transitions that enclose a critical $\mathbf{XY}$ phase. Figure 4.18 shows the schematic phase diagram of the classical Γ model in presence of a field H.

4.11 Numerical simulations

In this section I have discussed the details of the implementation of the lattice and numerical methods.

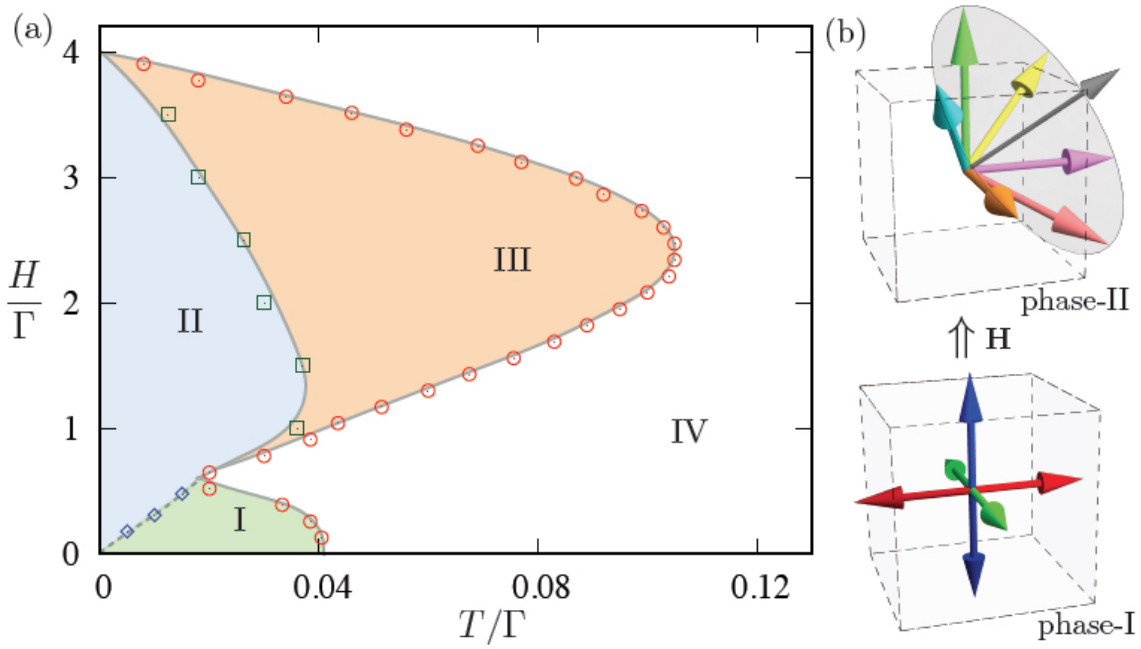

Figure 4.18: Schematic diagram of the Γ model.The different phases are color shaded as regimes change with temperature T and strength of the magnetic field H. (I) Spin liquid with hexagonal flux order that breaks the lattice translation symmetry [74]. (II) Long range $\sqrt{3} \times \sqrt{3}$ magnetic order with a tripled unit cell. (III) Critical $\mathbf{XY}$ phase with an emergent $\mathcal{O}(2)$ symmetry of Néel vectors. (IV) Classical spin liquid with short ranged correlation that is smoothly connected to high-T paramagnet and the polarized state at high field. (b) The transition from the plaquette spin liquid to the $\sqrt{3} \times \sqrt{3}$ magnetic order resembles a spin flop transition in bipartite antiferromagnet with weak anisotropy.Figure reproduced from [84]

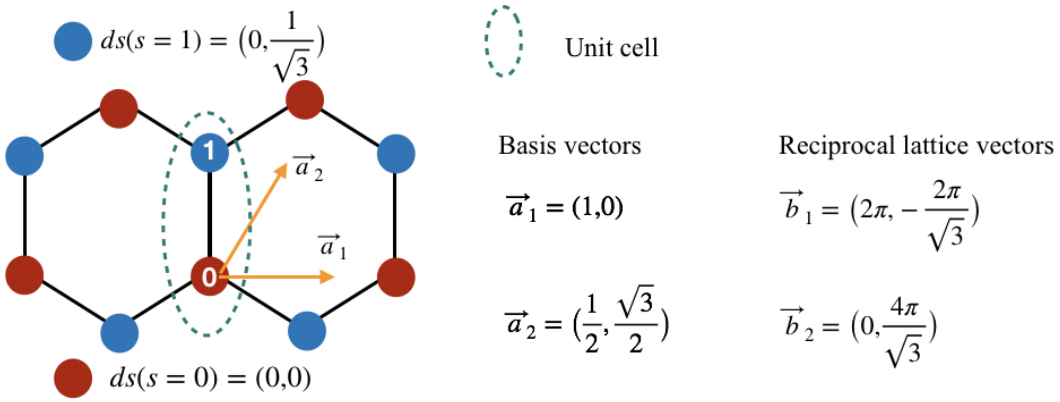

Figure 4.19: Honeycomb lattice : basis vectors and the corresponding reciprocal lattice vectors.

Table 4.1: Nearest neighbor coordinates

$s \downarrow$ $nn \rightarrow$	1	2	3
0	(X, Y, s=1)	(X, Y+1, s=1)	(X-1, Y+1, s=1)
1	(X, Y, s=0)	(X+1, Y-1, s=0)	(X, Y-1, s=0)

4.11.1 Lattice structure

We study the Gamma interaction on a honeycomb lattice. The basis vectors and corresponding reciprocal lattice vectors are given in Figure 4.19. The unit cell consists of 2 spin sites, each of which is considered a sublattice. This makes the total number of spins on a honeycomb lattice of linear size L equal to $N_S = 2L^2$. The coordinates of the unit cell is represented by (X, Y). Each of the spins on a lattice are represented by position vectors $\mathbf{r} = X\mathbf{a}_1 + Y\mathbf{a}_2 + ds[s]$, where $\mathbf{ds}(s)$ given in Figure 4.19 represents the position vector of each of the two sublattice spins within each unit cell.

Each spin on the unit cell has 3 nearest neighbors. We set the closest nearest neighbors individually for each sublattice. The nearest neighbors are constructed as given below and the idea is illustrated in the Figure 4.20. The coordinate construction for the nearest neighbour spins for the honeycomb lattice are shown in Table 4.1, where (X, Y) coordinate denotes the unit cell and s denotes the sublattices. We consider only these neighbors for exchange interactions for both Monte Carlo statistics and spin dynamics effective field.

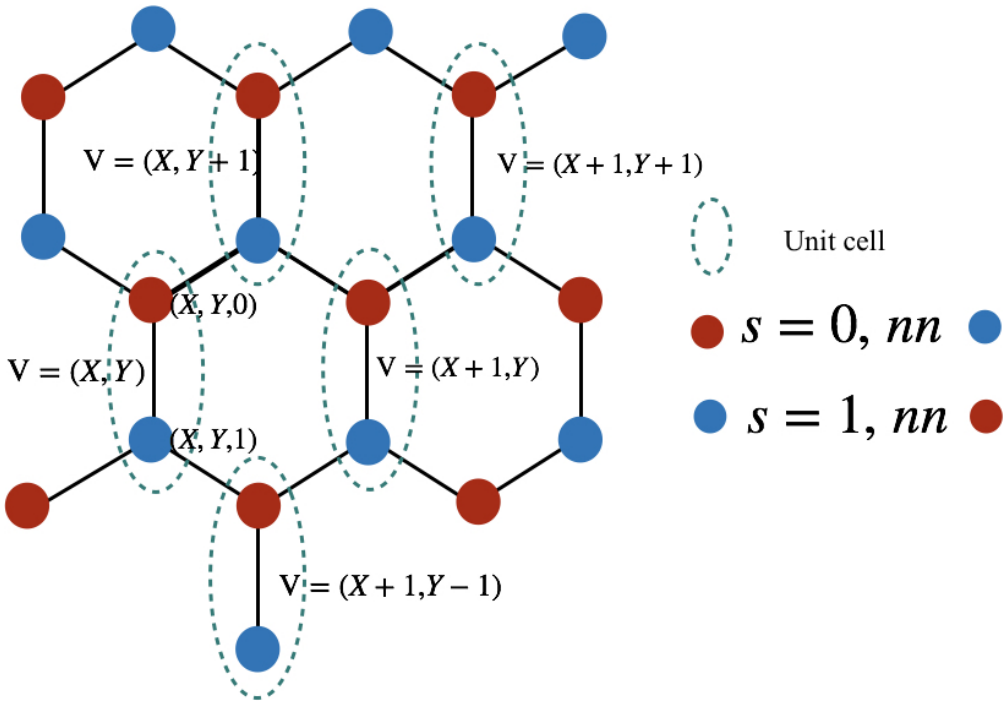

Figure 4.20: Nearest neighbors coordinates for each of the sublattices on a Honeycomb lattice.

4.11.2 Spin dynamics equations

The three dimensional Heisenberg spins experience Γ off-diagonal exchange interaction amongst themselves as given in Eq. 4.1 and their time trajectories are given by the Landau Lifshitz equation as given in Eq. 4.15. In this work we use the Mentink et al. SIB method [31] to integrate the Landau Lifshitz equation and simulate the spin trajectory in time. In our system the the dynamics in energy conserving and follow the method explained in section 3.2.2. The Γ interaction Hamiltonian in the component form as given Eq. 4.1 leads to the following effective Hamiltonian.

$$\begin{aligned}\mathcal{H}_{eff,i} &= -\frac{\partial \mathcal{H}}{\partial \mathbf{S}_i} = -\left(\frac{\partial \mathcal{H}}{\mathbf{S}_{ix}}, \frac{\partial \mathcal{H}}{\mathbf{S}_{iy}}, \frac{\partial \mathcal{H}}{\mathbf{S}_{iz}}\right) \\ &= -\Gamma\Big((\mathbf{S}^z_{j\in y-bond} + \mathbf{S}^y_{j\in z-bond})\hat{\mathbf{x}} \\ &\qquad + (\mathbf{S}^x_{j\in z-bond} + \mathbf{S}^z_{j\in x-bond})\hat{\mathbf{y}} + (\mathbf{S}^y_{j\in x-bond} + \mathbf{S}^x_{j\in y-bond})\hat{\mathbf{z}}\Big)\end{aligned} \tag{4.21}$$

Once we have the spin trajectories in time, we can use them to compute all kinds of dynamical structure factor plots, for example Fig. 4.12 and 4.14 given by Eq.4.17 for the spins and Eq. 4.18 for the flux variables. These dynamical structure factor figures are plot along the high symmetry points in the Brillouin zone(BZ). The BZ of a hexagonal lattice is also a hexagonal lattice. Details of these simulations are given at the end of Section 5.7.3.

4.12 Discussion and Outlook

We have demonstrated that thermal order-by-disorder in honeycomb Γ-model drives a phase transition into a new spin liquid phase with a hidden flux long-range order. The same scenario also applies to quantum order-by-disorder which generates a similar effective cubic anisotropy [73]. In the presence of other perturbations, the degeneracy of the plaquette-ordered states is lifted. Specifically, the antiferro-Kitaev exchange preserves the continuous degeneracy of $\hat{\mathbf{n}} = (a, b, c)$, while lifting the discrete η degeneracy by selecting the uniform configuration. Interestingly. the discrete degeneracy remains in the case of ferromagnetic Kitaev exchange. On the other hand, Heisenberg interactions favors a ground state with $\hat{\mathbf{n}} = (1, 1, 1)$. However, the flux-ordered spin liquid is expected to survive in a finite temperature window when these perturbations are small compared with the dominant Γ term. Experimentally, one manifestation of plaquette ordering is the onset of spin cubic anisotropy. However, this signal might be difficult to detect given the intrinsic cubic symmetry of the system. Through coupling to other degrees of freedom in crystal, e.g. spin-lattice coupling, the translation-symmetry breaking could produce Bragg peaks in neutron or X-ray scattering.

The effects of quantum fluctuations have been extensively discussed in Ref. [73]. The relevant energy scale of quantum order-by-disorder is $T^* \sim \mathcal{O}(|\Gamma|S)$ for both the discrete η and continuous $\hat{\mathbf{n}}$ variables [73]. As noted in the same study, the induced effective interaction between η_α remains frustrated for antiferromagnetic Γ, so a similar flux-ordered spin liquid can be stabilized by pure quantum fluctuations in this case. It is, however, unclear what is the scenario in the ferromagnetic Γ model due to the closeness of the two energy scales. Restoring the spin length, the critical

temperature for thermal order-by-disorder is $T_c \sim 0.04|\Gamma|S^2$. Our finding thus ensures the existence of the exotic flux-ordered spin liquid for large S at the temperature window $T^* \lesssim T \lesssim T_c$. Finally, it is also of great interest to study similar flux-ordering in three-dimensional hyper- or stripy-honeycomb lattices where some of the flux variables are defined on extended strings.

CHAPTER 5

SPIN DYNAMICS OF THE ANTIFERROMAGNETIC HEISENBERG MODEL ON A KAGOME BILAYER

5.1 Results summary

- In this work we present spin dynamical simulations of classical Heisenberg antiferromagnet with nearest neighbor interactions on a quasi-two-dimensional kagome bilayer. This geometrically frustrated lattice consists of two kagome layers connected by a triangular-lattice linking layer.
- By combining Monte Carlo with precessional spin dynamics simulations, we compute the dynamical structure factor of the classical spin liquid in kagome bilayer and investigate the thermal and dilution effects. While the low frequency and long wavelength dynamics of the cooperative paramagnetic phase is dominated by spin diffusion, weak magnon excitations persist at higher energies, giving rise the half moon pattern in the dynamical structure factor.
- We also investigate the system in its site diluted form. The dynamical properties in the presence of spin vacancies can be understood within the two population picture. The spin diffusion of the “correlated" spin clusters is mainly driven by the zero-energy weather-van modes, giving rise to an autocorrelation function that decays exponentially with time.
- Vacancies gives rise to a unique arrangement of spins called orphan spins. The diffusive dynamics of the quasi-free “orphan" spins leads to a distinctive longer time power-law tail in the autocorrelation function. We discuss the implications of our work for the glassy behaviors observed in the archetypal frustrated magnet $SrCr_{9p}Ga_{12-9p}O_{19}$ (SCGO).

5.2 Introduction

The SCGO is one of the most intensely studied frustrated magnets [85–98]. Thermodynamically, SCGO does not exhibit any signs of magnetic ordering down to temperatures $T_g = 3.5$–7 K, depending weakly on the vacancy concentration $x = 1 - p$. Below T_g, the magnet enters an unconventional spin-glass phase. A cooperative paramagnetic regime, also known as a classical spin liquid, emerges at temperatures below the Curie-Weiss constant $\Theta_{\rm CW} \approx 500$ K. Geometrically, SCGO belongs to a class of frustrated Heisenberg antiferromagnets on the so-called bi-simplex lattices [17, 18, 99, 100]. These are networks of corner-sharing simplexes such as triangles and tetrahedra. Canonical examples include the pyrochlore [17, 18] and kagome [22, 26, 38, 101] antiferromagnets. In SCGO, the Cr^{3+} ions with spin $S = 3/2$ reside on a two-dimensional lattice consisting of corner-sharing tetrahedra and triangles, known as the kagome bilayer or pyrochlore slab, as shown in Fig. 5.1. The strong short-range spin correlations in the low-temperature liquid phase result from the constraints of zero total spin in every simplex, a condition that minimizes the nearest-neighbor exchange interactions on such unit.

Considerable experimental efforts have been devoted to understanding the unusual spin glass phase in SCGO [86–89, 92, 94–96, 98]. Despite the characteristic field-cooled and zero-field-cooled hysteresis in the bulk susceptibility, several dynamical properties of its glassy phase are distinctly different from those of conventional spin glasses. These include the quadratic T^2 behavior of the specific heat [86, 87], the linear ω-dependent dynamical susceptibility χ'' [92], and a significantly weaker memory effect [102]. Taken together, these features suggest that SCGO belongs to a new state of glassy magnets, dubbed the spin jam [98, 102], that include several other magnetic compounds [103, 104]. The source of this unusual dynamical phase in SCGO, however, remains to be clarified. One plausible scenario is that quantum fluctuations transform the macroscopic degeneracy associated with the classical spin liquid of the kagome bilayer into the rugged energy landscape of spin jam [98, 105]. It remains to be shown how the unusual glassy behaviors of the spin jam evolve from the spin dynamics of the cooperative paramagnet.

Toward this goal, we present in this work the first systematic study of the dynamical properties of the bilayer-kagome classical spin liquid. By combining Monte Carlo simulations with energy-conserving Landau-Lifshitz dynamics, we compute the dynamical structure factor of the liquid regime. At the energy scales of the exchange interaction, we find signals of spin-wave excitations in the form of half moon pattern, replacing the pinch-point singularity of the static structure factor. On the other hand, the low-energy dynamics is dominated by spin-diffusion driven mostly by the zero-energy modes. The diffusion constant is found to depend weakly on temperature, but decrease significantly with increasing vacancy densities.

Our results will also serve as an important benchmark against which dynamical behaviors induced by other perturbations can be compared. Of particular interest are those perturbations, such as quantum order-by-disorder, that give rise to glassy dynamics characteristic of either the conventional spin-glass or the exotic spin-jam states. It is also worth noting that the dynamical properties of classical spin liquid has been extensively studied for Heisenberg antiferromagnets on both pyrochlore [17, 18, 106] and kagome lattices [80, 107–109]. Another aim of this work is to compare the spin dynamics of bilayer kagome against these two well studied bi-simplex frustrated magnets. The rest of the work is organized as follows. In section 5.3, we discuss the ground-state manifold of Heisenberg antiferromagnet on the kagome bilayer. We also outline the numerical framework that combines Monte Carlo simulation with energy-preserving Landau-Lifshitz dynamics method for computing the dynamical structure factor of a classical spin liquid. Magnetic excitations revealed from the dynamical structure factor are discussed in Sec. 5.4. In particular, half-moon features, which are the dynamical manifestation of the famous pinch-point structure at finite energies, are highlighted. Systematic analysis of the low-energy spin dynamics, which is dominated by diffusive modes, is presented in Sec. 5.5. We present in Sec. 5.6 dynamical features due to quenched disorder introduced by vacancies. Of particular interest is the emergence of quasi-free orphan spins that interact with each other through a week effective interaction mediated by the background spin-liquid. We have discussed the set up of the kagome-bilayer lattice for the implementation of the numerical methods in Sec. 5.7. We conclude in Sec. 5.8 with a brief summary and outlook on

future work.Our results are published in [110].

5.3 Model and method

We consider the classical Heisenberg model with nearest neighbor interactions on the kagome bilayer

$$\mathcal{H} \;=\; J\sum_{\langle ij\rangle}\mathbf{S}_i\cdot\mathbf{S}_j \tag{5.1}$$

Here $J>0$ is the antiferromagnetic exchange, $\langle ij\rangle$ denotes nearest-neighbor pairs, and the classical spins $\mathbf{S}_i$ are unit vectors. The kagome bilayer has a Bravais triangular lattice with a unit cell consisting of two corner sharing tetrahedra of opposite orientation. The bases of the tetrahedra in the two kagome layers are connected by triangle units; see Fig. 5.1. The triangle and tetrahedron are the regular simplexes with $q=3$ and $q=4$ corners, respectively. Importantly, because of this corner-sharing simplex structure, the exchange interaction can also be expressed as a sum of the squared total spin of both types of simplexes

$$\mathcal{H}=\frac{J}{2}\sum_{\boxtimes}\mathbf{L}_{\boxtimes}^2+\sum_{\triangle}\mathbf{L}_{\triangle}^2+\text{const.} \tag{5.2}$$

Here $\mathbf{L}_{\boxtimes}=\sum_{i\in\boxtimes}\mathbf{S}_i$ denotes total spin in a tetrahedron, $\mathbf{L}_{\triangle}=\sum_{i\in\triangle}\mathbf{S}_i$ denotes total spins of a triangle, and $\sum_{\boxtimes}$ and $\sum_{\triangle}$ indicate summation over tetrahedra and triangles, respectively, in the kagome-bilayer lattice. One can immediately see that the exchange energy is minimized by the condition that total spin of every simplexes is zero:

$$\mathbf{L}_{\boxtimes}=\mathbf{L}_{\triangle}=0, \tag{5.3}$$

The ground-state condition is confirmed by our Monte Carlo simulations. The fact that a macroscopic number of spin configurations satisfy the minimum energy condition leads to a classical spin liquid regime at temperatures $T\lesssim J$. Indeed, our Monte Carlo simulations show no signs of phase

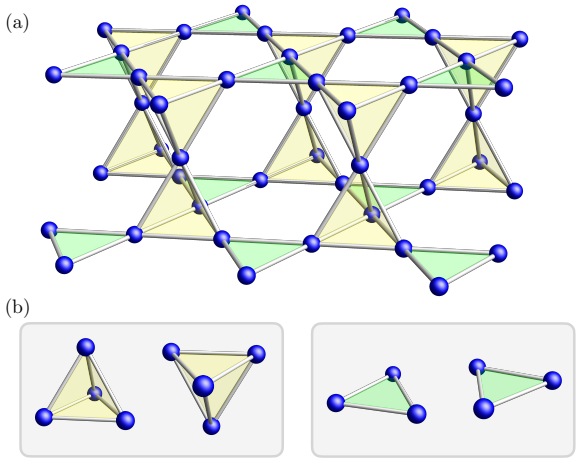

Figure 5.1: Top: Lattice structure of kagome bilayer. It can be viewed as a quasi-two-dimensional network of corner-sharing simplexes. There are two kinds of simplexes: tetrahedron and triangles, both comes with two (opposite) orientations, as shown in the bottom panel. Spins in the ground states satisfy the constraint that total spin in both types of simplexes is zero: $\mathbf{L}_{\boxtimes} = \mathbf{L}_{\triangle} = 0$.

transition down to temperatures $T \approx 0.001J$, consistent with previous studies [111–114]. Instead, a spin-disordered phase with strong short-range correlation is obtained at low temperatures.

In general, there are two types of spin dynamics in the liquid regime. At short time scales, or high frequencies ($\omega \sim J$), there are spin-wave excitations corresponding to small amplitude deviations from the ground-state manifold. These excitations are similar to the magnons in unfrustrated magnets. On the other hand, the macroscopic number of zero modes, or the weather-vane modes, that connect different ground states dominate the long-time dynamical behaviors of the frustrated bi-simplex antiferromagnet. The resultant drifting of the system in the ground-state manifold gives rise to spin-diffusion behaviors and an exponential decaying spin autocorrelation. In the following, we discuss our simulation results within this general picture.

The equation of motion for classical spins is given by the Landau-Lifshitz equation

$$\frac{d\mathbf{S}_i}{dt} = -\mathbf{S}_i \times \frac{\partial \mathcal{H}}{\partial \mathbf{S}_i} = -J \sum_j{}' \mathbf{S}_i \times \mathbf{S}_j, \tag{5.4}$$

where the prime indicates summation is restricted to the nearest neighbors of the i-th spin. Here

we numerically integrate the Landau-Lifshitz equation to compute the dynamical structure factor of the classical spin liquid. Low temperature Monte Carlo simulations are first used to obtain spin configurations in equilibrium of a specified temperature. These are then used as the initial states for the energy-conserving precession dynamics simulations. An efficient semi-implicit integration algorithm [31] is employed to integrate the above Landau-Lifshitz equation. The high efficiency of the algorithm comes from fact that it preserves the spin length at every time step and the energy values are well conserved with time irrespective of the step size or the time span of the simulation. From the numerically obtained spin trajectories $\mathbf{S}_i(t)$, we compute the dynamical correlation function $\mathcal{S}(\mathbf{q}, t)$

$$\mathcal{S}(\mathbf{q}, t) = \langle \mathbf{S}_{\mathbf{q}}(t) \cdot \mathbf{S}^*_{\mathbf{q}}(0) \rangle, \tag{5.5}$$

where $\mathbf{S}_{\mathbf{q}}(t) \equiv \sum_i \mathbf{S}_i(t) \exp(i\mathbf{q} \cdot \mathbf{r}_i)/\sqrt{N}$ is the spatial Fourier transform of the instantaneous spin configuration, and $\langle \cdots \rangle$ denotes the ensemble average over independent initial states of a given temperature. The dynamical structure factor is then given by

$$\begin{aligned} \mathcal{S}(\mathbf{q}, \omega) &= \int \mathcal{S}(\mathbf{q}, t) e^{-i\omega t} dt \\ &= \frac{1}{N} \sum_{ij} \int dt \langle \mathbf{S}_i(t) \cdot \mathbf{S}_j(0) \rangle e^{-i\omega t} dt, \end{aligned} \tag{5.6}$$

which is essentially the space-time Fourier transform of the spin-spin correlator $C_{ij}(t) \equiv \langle \mathbf{S}_i(t) \cdot \mathbf{S}_j(0) \rangle$.

5.4 Magnons and half moon patterns

The intensity plot of the scaled dynamical structure factor $\beta\, \mathcal{S}(\mathbf{q}, \omega)$, where $\beta = 1/T$, is shown in Fig. 5.2 for four different temperatures. The spin excitations are clearly dominated by the low-

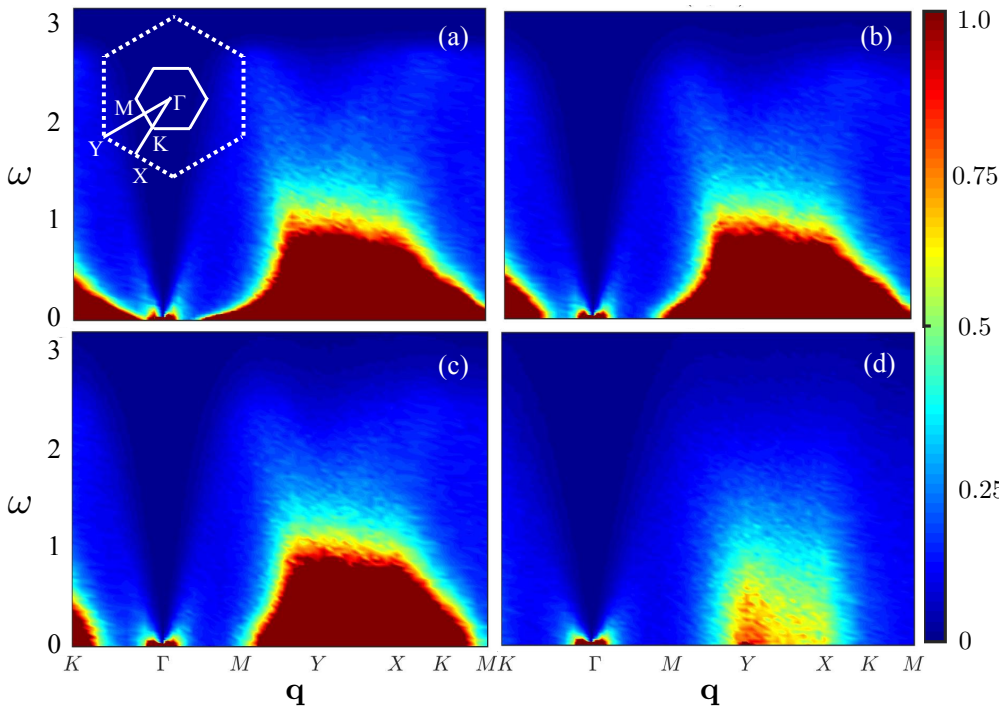

Figure 5.2: Temperature-scaled dynamical structure factor $\beta\,\mathcal{S}(\mathbf{q},\omega)$ of the classical spin liquid in the bilayer kagome antiferromagnet at four different temperatures: (a) $T/J = 0.01$, (b) 0.05, (c) 0.1, and (d) 0.6; here $\beta = 1/T$. The linear size of the simulated lattice is $L = 30$, with number of spins $N = 7 \times L^2$.

energy quasi-static fluctuations that extend over most of the Brillouin zone; also see Fig. 5.3 for the density plots of $\mathcal{S}(\mathbf{q},\omega)$ in the reciprocal space at constant energies. At low temperatures, the similar patterns of the quasi-static excitations indicating nontrivial scaling behaviors to be discussed below. Moreover, the relatively weak excitations at higher energies $\omega \gtrsim J$ result from the magnon fluctuations in the vicinity of an instantaneous ground state. Contrary to the kagome antiferromagnets [80, 108], no sharp propagating modes can be seen in the dynamical structure factor of the bilayer kagome.

The static structure factor, corresponding to Fig. 5.3(a) with $\omega = 0$, exhibits sharp pinch points which are a hallmark of highly correlated spin liquid in bi-simplex frustrated magnets. The source of these singularities can be attributed to the ground-state constraints Eq. (5.3), which translates into a solenoid condition $\nabla\cdot\mathbf{B} = 0$ for an emergent "magnetic" or flux field that is a coarse-grained representation of the spin configuration. This in turn gives rise to an anisotropic dipolar-like correlation of the flux field, which manifests itself as the pinch-point singularity in the reciprocal space [22–24].

At finite temperatures, the width of the pinch-point is roughly proportional to $\sqrt{T}$ [115]. Interestingly, the pinch point is also smeared with increasing ω, and is replaced by the so-called half moon pattern at $\omega \gtrsim J$, as shown in Fig. 5.3 (b) and (c). Similar features, called the "excitation rings" have been observed in the finite-energy dynamical structure factor of the coplanar spin liquid phase of kagome [108]. It has been pointed out that the half-moon can be viewed as the pinch-point with a dispersive dynamical flux field [116]. These crescent patterns at high energies are the remnants of the propagating magnons mentioned above. Compared with the coplanar phase in kagome, the half-moon feature is much weaker in the liquid phase of bilayer kagome, indicating less rigid local structures in the instantaneous ground state.

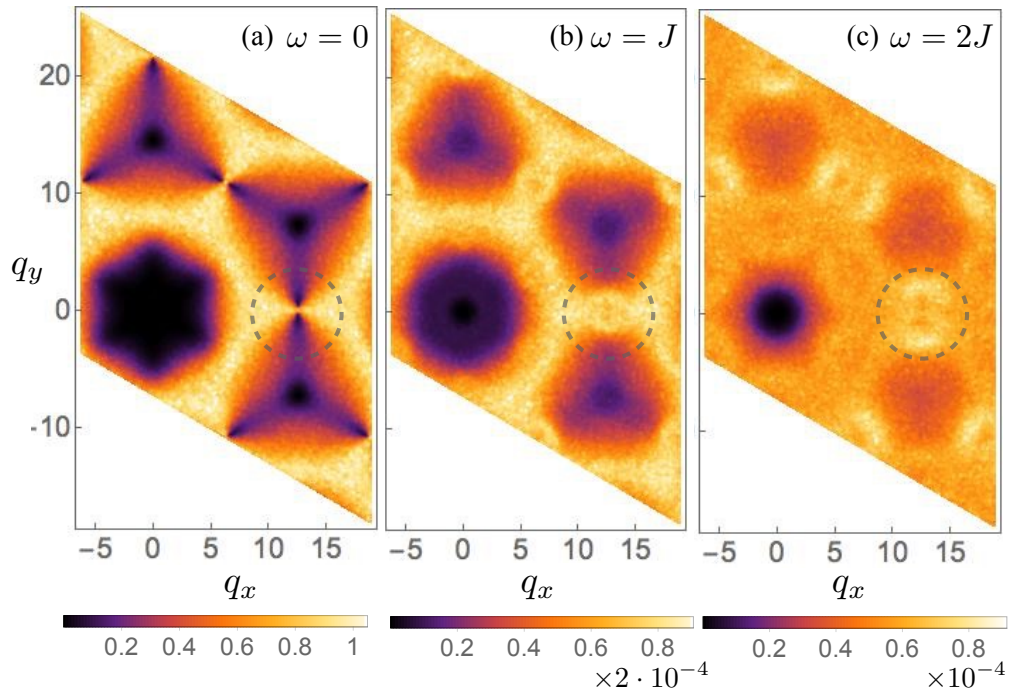

Figure 5.3: Density plots of the dynamical structure factor $\mathcal{S}(\mathbf{q}, \omega)$ at $T = 0.005\,J$ in the reciprocal space: (a) $\omega = 0$, (b) $\omega = J$, and (c) $2J$. The system size is $L = 30$. The dashed circles indicate the pinch point at $\omega = 0$, and the half moon pattern at higher energies.

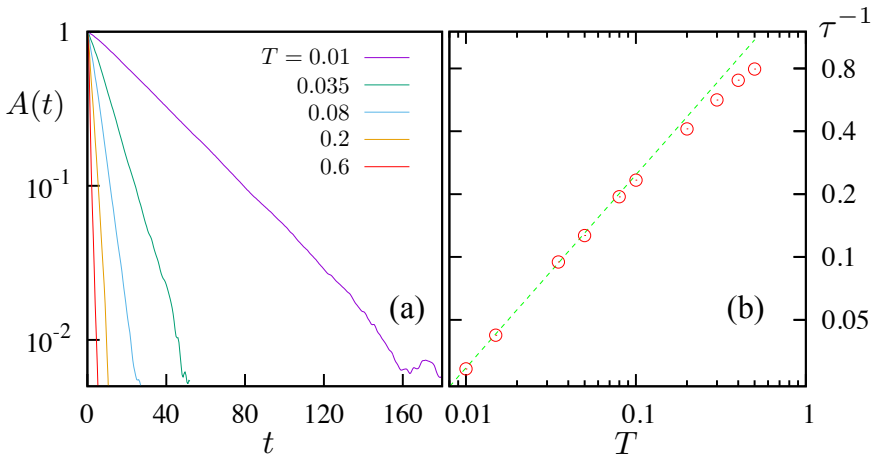

Figure 5.4: (a) The ensemble averaged spin autocorrelation function $A(t) = \sum_i \langle \mathbf{S}_i(t) \cdot \mathbf{S}_i(0) \rangle / N$ on a $L = 30$ lattice for varying temperatures. (b) Extracted relaxation time τ of $A(t) = \exp(-t/\tau)$ as a function of temperature. The dashed line shows the power-law $\tau \sim T^{-0.924}$ dependence.

5.5 Spin diffusion

The relatively weak half moon excitations also indicate a dominating spin diffusive dynamics in bilayer kagome. In general, spin diffusion dominates the excitation spectrum of disordered Heisenberg systems in the hydrodynamic limit [117, 118]. In frustrated magnets, this diffusion results from the macroscopic number of zero-energy modes in the instantaneous ground state, causing the system to wander around the degenerate manifold. One particular manifestation of this diffusion is the decay of the spin autocorrelation function

$$A(t) = \frac{1}{N}\sum_i \langle \mathbf{S}_i(t)\cdot\mathbf{S}_i(0)\rangle = \sum_{\mathbf{q}} \mathcal{S}(\mathbf{q},t), \tag{5.7}$$

where again $\langle\cdots\rangle$ is the thermal average, which is achieved through averaging over independent initial states from Monte Carlo simulations. Fig. 5.4(a) shows $A(t)$ as a function of time for various temperatures obtained from a $L = 30$ system. The decay of the autocorrelation function is found to be exponential $A(t) \sim \exp(-t/\tau)$ in the low temperature regime, and the numerically extracted time constant τ is shown in Fig. 5.4(b) as a function of temperature.

The nearly linear segment in the log-log plot suggests a power-law dependence $\tau \sim T^{-\zeta}$, where the numerically obtained exponent $\zeta = 0.924 \pm 0.015$, which is close to 1 as predicted by a soft-spin Langevin dynamics model for frustrated magnets with macroscopic ground-state degeneracy [106]. The exponential decay with $\tau \sim 1/T$ is consistent with the zero-mode driven spin-diffusion scenario [17, 106], since the zero modes have no intrinsic energy scales, and the only relevant one is set by the inverse temperature. This result is also in stark contrast to the high-T conventional paramagnet in which the spin-diffusion is shown to produce a power-law tail in the autocorrelation function [118–122].

While the microscopic mechanisms of spin-diffusion could be thermal or quantum fluctuations, or the large number of zero modes in frustrated systems, fundamentally the diffusive spin dynamics is related to the fact that the total spin density $\mathbf{m} = \sum_i \mathbf{S}_i/N$ is a constant of the equation of motion.

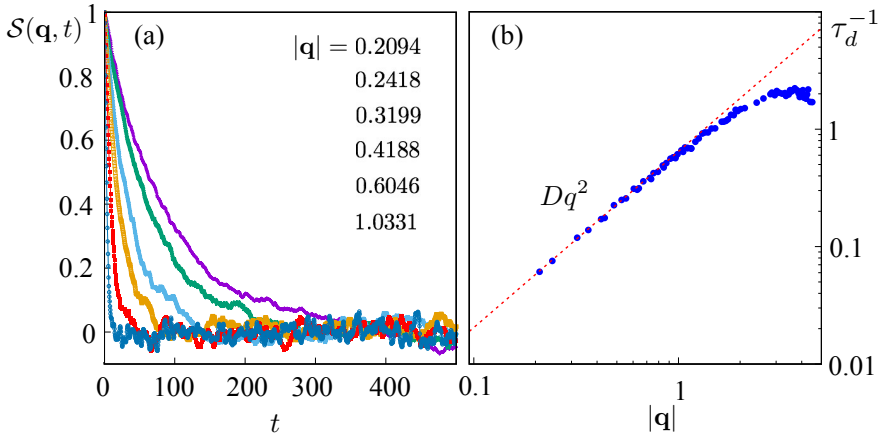

Figure 5.5: (a) Time dependence of the normalized dynamical correlation function $\mathcal{S}(\mathbf{q},t)/\mathcal{S}(\mathbf{q},0)$ at $T = 0.5J$ for various wave vectors close to the zone center. The simulated system size is $L = 60$. (b) The inverse relaxation time τ_d^{-1} extracted from panel (a) as a function of $|\mathbf{q}|$. For each wave vector the data is fitted to an exponentially decaying function.

By combining the continuity equation $\partial\mathbf{m}/\partial t + \nabla \cdot \mathbf{j} = 0$ with a phenomenological Fick's law for local spin current $\mathbf{j} = -D\nabla\mathbf{m}$, one arrives at the familiar diffusion equation for the magnetization density. In the hydrodynamic regime, this introduces a diffusion timescale $\tau_d = 1/Dq^2$ for perturbations characterized by wave vector $\mathbf{q}$. This is indeed confirmed by our dynamical simulations. Fig. 5.5(a) shows the time dependence of the dynamical correlation function $\mathcal{S}(\mathbf{q},t)$ for various wave vectors. Each curve is obtained after averaging over 500 independent initial states from Monte Carlo simulations. The correlation function is found to decay exponentially with time: $\mathcal{S}(\mathbf{q},t) \sim \exp(-t/\tau_d)$, where the numerically extracted relaxation time, shown in Fig. 5.5(b), is isotropic in the reciprocal space and follows nicely the expected behavior $\tau_d^{-1} = Dq^2$ for wave vectors close to the Brillouin zone center.

More generally, here we try to understand our results using the hydrodynamic theory of the paramagnetic state, which suggests a generalized dynamical susceptibility: $\chi(\mathbf{q},\omega) = -\chi(\mathbf{q})\, Dq^2/(Dq^2 - i\omega)$ [117, 123], where $\chi(\mathbf{q})$ is the static susceptibility at wave vector $\mathbf{q}$ and D is the spin diffusion coefficient. The dynamical structural factor is obtained through the fluctuation-dissipation theorem: $\mathcal{S}(\mathbf{q},\omega) \approx 2[n_B(\omega)+1]\,\mathrm{Im}\chi(\mathbf{q},\omega)$, where $n_B(\omega) = 1/(e^{\beta\omega}-1)$. In the $\omega \ll T$ regime, assuming $\chi(\mathbf{q}) \approx \chi$ is a constant for small q, the dynamical structure factor can be expressed in a

scaling form

$$\beta q^2 \mathcal{S}(\mathbf{q},\omega) = \chi \frac{2D}{(\omega/q^2)^2 + D^2}, \tag{5.8}$$

A similar result can be obtained from the Langevin soft-spin model [106]. By plotting $\beta q^2 \mathcal{S}$ versus ω/q^2, we find nice data collapsing from curves of different wave vectors, as shown in Fig. 5.6 (a) and (b), indicating a static susceptibility that indeed weakly depends on $\mathbf{q}$ for wave vectors close to zone center. On the other hand, we find that the collapsing of data points from different temperatures is not very satisfactory. Instead, we fit the collapsed data points from each temperature with the Lorentzian scaling function in Eq. (5.8) and extract both the spin diffusion coefficient D and static susceptibility χ. The temperature dependence of these two quantities are shown in Fig. 5.6(c) and (d). The spin-diffusion coefficient decreases quite appreciably with temperature, while the susceptibility remains roughly the same within the error bars.

5.6 Dilution effects

We next investigate the effect of dilution on the spin dynamics of the liquid phase. Previous studies have indicated that dilution with non-magnetic vacancies does not induce the spin-glass behavior of SCGO [99, 124]. In fact, the condition Eq. (5.3) is satisfied for every simplex, for both tetrahedron and trinagle, in the ground states even for strong dilution [99]. Consequently, a macroscopic degeneracy remains and the low-T phase seems well approximated by a Coulombic classical spin liquid. To demonstrate this, we compute the dynamical structure factor of the diluted kagome bilayer using a combination of Monte Carlo simulations with the energy-conserving Landau-Lifshitz dynamics simulations. Fig. 5.7 shows the computed $\mathcal{S}(\mathbf{q},\omega)$ at $T = 0.01J$ for four different vacancy concentrations. In addition to the thermal average over independent initial states, the $\mathcal{S}(\mathbf{q},\omega)$ of the diluted system is computed with a further average over the disorder, or different vacancy configurations. Interestingly, we find no dramatic change to the calculated $\mathcal{S}(\mathbf{q},\omega)$ even for vacancy density as high as $x = 0.5$. The quasi-static excitations show similar patterns for all concentrations, although both the energy of spin-wave-like excitations at large ω and the bandwidth of the

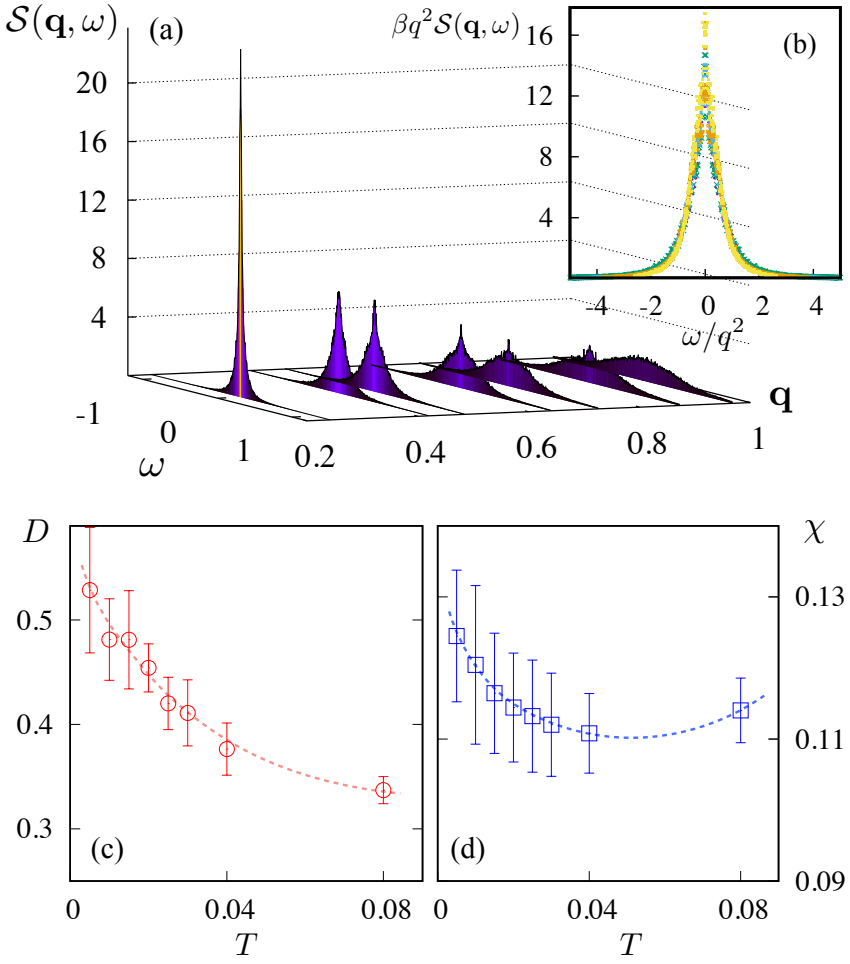

Figure 5.6: (a) Dynamical structure factor $\mathcal{S}(\mathbf{q},\omega)$ as a function of ω at varying wave vectors $\mathbf{q}$ at a temperature $T = 0.01J$. (b) Scaling collapse according to Eq. (5.8) for data points from different wave vectors shown in panel (a). These curves are well approximated by a Lorentzian centered on $\omega = 0$. By fitting the collapsed data-points to the scaling function, the numerically extracted spin diffusion coefficient D and static susceptibility χ (normalized to the value at $T = 0.01$) are shown in panels (c) and (d), respectively, as functions of temperature.

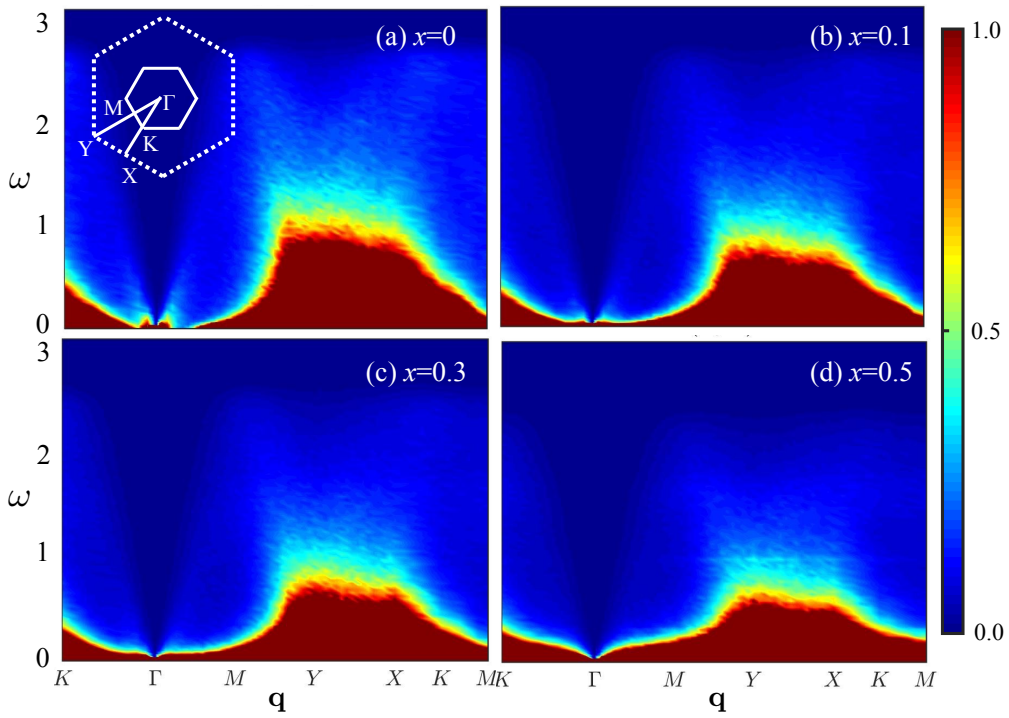

Figure 5.7: Dynamical structure factor $\mathcal{S}(\mathbf{q}, \omega)$ of the classical spin liquid in the diluted bilayer kagome antiferromagnet at $T = 0.01$ for four different vacancy concentrations: (a) $x = 0$ (no dilution), (b) 0.1, (c) 0.3, and (d) 0.5. The linear size of the simulated lattice is $L = 30$. The density plots for diluted systems ($x \neq 0$) are further averaged over 50 different disorder configurations.

quasi-static excitations are slightly reduced with increasing vacancy concentrations.

Focusing on the small-ω and $\mathbf{q}$ regime, we found that the dynamical structure factor is still well approximated by the scaling function of Eq. (5.8), as shown in Fig. 5.8(a) and (b), indicating a dominating spin diffusion behavior. The diffusion coefficient D extracted from the data-point collapsing is plotted in Fig. 5.8(c) as a function of x. The reduced diffusivity with increasing vacancy concentration indicates a longer relaxation time $\tau_d = 1/Dq^2$, or a slower dynamics, caused by the disorder, although the system remains liquid-like. Fig. 5.8(d) shows the extracted static susceptibility χ in the $q \to 0$ limit versus vacancy concentration x. This trend is consistent with the two population picture since the quasi-free orphan spins dominate the low-T static susceptibility, hence χ increases with the vacancy concentration.

Since the presence of vacancies does not change the liquid nature or the frustrated spin-interactions in the kagome bilayer, it is unclear whether the non-magnetic impurities introduce any new dynamical effect. On the other hand, the so-called orphan spins due to the dilution are known to induce nontrivial effects on the equilibrium properties of the kagome bilayer [125]. The orphan spin corresponds to defect triangular simplex with only one surviving spin and two non-magnetic sites [99, 126]. An example of the orphan spin is shown in Fig. 5.9. One can also think of orphan spin as connecting a $q = 3$ triangular simplex and a $q = 1$ point simplex, which is the spin itself. The orphan spin behaves as a quasi-free spin with a fractionalized length $S/2$ when perturbed by a magnetic field [113, 114]. Experimentally, these seemingly isolated free spins in diluted SCGO produce a Curie-like component in the static susceptibility even at temperatures well below Θ_{CW} [125, 126]. Detailed Monte Carlo simulations uncover a complex spin texture surrounding the defect simplex whose total spins indeed sum to $S/2$ [113, 114]. The fractionalized spin-texture also provides a natural explanation for the short-range oscillating signal observed in nuclear magnetic resonance [127].

An intuitive argument for the fractionalized $S/2$ orphan spins was originally given by Henley from the viewpoint of bi-simplex structure [99]. Because each spin is shared by two simplexes

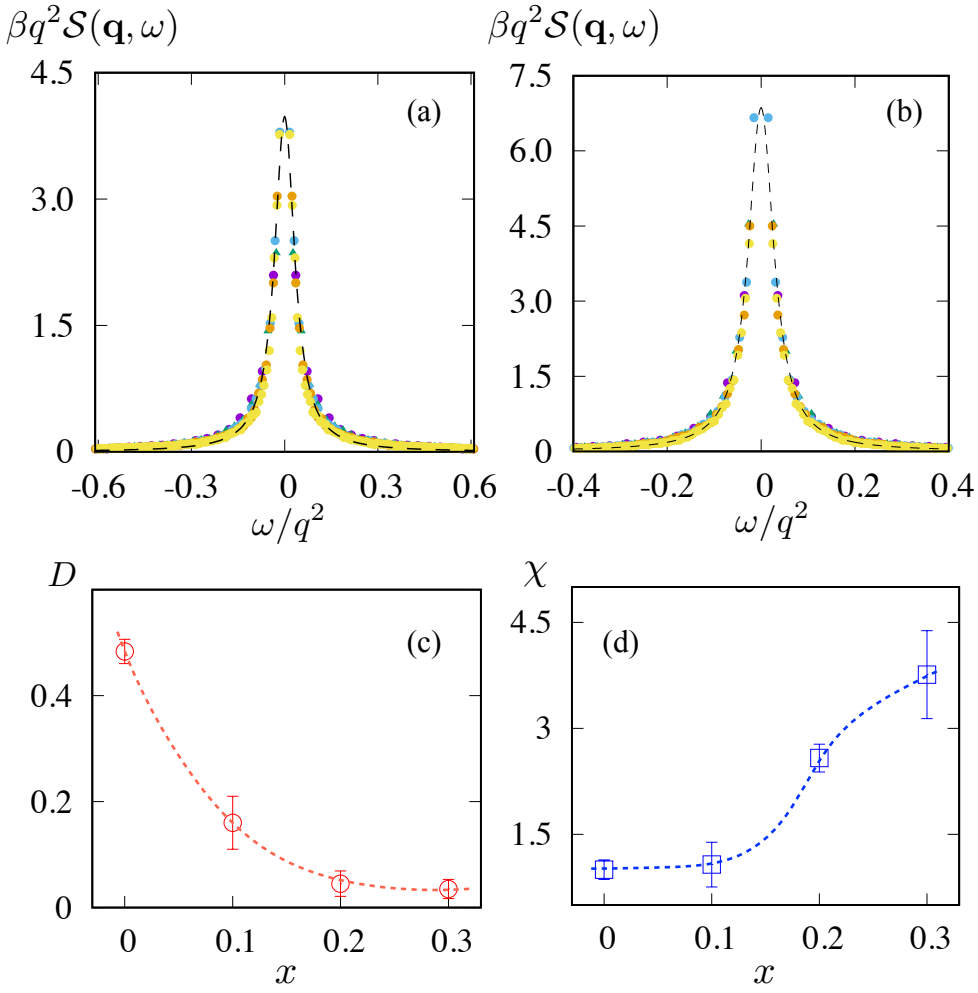

Figure 5.8: Data points collapsing of the scaled dynamical structure factor $\beta q^2 \mathcal{S}$ versus ω/q^2 for diluted bilayer kagome with (a) $x = 0.2$ and (b) $x = 0.3$ vacancy concentrations at a temperature $T = 0.01J$. The dashed lines correspond to the Lorentzian scaling function in Eq. (5.8). The extracted diffusion coefficient D and static susceptibility χ (normalized with respect to $x = 0$) as functions of the vacancy concentration are shown in panels (c) and (d), respectively.

in the bi-simplex lattices such as the kagome-bilayer, the total magnetization can be written as $\mathbf{M}_{\rm tot} = \frac{1}{2}\sum_\alpha \mathbf{L}_\alpha$, where α now runs over tetrahedral, triangular, and $q = 1$ simplexes in the presence of orphan spins. In the ground states, total spin of each tetrahedron and triangle simplex remains zero, as evidenced by Monte Carlo simulations [99]. As a result, the total magnetization of the system becomes $\mathbf{M}_{\rm tot} = \frac{1}{2}\sum_\alpha^{q=1} \mathbf{L}_\alpha$, where now the summation is restricted to $q = 1$ single-point simplexes. As shown above, such $q = 1$ simplex is just the orphan spin itself, so we have $\mathbf{M}_{\rm tot} = \frac{1}{2}\sum_{i\in{\rm orphan}} \mathbf{S}_i$, which also means that each orphan spin can be viewed as a quasi-free spin with a fractionalized length $S/2$ when in a magnetic field [99].

A natural question then is what is the dynamical manifestation of these orphan spins. To this end, we examine the spin-spin autocorrelation function $A(t)$ defined in Eq. (5.7). Fig. 5.10 shows the semi-log plot of autocorrelation functions with and without vacancies obtained from our dynamical simulations. In both cases, the initial decay of the autocorrelation can be well described by an exponential function, i.e. $A(t) \sim e^{-t/\tau}$ for small t. However, while the exponential decay persists to longer time-scales in the non-diluted system, the autocorrelation function of the diluted magnet exhibits a long-time tail, indicating a significantly reduced decline rate of the spin-autocorrelation.

This two-stage relaxation of the autocorrelation function can be understood in the framework of the two population picture [125] discussed previously, namely, the classical spin liquid of kagome bilayer can be viewed of consisting of the “correlated" population which forms momentless clusters ($\mathbf{L}_\boxtimes = \mathbf{L}_\triangle = 0$) and the population of quasi-free “orphan" spins that weakly interact with each other [114]. Of course, at very strong dilution, the set of free spins also include those completely isolated magnetic ions [99]. Dynamically, these two populations of spins are expected to behave differently. As discussed in Sec. 5.5, spin diffusion in the classical spin liquid, which is mainly driven by the zero energy modes, results in an autocorrelation function $A(t)$ which decays exponentially with time. On the other hand, since the vacancy-induced orphan spins can be viewed as nearly free spins, one expects their dynamical behavior to be similar to that of uncorrelated param-

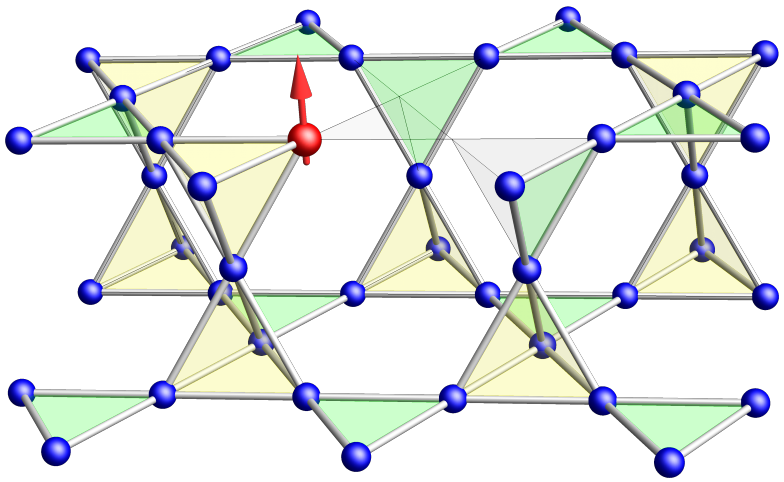

Figure 5.9: Orphan spin (red arrow) induced by vacancies in the kagome bilayer. An orphan spin resides in defective triangular simplex, in which two of the spins are removed, in either of the kagome layers. From the viewpoint of simplex, two adjacent vacancies in a triangle removes one triangle simplex , but produces a $q = 1$ (point) simplex, which is the orphan spin itself and transforming two neighboring tetrahedral into triangular simplexes.

agnet. Earlier works have shown that diffusion of Heisenberg spins in an uncorrelated paramagnet leads to a power-law tail in the autocorrelation function, i.e. $A(t) \sim 1/t^{\alpha}$ [118–122], where the exponent α depends strongly on the dimensionality. For 2D Heisenberg magnet, it is estimated to be $\alpha \approx 1.05 \pm 0.025$ [118].

To verify the above picture, we present detailed examination of both the short-time and long-time behaviors of spin autocorrelation function for a diluted kagome bilayer with a vacancy density $x = 0.3$. We performed extensive Monte Carlo and Landau-Lifshitz dynamics simulations on a $L = 48$ lattice (with total number of spins $N = 7 \times L^2 = 16128$). Over 50 independent realizations of the disorder were constructed, and for each vacancy configuration, 100 independent initial spin states are prepared at the simulation temperatures. Fig. 5.11(a) shows semi-log plot of spin-autocorrelation at various temperatures. At short time scale, the decrease of $A(t)$ can be reasonably approximated by an exponential decay $A(t) \sim e^{-t/\tau(T)}$, similar to the undiluted case, with a temperature-dependent decay time constant τ. The numerically extracted relaxation time τ, shown in Fig. 5.12(a), again exhibits a power-law dependence on temperature $\tau \sim 1/T^{\zeta}$, with an exponent $\zeta \sim 0.952 \pm 0.017$, which is similar to the undiluted case. As discussed in the previous

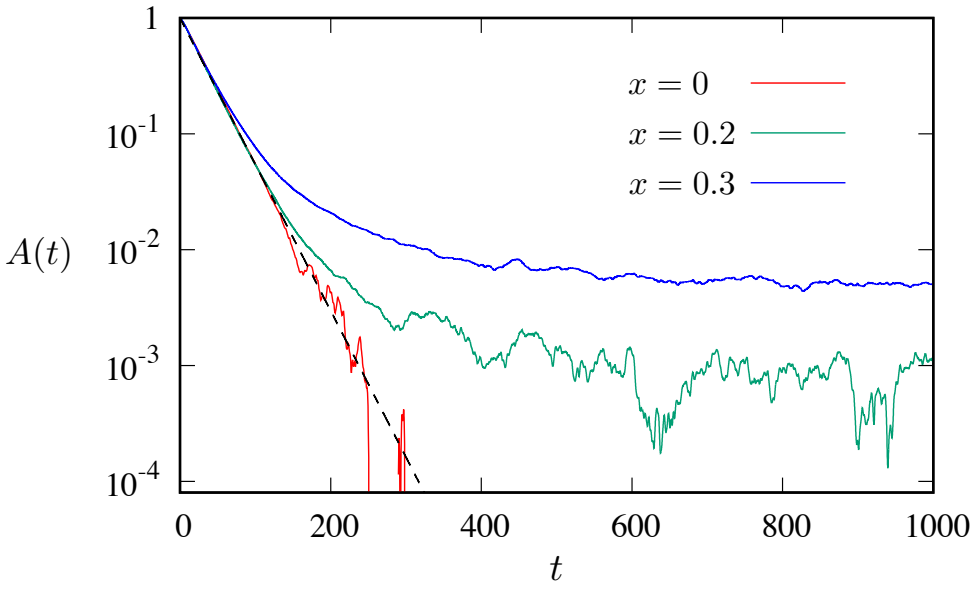

Figure 5.10: Semi-log plot of autocorrelation function $A(t)$ at $T = 0.01$ without vacancies (red) and with 20% (green) and 30% vacancies (blue), obtained from Landau-Lifshitz dynamics simulations of a $L = 48$ system. The black dashed line indicates an exponential decay $A(t) \approx e^{-t/\tau}$ at small t.

section, the spherical approximation for the classical spin liquid predicts an exponent $\zeta = 1$. It is unclear whether the deviation here is due to finite-size effect or the soft-spin approximation.

At longer time scales, the decay of the auto-correlation function slows down and turns into a power-law tail, $A(t) \sim A_\infty + \mathcal{C}(T)/t^\alpha$ with the same exponent α for different temperatures.

Interestingly, as shown in Fig. 5.12(b), the amplitude of this power-law tail also exhibits a power-law dependence $\mathcal{C} \sim 1/T^\eta$, with an exponent $\eta = 2.123 \pm 0.021$. It is also worth noting that the decay of spin auto-correlation saturates to a small but non-zero value at large times, as shown in

Fig. 5.12(a). Similar results, which can be attributed to finite-size effect, have been reported in the spin-dynamics of uncorrelated classical Heisenberg chains [121, 122].

To better understand the power-law decay and the origin of the nonzero asymptotic A_∞ in the diluted systems, we consider the dynamics of an orphan spin. At any finite temperatures, the total spin of individual simplex does not vanish identically, hence the ground-state condition Eq. (5.3) is

not strictly satisfied. Indeed, the fluctuation of simplex magnetization is given by $\langle \mathbf{L}_\alpha^2 \rangle \sim T/J$ [17, 114]. This also indicates a non-zero coupling between orphan spins and the background correlated spin liquid. This residual coupling leads to incoherent precession of orphan spins and the exponential decay of the orphan-spin autocorrelation function. On the other hand, as shown in Ref. [114], there is an emergent effective interaction between the orphan spins. At low enough temperatures, their collective dynamics induced by this residual interaction thus slows down the exponential decay of autocorrelation function that is caused by coupling to the background spin liquid, and turns it into a power-law decay, similar to the anomalous spin diffusion in classical Heisenberg magnets at high temperatures [118].

Interestingly, the exponent $\alpha \approx 2.1$ obtained from our numerical fitting is significantly different from that of the 2D paramagnet. This unusual result could be attributed to the complex interaction between the orphan spins. As demonstrated in Ref. [114], there is an emergent Heisenberg exchange interaction between the orphan spins, that is determined by the charge-charge correlator of the underlying Coulomb spin liquid. Moreover, the sign (FM vs AFM) depends on whether the two orphan spins belong to the same kagome layer or not. It has been speculated whether this complex and potentially frustrated interaction might lead to glassy dynamics at low temperatures. Indeed, although it is believed that the autocorrelation function of spin-glass exhibits an stretched exponential decay at temperatures above the glass transition T_g, general scaling rules near the glass transition point imply a cutoff power-law [128–132], such as the Ogielski form $A(t) \sim t^{-\alpha} \exp[-(\lambda t)^\beta]$, where the parameter $\lambda \to 0$ as $T \to T_g$. If the kagome-bilayer can be viewed as exhibiting a glass transition at $T = 0$, as conventional 2D spin-glasses, the autocorrelation function might be dominated by a power-law behavior at intermediate time scale before it is cut off by the stretched exponential. Further larger scale simulations are required to investigate this scenario.

The power-law tail and the associated collective behaviors also depend strongly on the density x of orphan spins. The effective interaction between two such defects separated by a distance r

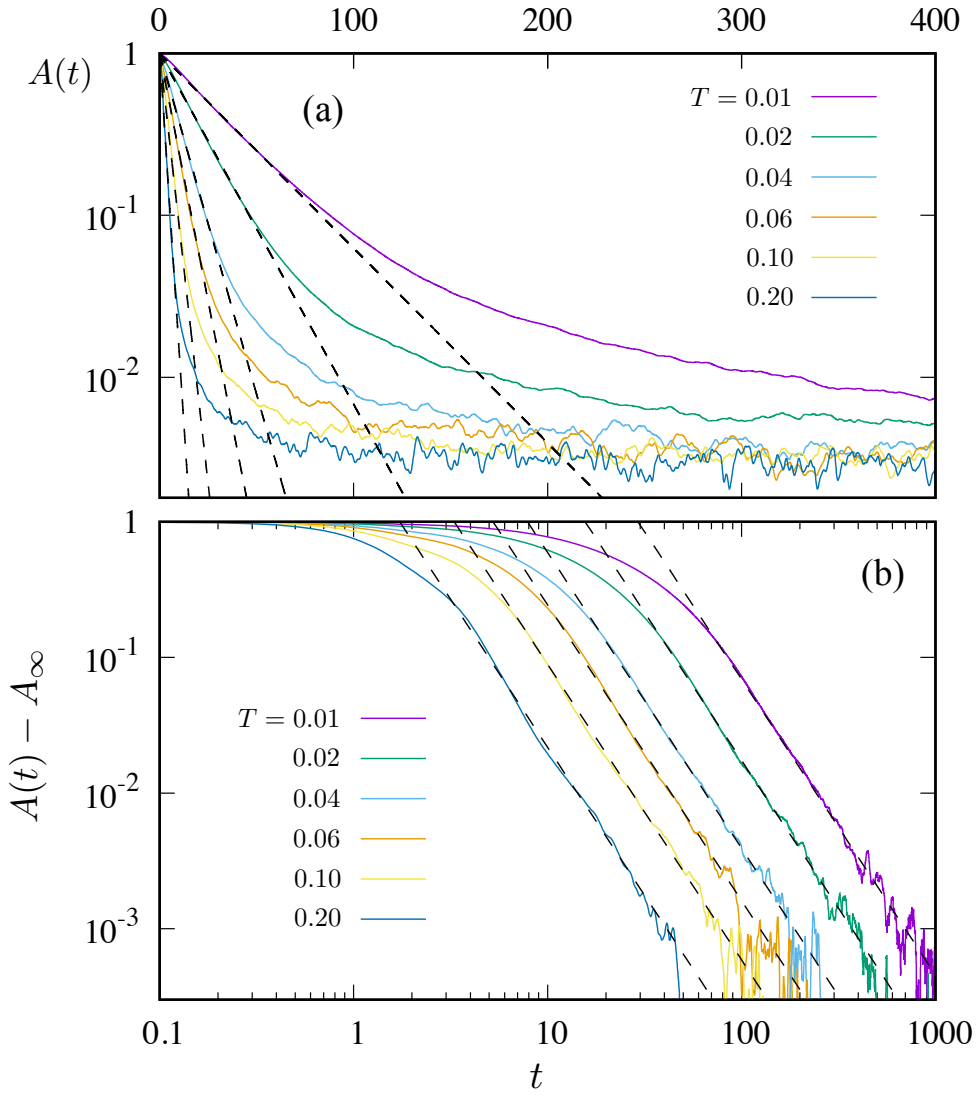

Figure 5.11: (a) Semi-log plot of the spin autocorrelation function $A(t) = \sum_i \langle \mathbf{S}_i(t) \cdot \mathbf{S}_i(0) \rangle / N$ of $L = 48$ kagome-bilayer with 30% vacancy at varying temperatures. The dashed lines correspond to the initial exponential decay of the autocorrelation function, i.e. $A(t) \sim \exp(-t/\tau)$ for small t. (b) The log-log plot of same autocorrelation functions, with the asymptotic value at large time subtracted, at varying temperatures. The dashed lines indicate power-law long-tails $A(t) \sim \mathcal{C}/t^\alpha$, with an exponent $\alpha = 2.18$.

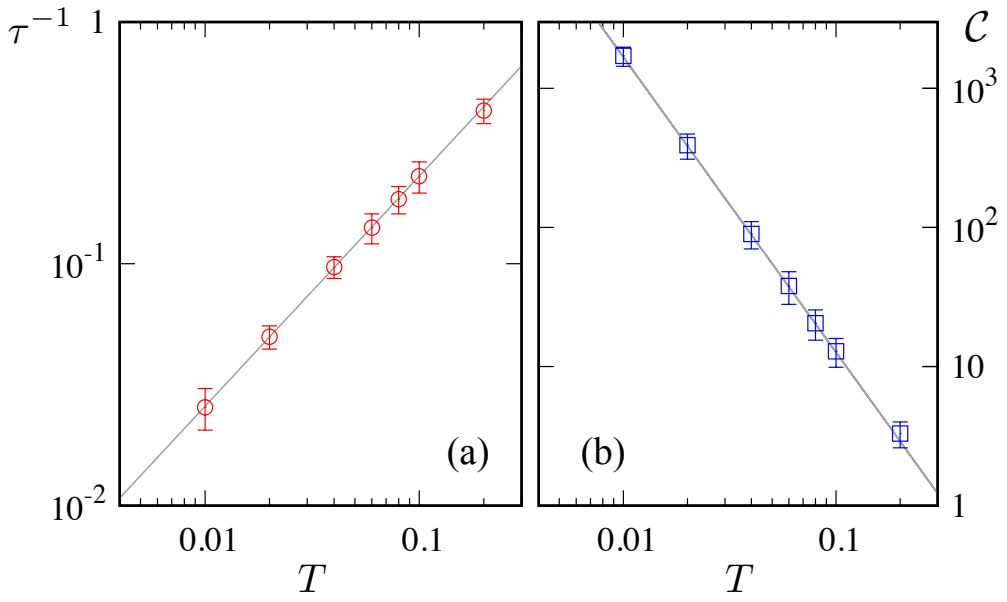

Figure 5.12: (a) The decay-time constant τ as a function of temperature T in log-log plot. The solid line corresponds to a power-law dependence $\tau \sim 1/T^{0.953}$. (b) The amplitude $\mathcal{C}$ of the power-law long-tail versus the temperature. The straight line of the log-log plot indicates a power-law relationship $\mathcal{C} \sim 1/T^{2.123}$.

is given by $J_{\text{eff}}(r) \sim T\mathcal{J}(r/\xi(T))$, where $\xi \sim 1/\sqrt{T}$ is the temperature-dependent correlation length of the background spin liquid, and the function $\mathcal{J}(r) \sim \exp(-r)$ decays exponentially at large distances [114]. The T-linear prefactor here indicates the entropic origin of the effective interaction, namely J_{eff} arises from conformational entropy of the fluctuating background correlated spins. Since the average distance between orphan spins scales as $\ell \sim 1/\sqrt{x}$, one thus obtains an average interaction $\overline{J}_{\text{eff}} \sim J_{\text{eff}}(\ell) \sim T\,\exp(-\sqrt{T/x})$, which becomes exponentially weak at small vacancy percentages. Despite this weakened interaction, the collective behavior of orphan spins would set in at a temperature that is of the order of the effective interaction. This gives the condition: $T^* \sim \overline{J}_{\text{eff}}(T^*)$. Using the expression for $\overline{J}_{\text{eff}}$ above, one thus obtain a characteristic temperature $T^* \sim x$ that decreases linearly with the reduced defect density. Physically, the thermal correlation length at this T^* is comparable to inter-orphan-spin distance.

5.7 Numerical simulation

In This section we discuss the implementation of the lattice structure and spin dynamics.

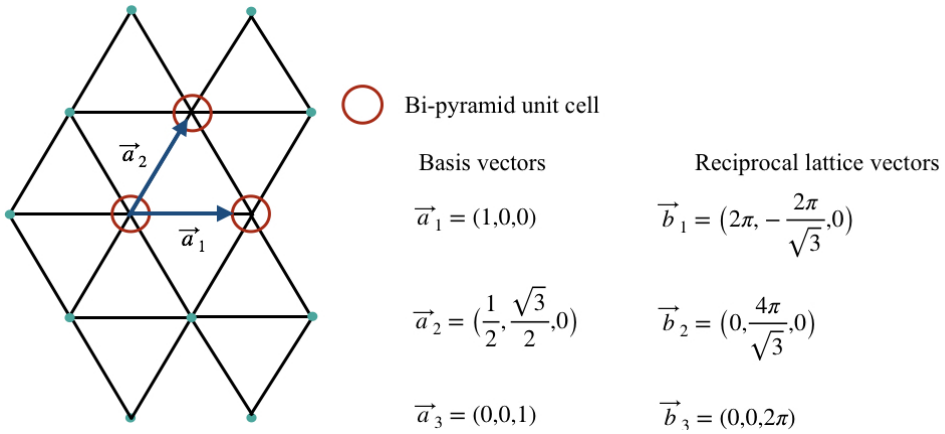

Figure 5.13: Triangular lattice basis vectors and the corresponding reciprocal lattice vectors.

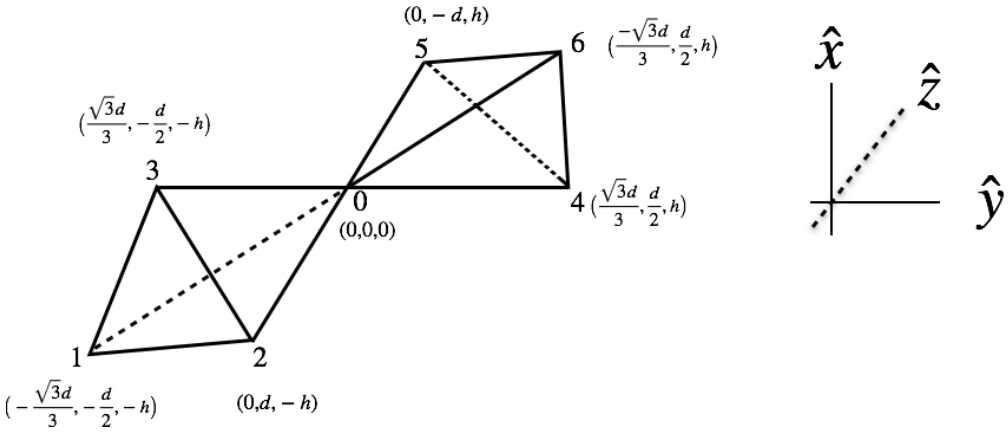

Figure 5.14: Coordinates of the corner sharing bipyramid.

5.7.1 Lattice Structure

As mentioned in section 5.3, the kagome bilayer is a Bravais triangular lattice. Every vertex on the triangular lattice is a unit cell consisting of two corner sharing oppositely oriented tetrahedra. The basis vectors and corresponding reciprocal lattice vectors are given in Figure 5.13.

Each unit cell contains 7 spins as given in the Figure 5.14. Each of the 7 spins on the unit cell can be considered as a sublattice "s" on its own. As a result, total number of spins on a lattice of linear size L are $N_S = 7L^2$. The coordinates of the Bravais triangular lattice that house the bi-pyramid unit cells are given by (X, Y), see Figure 5.13. Each spin in the unit cell is given a 3 dimensional position vector based on the basis vectors of the triangular lattice and the position (X, Y) of the

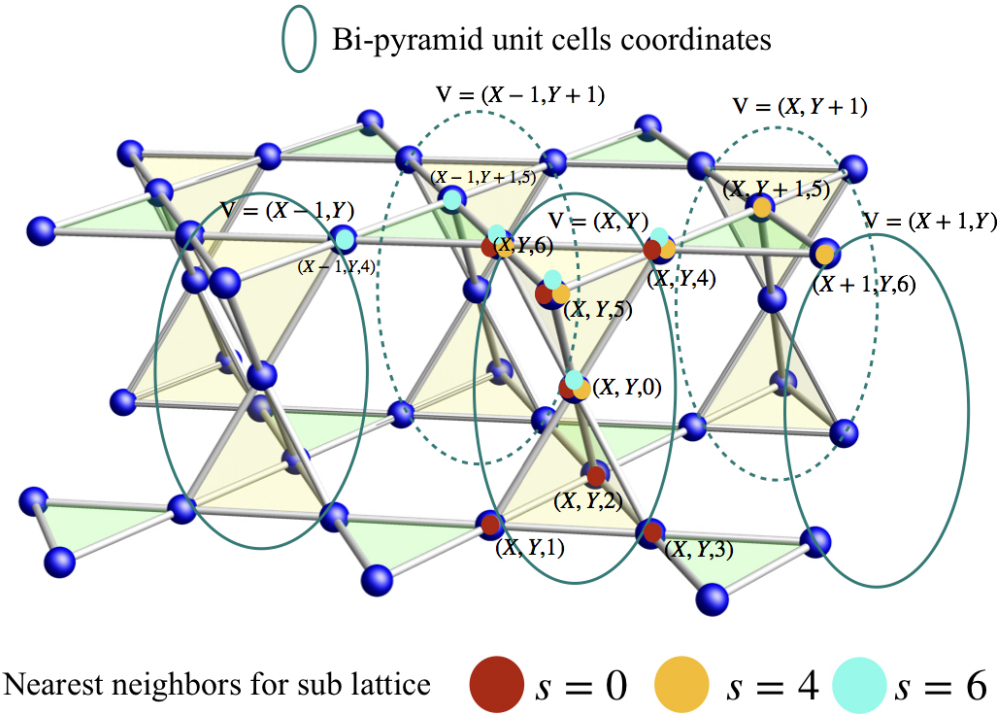

Figure 5.15: Coordinates of nearest neighbors for each of the spins on a unit cell of a quasi-2D Kagome bilayer lattice.

unit cell on the triangular lattice. A spin position vector is given by $\mathbf{r} = X\mathbf{a}_1 + Y\mathbf{a}_2 + \mathbf{ds}[s]$, where $\mathbf{ds}[s]$ is the placement vector of spin within the unit cell. These values for each of the 7 spins are given in Figure 5.14.

The spin at the center of the bi-pyramid has 6 nearest neighbors and the rest of the 6 spins on the unit cell each have 5 nearest neighbors each. We set the closest nearest neighbors individually for each sublattice. The nearest neighbors are constructed as given below and the idea is illustrated in the Figure 5.15. The coordinates of the spins on the bipyramid (X, Y) for sublattices s are shown in the Table 5.1. We consider only these neighbors for exchange interactions, for both Monte Carlo simulations and spin dynamics effective field.

After generating the lattice and fixing the nearest neighbours. Our next step is to generate temperature thermalized ground state configurations. I have employed Metropolis Hastings single spin update Monte Carlo algorithm to get ground state configurations for different temperatures. The temperature specific configurations for the system were generated using temperature annealing

Table 5.1: Nearest neighbor coordinates

$s\downarrow$ $nn\rightarrow$	1	2	3	4	5	6
0	(X,Y,s=1)	(X,Y,s=2)	(X,Y,s=3)	(X,Y,s=4)	(X,Y,s=5)	(X,Y,s=6)
1	(X,Y,s=0)	(X,Y,s=2)	(X,Y,s=3)	(X,Y-1,s=2)	(X-1,Y,s=3)	NA
2	(X,Y,s=0)	(X,Y,s=1)	(X,Y,s=3)	(X-1,Y,s=1)	(X-1,Y+1,s=3)	NA
3	(X,Y,s=0)	(X,Y,s=1)	(X,Y,s=2)	(X+1,Y,s=1)	(X+1,Y-1,s=2)	NA
4	(X,Y,s=0)	(X,Y,s=5)	(X,Y,s=6)	(X,Y+1,s=5)	(X+1,Y,s=6)	NA
5	(X,Y,s=0)	(X,Y,s=4)	(X,Y,s=6)	(X,Y-1,s=4)	(X+1,Y-1,s=6)	NA
6	(X,Y,s=0)	(X,Y,s=4)	(X,Y,s=5)	(X-1,Y,s=5)	(X-1,Y+1,s=5)	NA

method, where we start thermalizing the system from a higher temperature and slowly lower it, thereby preventing the system from getting stuck at local minima and not reaching a ground state configuration. We simulate the system dynamics using the ground state configurations as the initial starting point.

5.7.2 Spin dynamics equations

The three dimensional Heisenberg spins experience antiferromagnetic Heisenberg interaction amongst themselves, as given in Eq. 5.1 and their time trajectories are given by the Landau Lifshitz equation as given in Eq. 5.4. In this work we use the Mentink et al. SIB [31] method to integrate the Landau Lifshitz equation and simulate the spin trajectory in time. In our system the the dynamics is energy conserving and follow the method explained in section 3.2.2.

5.7.3 Structure factor simulations

Structure factor explained in Section 5.3 describes a correlation function as given in Eq. 5.5. We plot the static and dynamic plots for the correlation function. The the correlation function in the system's ground state spin configuration at time snapshot $t = 0$, gives us the static structure factor. We can describe the static structure factor by the following equation,

$$\mathcal{S}(\mathbf{q}, 0) = \langle \mathbf{S}_{\mathbf{q}}(0) \cdot \mathbf{S}^*_{\mathbf{q}}(0) \rangle \tag{5.9}$$

where $\langle \cdots \rangle$ denotes the ensemble average over independent initial states of a given temperature. We can write $\mathbf{S_q}$, the spatial Fourier transform of the instantaneous spin configuration in three dimensional complex vector form as,

$$\mathbf{S_q} = \frac{1}{\sqrt{N}} \sum_i \mathbf{S}_i(t=0) \exp(i\mathbf{q} \cdot \mathbf{r}_i) = \mathbf{C} + i\mathbf{S} \tag{5.10}$$

Then,

$$\mathcal{S}(\mathbf{q}, 0) = \langle \mathbf{C} - i\mathbf{S} | \mathbf{C} + i\mathbf{S} \rangle \tag{5.11}$$

We plot the ensemble average of $\mathcal{S}(\mathbf{q}) = \mathbf{C}^2 + \mathbf{S}^2$, where $\mathbf{q} = \frac{m}{L}\mathbf{b_1} + \frac{n}{L}\mathbf{b_2}$ represents the reciprocal lattice wave vectors and position vector of each spin $\mathbf{r}$ gives us the phase values "$\exp(i\mathbf{q} \cdot \mathbf{r}_i)$" corresponding to each $\mathbf{q}$. Both m and n belong in the range $0 \leq m < L$ and $0 \leq n < L$ where L is the linear triangular lattice size. An example of a static structure factor plot is given in Figure 5.3 (a).

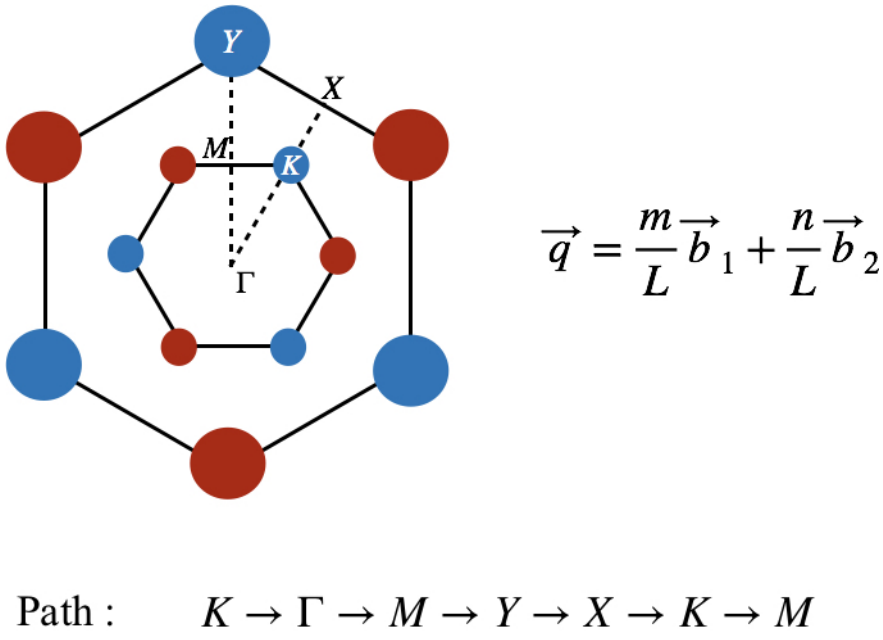

Figure 5.16: The Brillouin zone (BZ) of a triangular lattice is a hexagonal lattice. We plot the dynamic structure factor values along the path of high symmetry points on the BZ.

As seen in section 5.5, the dynamic structure factor given by Eq. 5.6 represents the time integral of the space-time Fourier transform of the spin-spin correlator. Such plots can be made for any given range of wave vectors. Some dynamic structure factor plots at specific frequencies ω are given in Figure 5.3 (b) and (c). We have also studied the dynamic structure factor figures for specific values of wave vectors $\mathbf{q} < 1$ to check the limit of spin diffusion, see Figure 5.6. More conventionally, to understand the important properties of the correlations in the spins, dynamic structure factor plots in Figures 5.2 and 5.7 are computed along high symmetry points on the Brillouin zone. The Brillouin zone of a triangular lattice is a hexagonal lattice. The path of the structure factor figure is shown in Figure 5.16. The $\mathbf{q}$ coordinates of the high symmetry points for a hexagonal Brillouin zone are given in Table 5.2

Table 5.2: High symmetry point on the hexagonal Brillouin zone

Point	$\mathbf{q}$-Coordinates
Γ	$\left(0, 0\right)$
K	$\left(\frac{2\pi}{3}, \frac{2\pi}{\sqrt{3}}\right)$
M	$\left(0, \frac{2\pi}{\sqrt{3}}\right)$
Y	$\left(0, \frac{4\pi}{\sqrt{3}}\right)$
X	$\left(\pi, \pi\sqrt{3}\right)$

5.8 Discussion and outlook

To summarize, we have extensively characterized the spin dynamics in the liquid phase of Heisenberg antiferromagnet on the kagome bilayer, which is relevant for the frustrated magnet SCGO. By computing the dynamical structure factor at different temperatures and dilutions, we show that the spin excitations are dominated by spin diffusion in the low energy, long time regime. The spin diffusion constant depends weakly on temperature, but decreases with dilution. Another interesting result is the half moon pattern of the dynamical structure factor with energy $\omega \gtrsim J$. Similar features have recently been observed in some pyrochlore compounds, it remains to be seen whether

these remnants of the propagating spin waves can be observed in SCGO. Our simulations on diluted bilayer kagome shows that spin diffusion remains the dominant process in the presence of site disorder. This result further confirms, from the dynamical viewpoint, that site-disorder itself does not immediately cause glassy behaviors in the classical spin liquid, although the diffusion relaxation time becomes longer with increasing disorder. However, for disorder due to non-magnetic vacancies, the presence of so-called orphan spins results in an intriguing power-law tail in the spin-autocorrelation function. This power-law slow dynamics indicates that the system might be on the verge of a glass transition, which could be induced by other perturbations.

As discussed above, our work offers important benchmark for future dynamics studies of kagome bilayer that include other perturbations. Of particular interest are those perturbations that might transform the classical spin liquid into either the conventional spin glass or the more exotic spin jam. Indeed, since the diffusive spin dynamics in highly frustrated magnets is mainly driven by the zero-energy modes, one expects a diminishing diffusivity when the number of such zero modes is significantly reduced. For example, the entropic barrier in the coplanar phase of kagome reduces the *continuous* weather-van modes to *discrete* zero modes defined on closed loops. It has been proposed that the much slower relaxation of these discrete loops might give rise to glassiness without intrinsic disorder in kagome [133, 134]. However, the coplanar phase induced by thermal order-by-disorder seems to remain a classical spin liquid [80]. A transition into the glassy regime might still occur at a lower temperature when the dynamics is dominated by quantum tunneling of loops [133].

Contrary to kagome Heisenberg antiferromagnets, there is no thermal induced coplanar or collinear phase in kagome bilayer. On the other hand, it has been proposed in Ref. [105] that a coplanar regime, in which spins in each tetrahedron are collinear, can be induced by quantum fluctuations. Moreover, different coplanar ground states can be mapped to discrete hexagonal tilings. Importantly, there is no continuous weather-van modes in this coplanar regime, and the only zero-energy modes are system-wide extended strings [105]. As jamming transition often occurs in such con-

strained discrete models, the resultant coplanar phase is dubbed the spin jam [98, 105]. It is argued that quantum fluctuations transform the degenerate classical ground-state manifold into a rugged landscape that is different from that of conventional spin glass. While this spin-jam picture seem to explain some properties of SCGO and other similar glassy magnets, such as the much weaker memory effect [102, 104], an important open question is to see how dynamical behaviors characteristic to spin-jam evolve from the classical spin liquid, which will be left for future study.

CONCLUSION

Frustration in spin systems arise when the interactions between neighboring magnetic moments cannot be satisfied simultaneously. This can be a direct consequence of incompatibility between magnetic interactions and the underlying geometry of the lattice or due to anisotropy in magnetic interaction exchanges. Frustration gives rise to many exotic phenomena, a prominent one being classical spin liquids (CSLs). CSLs are characterized by their extensive ground state degeneracy and absence of ordered states even at very low temperatures upto absolute zero. Nonetheless classical spin liquids are known to exhibit strong, algebraically decaying correlations. The degeneracy in the ground state manifold is quite accidental and not a consequence of symmetries in the Hamiltonian.

In Chapter **4**, I have explained the details of our research on frustrated spin-orbit magnets where a dominant off-diagonal exchange, the so-called Γ term results in a classical spin liquid phase with macroscopic ground-state degeneracy. We demonstrated that the system undergoes a phase transition driven by thermal order-by-disorder at a critical temperature $T_C \sim 0.04|\Gamma|$ corresponding to plaquette ordering of hexagonal fluxes. We characterized the nature of the plaquette-ordering transition using Monte Carlo simulations and finite-size analysis. We also studied the dynamical behavior of fluxes and the influence of other types of interactions on the phase transition. Our work was motivated by the recent enormous interest in frustrated spin-orbit magnets, where the spin interactions in certain $4d$ and $5d$ Mott insulators are dominated by the anisotropic Kitaev-type exchange. The results on the thermodynamic behavior of the pure Γ model will help in the search for spin liquids in frustrated spin-orbit magnets as well add to the knowledge of exotic phases found in frustrated systems.

In Chapter **5**, we report on the spin dynamical simulations of the Heisenberg antiferromagnet with nearest neighbor interactions on a quasi-2D kagome bilayer. $SrCr_{9p}Ga_{12-9p}O_{19}$ (SCGO) is one

of the most intensely studied frustrated magnets, which inspired our work on this system. Geometrically, SCGO belongs to a class of frustrated Heisenberg antiferromagnets on the networks of corner-sharing tetrahedra which enters an unconventional spin-glass phase below a certain low temperature $T_g \sim 3.5 - 7K$. Considerable efforts have been devoted to understanding the unusual spin glass phase in SCGO. We discuss the implications of our work for the glassy behaviors observed in the archetypal frustrated magnet SCGO.

The Heisenberg antiferromagnet on the kagome bilayer exists in a classical spin liquid phase arising from geometric frustration. By combining Monte Carlo simulations with precessional spin dynamics simulations, we computed the dynamical structure factor and investigated the thermal and dilution effects. We have characterized the diffusion dynamics of the "correlated" spin clusters as well as the site diluted system. The spin diffusion constant depends weakly on temperature, but decreases with dilution. Our simulations on diluted bilayer kagome shows that spin diffusion remains the dominant process in the presence of site disorder. We have further confirmed that from the dynamical point of view, site-disorder itself does not cause glassy behaviors in the classical spin liquid, although the diffusion relaxation time becomes longer with increasing disorder. Our work provides important benchmark for future dynamics studies of kagome bilayer that include other perturbations, particularly those perturbations that might transform the classical spin liquid into either the conventional spin glass or the more exotic spin jam.

BIBLIOGRAPHY

[1] Stephen Blundell. “Magnetism in Condensed Matter”. In: *American Journal of Physics* 71.1 (Jan. 1, 2003). Publisher: American Association of Physics Teachers, pp. 94–95.

[2] David C. Johnston. “Magnetic dipole interactions in crystals”. In: *Physical Review B* 93.1 (Jan. 13, 2016). Publisher: American Physical Society, p. 014421.

[3] Marc Mezard, Giorgio Parisi, and Miguel Angel Virasoro. *Spin Glass Theory And Beyond: An Introduction To The Replica Method And Its Applications*. Google-Books-ID: DwY8DQAAQBAJ. World Scientific Publishing Company, Nov. 1, 1987. 477 pp. ISBN: 978-981-310-391-7.

[4] Alexei Kitaev. “Anyons in an exactly solved model and beyond”. In: *Annals of Physics*. January Special Issue 321.1 (Jan. 1, 2006), pp. 2–111.

[5] A P Ramirez. “Strongly Geometrically Frustrated Magnets”. In: *Annual Review of Materials Science* 24.1 (1994), pp. 453–480.

[6] J. M. Luttinger and L. Tisza. “Theory of Dipole Interaction in Crystals”. In: *Physical Review* 70.11 (Dec. 1, 1946). Publisher: American Physical Society, pp. 954–964.

[7] D. A. Pesin and Leon Balents. “Mott physics and band topology in materials with strong spin-orbit interaction”. In: *Nature Physics* 6.5 (May 2010), pp. 376–381. arXiv: 0907.2962.

[8] B. J. Kim et al. “Phase-Sensitive Observation of a Spin-Orbital Mott State in Sr2IrO4”. In: *Science* (2009).

[9] Samarth Chandra, Kabir Ramola, and Deepak Dhar. “Classical Heisenberg spins on a hexagonal lattice with Kitaev couplings”. In: *Physical Review E* 82.3 (Sept. 8, 2010). Publisher: American Physical Society, p. 031113.

[10] Eran Sela et al. “Order-by-disorder and spin-orbital liquids in a distorted Heisenberg-Kitaev model”. In: *Physical Review B* 90.3 (July 14, 2014). Publisher: American Physical Society, p. 035113.

[11] Christopher L. Henley. “The "Coulomb Phase" in Frustrated Systems”. In: *Annual Review of Condensed Matter Physics* 1.1 (2010), pp. 179–210.

[12] Giniyat Khaliullin. *Orbital order and fluctuations in Mott insulators*. 2006.

[13] G. Jackeli and G. Khaliullin. “Mott Insulators in the Strong Spin-Orbit Coupling Limit: From Heisenberg to a Quantum Compass and Kitaev Models”. In: *Physical Review Letters* 102.1 (Jan. 6, 2009). Publisher: American Physical Society, p. 017205.

[14] Craig C. Price and Natalia B. Perkins. “Critical Properties of the Kitaev-Heisenberg Model”. In: *Physical Review Letters* 109.18 (Nov. 2, 2012). Publisher: American Physical Society, p. 187201.

[15] Craig Price and Natalia B. Perkins. “Finite-temperature phase diagram of the classical Kitaev-Heisenberg model”. In: *Physical Review B* 88.2 (July 15, 2013). Publisher: American Physical Society, p. 024410.

[16] Gia-Wei Chern et al. “Kitaev-Heisenberg model in a magnetic field: order-by-disorder and commensurate-incommensurate transitions”. In: *Physical Review B* 95.14 (Apr. 21, 2017), p. 144427. arXiv: 1611.03436.

[17] R. Moessner and J. T. Chalker. “Properties of a Classical Spin Liquid: The Heisenberg Pyrochlore Antiferromagnet”. In: *Physical Review Letters* 80.13 (Mar. 30, 1998). Publisher: American Physical Society, pp. 2929–2932.

[18] R. Moessner and J. T. Chalker. “Low-temperature properties of classical geometrically frustrated antiferromagnets”. In: *Physical Review B* 58.18 (Nov. 1, 1998). Publisher: American Physical Society, pp. 12049–12062.

[19] Jacques Villain. “Insulating spin glasses”. In: *Zeitschrift fur Physik B Condensed Matter* 33.1 (Mar. 1, 1979), pp. 31–42.

[20] J. Villain et al. “Order as an effect of disorder”. In: *Journal de Physique* 41.11 (1980), pp. 1263–1272.

[21] E. F. Shender and P. C. W. Holdsworth. “Order by Disorder and Topology in Frustrated Magnetic Systems”. In: *Fluctuations and Order*. Ed. by Mark Millonas. Series Title: Institute for Nonlinear Science. New York, NY: Springer US, 1996, pp. 259–279. ISBN: 978-1-4612-8463-5 978-1-4612-3992-5.

[22] D. A. Garanin and Benjamin Canals. “Classical spin liquid: Exact solution for the infinite-component antiferromagnetic model on the kagomé lattice”. In: *Phys. Rev. B* 59 (1 Jan. 1999), pp. 443–456.

[23] S. V. Isakov et al. “Dipolar Spin Correlations in Classical Pyrochlore Magnets”. In: *Physical Review Letters* 93.16 (Oct. 14, 2004). Publisher: American Physical Society, p. 167204.

[24] C. L. Henley. “Power-law spin correlations in pyrochlore antiferromagnets”. In: *Physical Review B* 71.1 (Jan. 19, 2005). Publisher: American Physical Society, p. 014424.

[25] G. H. Wannier. “Antiferromagnetism. The Triangular Ising Net”. In: *Physical Review* 79.2 (July 15, 1950). Publisher: American Physical Society, pp. 357–364.

[26] J. T. Chalker, P. C. W. Holdsworth, and E. F. Shender. “Hidden order in a frustrated system: Properties of the Heisenberg Kagom\’e antiferromagnet”. In: *Physical Review Letters* 68.6 (Feb. 10, 1992). Publisher: American Physical Society, pp. 855–858.

[27] Jan N. Reimers and A. J. Berlinsky. “Order by disorder in the classical Heisenberg kagom\’e antiferromagnet”. In: *Physical Review B* 48.13 (Oct. 1, 1993). Publisher: American Physical Society, pp. 9539–9554.

[28] David P Landau and Kurt Binder. “A Guide to Monte Carlo Simulations in Statistical Physics, Third Edition”. In: (), p. 489.

[29] Bernd A. Berg. “Introduction to Markov Chain Monte Carlo Simulations and their Statistical Analysis”. In: (Oct. 19, 2004).

[30] Nicholas Metropolis et al. “Equation of State Calculations by Fast Computing Machines”. In: *The Journal of Chemical Physics* 21.6 (June 1, 1953). Publisher: American Institute of Physics, pp. 1087–1092.

[31] J H Mentink et al. “Stable and fast semi-implicit integration of the stochastic Landau–Lifshitz equation”. In: 22.17 (Apr. 2010), p. 176001.

[32] William Witczak-Krempa et al. “Correlated Quantum Phenomena in the Strong Spin-Orbit Regime”. In: *Annual Review of Condensed Matter Physics* 5.1 (2014). _eprint: https://doi.org/10.1146/annu conmatphys-020911-125138, pp. 57–82.

[33] K. Kugel and D. I. Khomskii. “The Jahn-Teller effect and magnetism: transition metal compounds”. In: *Soviet Physics Uspekhi* 25.4 (Apr. 30, 1982). Publisher: IOP Publishing, p. 231.

[34] Zohar Nussinov and Jeroen van den Brink. “Compass models: Theory and physical motivations”. In: *Reviews of Modern Physics* 87.1 (Jan. 12, 2015). Publisher: American Physical Society, pp. 1–59.

[35] Congjun Wu. “Orbital Ordering and Frustration of p-Band Mott Insulators”. In: *Physical Review Letters* 100.20 (May 22, 2008). Publisher: American Physical Society, p. 200406.

[36] Erhai Zhao and W. Vincent Liu. “Orbital Order in Mott Insulators of Spinless p-Band Fermions”. In: *Physical Review Letters* 100.16 (Apr. 22, 2008). Publisher: American Physical Society, p. 160403.

[37] Gia-Wei Chern and Congjun Wu. “Orbital ice: An exact Coulomb phase on the diamond lattice”. In: *Physical Review E* 84.6 (Dec. 15, 2011). Publisher: American Physical Society, p. 061127.

[38] Gia-Wei Chern and R. Moessner. “Dipolar order by disorder in the classical Heisenberg antiferromagnet on the kagome lattice”. In: *Physical Review Letters* 110.7 (Feb. 15, 2013), p. 077201.

[39] C. Lacroix, P. Mendels, and F. Mila. “Introduction to frustrated magnetism : materials, experiments, theory”. In: 2011.

[40] J. Knolle et al. “Dynamics of a Two-Dimensional Quantum Spin Liquid: Signatures of Emergent Majorana Fermions and Fluxes”. In: *Physical Review Letters* 112.20 (May 21, 2014). Publisher: American Physical Society, p. 207203.

[41] Joji Nasu, Masafumi Udagawa, and Yukitoshi Motome. “Vaporization of Kitaev Spin Liquids”. In: *Physical Review Letters* 113.19 (Nov. 7, 2014). Publisher: American Physical Society, p. 197205.

[42] G. Baskaran, Diptiman Sen, and R. Shankar. “Spin-S Kitaev model: Classical ground states, order from disorder, and exact correlation functions”. In: *Physical Review B* 78.11 (Sept. 22, 2008). Publisher: American Physical Society, p. 115116.

[43] Ioannis Rousochatzakis, Yuriy Sizyuk, and Natalia B. Perkins. “Quantum spin liquid in the semiclassical regime”. In: *Nature Communications* 9 (Apr. 23, 2018), p. 1575.

[44] Ji Chaloupka, George Jackeli, and Giniyat Khaliullin. “Kitaev-Heisenberg Model on a Honeycomb Lattice: Possible Exotic Phases in Iridium Oxides $A_2\mathrm{IrO}_3$”. In: *Phys. Rev. Lett.* 105 (2 July 2010), p. 027204.

[45] Ji Chaloupka, George Jackeli, and G. Khaliullin. “Zigzag Magnetic Order in the Iridium Oxide $\mathrm{Na}_2\mathrm{IrO}_3$”. In: *Phys. Rev. Lett.* 110 (9 Feb. 2013), p. 097204.

[46] Simon Trebst. “Kitaev Materials”. In: *arXiv:1701.07056 [cond-mat]* (Jan. 24, 2017).

[47] Yogesh Singh et al. “Relevance of the Heisenberg-Kitaev Model for the Honeycomb Lattice Iridates $A_2\mathrm{IrO}_3$”. In: *Phys. Rev. Lett.* 108 (12 Mar. 2012), p. 127203.

[48] S. K. Choi et al. “Spin Waves and Revised Crystal Structure of Honeycomb Iridate $\mathrm{Na}_2\mathrm{IrO}_3$”. In: *Phys. Rev. Lett.* 108 (12 Mar. 2012), p. 127204.

[49] Feng Ye et al. “Direct evidence of a zigzag spin-chain structure in the honeycomb lattice: A neutron and x-ray diffraction investigation of single-crystal $\mathrm{Na}_2\mathrm{IrO}_3$”. In: *Phys. Rev. B* 85 (18 May 2012), p. 180403.

[50] Sae Hwan Chun et al. “Direct evidence for dominant bond-directional interactions in a honeycomb lattice iridate Na_2IrO_3”. In: *Nature Physics* 11.6 (May 11, 2015).

[51] S. C. Williams et al. “Incommensurate counterrotating magnetic order stabilized by Kitaev interactions in the layered honeycomb α-Li_2IrO_3”. In: *Phys. Rev. B* 93 (19 May 2016), p. 195158.

[52] K. W. Plumb et al. “A spin-orbit assisted Mott insulator on a honeycomb lattice α-$RuCl_3$”. In: *Phys. Rev. B* 90 (4 July 2014), p. 041112.

[53] J. A. Sears et al. “Magnetic order in α-$RuCl_3$ A honeycomb-lattice quantum magnet with strong spin-orbit coupling”. In: *Phys. Rev. B* 91 (14 Apr. 2015), p. 144420.

[54] Yumi Kubota et al. “Successive magnetic phase transitions in α-$RuCl_3$: XY-like frustrated magnet on the honeycomb lattice”. In: *Phys. Rev. B* 91 (9 Mar. 2015), p. 094422.

[55] R. D. Johnson et al. “Monoclinic crystal structure of α-$RuCl_3$ and the zigzag antiferromagnetic ground state”. In: *Phys. Rev. B* 92 (23 Dec. 2015), p. 235119.

[56] A. Biffin et al. “Unconventional magnetic order on the hyperhoneycomb Kitaev lattice in β-Li_2IrO_3: Full solution via magnetic resonant x-ray diffraction”. In: *Phys. Rev. B* 90 (20 Nov. 2014), p. 205116.

[57] A. Biffin et al. “Noncoplanar and Counterrotating Incommensurate Magnetic Order Stabilized by Kitaev Interactions in γ-Li_2IrO_3”. In: *Phys. Rev. Lett.* 113 (19 Nov. 2014), p. 197201.

[58] K. A. Modic et al. “Realization of a three-dimensional spin-anisotropic harmonic honeycomb iridate”. In: *Nature Communications* 5 (June 27, 2014), p. 4203.

[59] Jiacheng Zheng et al. “Gapless Spin Excitations in the Field-Induced Quantum Spin Liquid Phase of α-$RuCl_3$”. In: *Phys. Rev. Lett.* 119 (22 Dec. 2017), p. 227208.

[60] Zhe Wang et al. “Magnetic Excitations and Continuum of a Possibly Field-Induced Quantum Spin Liquid in α-$RuCl_3$”. In: *Phys. Rev. Lett.* 119 (22 Nov. 2017), p. 227202.

[61] S.-H. Baek et al. “Evidence for a Field-Induced Quantum Spin Liquid in α-$RuCl_3$”. In: *Phys. Rev. Lett.* 119 (3 July 2017), p. 037201.

[62] T. Takayama et al. “Hyperhoneycomb Iridate β-Li_2IrO_3 as a Platform for Kitaev Magnetism”. In: *Phys. Rev. Lett.* 114 (7 Feb. 2015), p. 077202.

[63] L. S. I. Veiga et al. “Pressure tuning of bond-directional exchange interactions and magnetic frustration in the hyperhoneycomb iridate β-Li_2IrO_3”. In: *Phys. Rev. B* 96 (14 Oct. 2017), p. 140402.

[64] Yuriy Sizyuk et al. “Importance of anisotropic exchange interactions in honeycomb iridates: Minimal model for zigzag antiferromagnetic order in Na_2IrO_3.” In: *Phys. Rev. B* 90 (15 Oct. 2014), p. 155126.

[65] Jeffrey G. Rau, Eric Kin-Ho Lee, and Hae-Young Kee. “Generic Spin Model for the Honeycomb Iridates beyond the Kitaev Limit”. In: *Phys. Rev. Lett.* 112 (7 Feb. 2014), p. 077204.

[66] Stephen M. Winter et al. “Challenges in design of Kitaev materials: Magnetic interactions from competing energy scales”. In: *Phys. Rev. B* 93 (21 June 2016), p. 214431.

[67] Heung-Sik Kim and Hae-Young Kee. “Crystal structure and magnetism in α-$RuCl_3$: An ab initio study”. In: *Phys. Rev. B* 93 (15 Apr. 2016), p. 155143.

[68] Satoshi Nishimoto et al. “Strongly frustrated triangular spin lattice emerging from triplet dimer formation in honeycomb Li_2IrO_3”. In: *Nature Communications* 7.1 (Jan. 18, 2016), p. 10273.

[69] Lukas Janssen, Eric C. Andrade, and Matthias Vojta. “Magnetization processes of zigzag states on the honeycomb lattice: Identifying spin models for α-$RuCl_3$ and Na_2IrO_3”. In: *Phys. Rev. B* 96 (6 Aug. 2017), p. 064430.

[70] Matthias Gohlke et al. “Quantum spin liquid signatures in Kitaev-like frustrated magnets”. In: *Phys. Rev. B* 97 (7 Feb. 2018), p. 075126.

[71] Heung-Sik Kim, Yong Baek Kim, and Hae-Young Kee. “Revealing frustrated local moment model for pressurized hyperhoneycomb iridate: Paving the way toward a quantum spin liquid”. In: *Phys. Rev. B* 94 (24 Dec. 2016), p. 245127.

[72] M. Majumder et al. “Breakdown of magnetic order in the pressurized Kitaev iridate Li_2IrO_3”. In: *Physical Review Letters* 120.23 (June 8, 2018), p. 237202. arXiv: 1802.06819.

[73] Ioannis Rousochatzakis and Natalia B. Perkins. “Classical Spin Liquid Instability Driven By Off-Diagonal Exchange in Strong Spin-Orbit Magnets”. In: *Phys. Rev. Lett.* 118 (14 Apr. 2017), p. 147204.

[74] Preetha Saha et al. “Hidden plaquette order in a classical spin liquid stabilized by strong off-diagonal exchange”. In: *Physical review letters* 122.25 (2019), p. 257204.

[75] R. Ganesh, Jeroen van den Brink, and Satoshi Nishimoto. “Deconfined Criticality in the Frustrated Heisenberg Honeycomb Antiferromagnet”. In: *Phys. Rev. Lett.* 110 (12 Mar. 2013), p. 127203.

[76] Zhenyue Zhu, David A. Huse, and Steven R. White. “Weak Plaquette Valence Bond Order in the $S{=}1/2$ Honeycomb $J_1{-}J_2$ Heisenberg Model”. In: *Phys. Rev. Lett.* 110 (12 Mar. 2013), p. 127205.

[77] H. H. Zhao et al. “Plaquette order and deconfined quantum critical point in the spin-1 bilinear-biquadratic Heisenberg model on the honeycomb lattice”. In: *Phys. Rev. B* 85 (13 Apr. 2012), p. 134416.

[78] Shou-Shu Gong, Wei Zhu, and D. N. Sheng. “Quantum phase diagram of the spin-1 $J_1 - J_2$ Heisenberg model on the honeycomb lattice”. In: *Phys. Rev. B* 92 (19 Nov. 2015), p. 195110.

[79] F. Y. Wu. “The Potts model”. In: *Rev. Mod. Phys.* 54 (1 Jan. 1982), pp. 235–268.

[80] Mathieu Taillefumier et al. “Semiclassical spin dynamics of the antiferromagnetic Heisenberg model on the kagome lattice”. In: *Phys. Rev. B* 90 (6 Aug. 2014), p. 064419.

[81] A. M. Samarakoon et al. “Comprehensive study of the dynamics of a classical Kitaev spin liquid”. In: *Phys. Rev. B* 96 (13 Oct. 2017), p. 134408.

[82] F. Baumberger et al. “Electron Coherence in a Melting Lead Monolayer”. In: *Science* 306.5705 (2004), pp. 2221–2224.

[83] Keun Su Kim and Han Woong Yeom. “Radial Band Structure of Electrons in Liquid Metals”. In: *Phys. Rev. Lett.* 107 (13 Sept. 2011), p. 136402.

[84] Zhongzheng Tian et al. “Honeycomb-lattice Gamma model in a magnetic field: hidden N\’eel order and spin-flop transition”. In: *arXiv preprint arXiv:2106.16121* (2021).

[85] X. Obradors et al. “Magnetic frustration and lattice dimensionality in SrCr8Ga4O19”. In: *Solid State Communications* 65.3 (1988), pp. 189–192.

[86] A. P. Ramirez, G. P. Espinosa, and A. S. Cooper. “Strong frustration and dilution-enhanced order in a quasi-2D spin glass”. In: *Phys. Rev. Lett.* 64 (17 Apr. 1990), pp. 2070–2073.

[87] A. P. Ramirez, G. P. Espinosa, and A. S. Cooper. “Elementary excitations in a diluted antiferromagnetic Kagomé lattice”. In: *Phys. Rev. B* 45 (5 Feb. 1992), pp. 2505–2508.

[88] C. Broholm et al. “Antiferromagnetic fluctuations and short-range order in a Kagomé lattice”. In: *Phys. Rev. Lett.* 65 (25 Dec. 1990), pp. 3173–3176.

[89] Y. J. Uemura et al. “Spin Fluctuations in Frustrated Kagomé Lattice System $\mathrm{SrCr_8Ga_4O_{19}}$ Studied by Muon Spin Relaxation”. In: *Phys. Rev. Lett.* 73 (24 Dec. 1994), pp. 3306–3309.

[90] S.-H. Lee et al. “Isolated Spin Pairs and Two-Dimensional Magnetism in $\mathrm{SrCr_{9p}Ga_{12-9p}}O_{19}$”. In: *Phys. Rev. Lett.* 76 (23 June 1996), pp. 4424–4427.

[91] P. Schiffer et al. “Interaction-Induced Spin Coplanarity in a Kagomé Magnet: $\mathrm{SrCr_{9p}Ga_{12-9p}O_{19}}$”. In: *Phys. Rev. Lett.* 77 (10 Sept. 1996), pp. 2085–2088.

[92] S.-H Lee et al. “Spin-glass and non–spin-glass features of a geometrically frustrated magnet”. In: 35.2 (July 1996), pp. 127–132.

[93] A. P. Ramirez, B. Hessen, and M. Winklemann. “Entropy Balance and Evidence for Local Spin Singlets in a Kagomé-Like Magnet”. In: *Phys. Rev. Lett.* 84 (13 Mar. 2000), pp. 2957–2960.

[94] A. Keren et al. “Magnetic Dilution in the Geometrically Frustrated $\mathrm{SrCr}_{9p}\mathrm{Ga}_{12-9p}O_{19}$ and the Role of Local Dynamics: A Muon Spin Relaxation Study”. In: *Phys. Rev. Lett.* 84 (15 Apr. 2000), pp. 3450–3453.

[95] P. Mendels et al. “Ga NMR Study of the Local Susceptibility in Kagomé-Based $\mathrm{SrCr}_8\mathrm{Ga}_4O_{19}$: Pseudogap and Paramagnetic Defects”. In: *Phys. Rev. Lett.* 85 (16 Oct. 2000), pp. 3496–3499.

[96] David Bono et al. “Correlations, spin dynamics, defects: the highly-frustrated Kagom\’{e} bilayer”. In: *Low Temperature Physics* 31.8 (Aug. 2005), pp. 704–721. arXiv: cond-mat/0503496.

[97] K. Iida, S.-H. Lee, and S.-W. Cheong. “Coexisting Order and Disorder Hidden in a Quasi-Two-Dimensional Frustrated Magnet”. In: *Phys. Rev. Lett.* 108 (21 May 2012), p. 217207.

[98] Junjie Yang et al. “Spin jam induced by quantum fluctuations in a frustrated magnet”. In: *Proceedings of the National Academy of Sciences* 112.37 (2015), pp. 11519–11523.

[99] C L Henley. “Effective Hamiltonians and dilution effects in Kagome and related antiferromagnets”. In: *Canadian Journal of Physics* 79.11-12 (2001), pp. 1307–1321. eprint: https://doi.org/10.1139/p01-097.

[100] B. Canals and C. Lacroix. “Pyrochlore Antiferromagnet: A Three-Dimensional Quantum Spin Liquid”. In: *Phys. Rev. Lett.* 80 (13 Mar. 1998), pp. 2933–2936.

[101] Christopher L. Henley. “Publisher’s Note: Long-range order in the classical kagome antiferromagnet: Effective Hamiltonian approach [Phys. Rev. B 80, 180401(R) (2009)]”. In: *Phys. Rev. B* 80 (18 Nov. 2009), p. 189901.

[102] Anjana Samarakoon et al. “Aging, memory, and nonhierarchical energy landscape of spin jam”. In: *Proceedings of the National Academy of Sciences* 113.42 (2016), pp. 11806–11810.

[103] Junjie Yang et al. “Glassy Behavior and Isolated Spin Dimers in a New Frustrated Magnet BaCr9 p Ga12- 9 p O19”. In: *Journal of the Physical Society of Japan* 85.9 (2016), p. 094712.

[104] AM Samarakoon et al. “Scaling of memories and crossover in glassy magnets”. In: *Scientific reports* 7.1 (2017), pp. 1–8.

[105] Ik Klich, S-H Lee, and K Iida. “Glassiness and exotic entropy scaling induced by quantum fluctuations in a disorder-free frustrated magnet”. In: *Nature communications* 5.1 (2014), pp. 1–9.

[106] PH Conlon and JT Chalker. “Spin dynamics in pyrochlore Heisenberg antiferromagnets”. In: *Physical review letters* 102.23 (2009), p. 237206.

[107] Amit Keren. “Dynamical simulation of spins on kagomé and square lattices”. In: *Physical review letters* 72.20 (1994), p. 3254.

[108] Julien Robert et al. “Propagation and ghosts in the classical kagome antiferromagnet”. In: *Physical review letters* 101.11 (2008), p. 117207.

[109] Thomas Bilitewski, Mike E Zhitomirsky, and Roderich Moessner. “Dynamics and energy landscape of the jammed spin liquid”. In: *Physical Review B* 99.5 (2019), p. 054416.

[110] Preetha Saha et al. “Spin dynamics of the antiferromagnetic Heisenberg model on a kagome bilayer”. In: *Phys. Rev. B* 103 (22 2021), p. 224402.

[111] Takuya Arimori and Hikaru Kawamura. “Ordering of the antiferromagnetic Heisenberg model on a pyrochlore slab”. In: *Journal of the Physical Society of Japan* 70.12 (2001), pp. 3695–3707.

[112] Hikaru Kawamura and Takuya Arimori. “Chiral Kosterlitz-Thouless transition in the frustrated Heisenberg antiferromagnet on a pyrochlore slab”. In: *Physical review letters* 88.7 (2002), p. 077202.

[113] Arnab Sen, Kedar Damle, and Roderich Moessner. “Fractional Spin Textures in the Frustrated Magnet SrCr 9 p Ga 12- 9 p O 19”. In: *Physical review letters* 106.12 (2011), p. 127203.

[114] Arnab Sen, Kedar Damle, and R Moessner. “Vacancy-induced spin textures and their interactions in a classical spin liquid”. In: *Physical Review B* 86.20 (2012), p. 205134.

[115] PH Conlon and JT Chalker. “Absent pinch points and emergent clusters: further neighbor interactions in the pyrochlore Heisenberg antiferromagnet”. In: *Physical Review B* 81.22 (2010), p. 224413.

[116] Han Yan, Rico Pohle, Nic Shannon, et al. “Half moons are pinch points with dispersion”. In: *Physical Review B* 98.14 (2018), p. 140402.

[117] BI Halperin and PC Hohenberg. “Scaling laws for dynamic critical phenomena”. In: *Physical Review* 177.2 (1969), p. 952.

[118] Gerhard Müller. “Anomalous spin diffusion in classical heisenberg magnets”. In: *Physical review letters* 60.26 (1988), p. 2785.

[119] RW Gerling and DP Landau. “Spin-dynamics study of the classical ferromagnetic XY chain”. In: *Physical Review B* 41.10 (1990), p. 7139.

[120] RW Gerling and DP Landau. “Time-dependent behavior of classical spin chains at infinite temperature”. In: *Physical Review B* 42.13 (1990), p. 8214.

[121] V Constantoudis and Nikos Theodorakopoulos. “Nonlinear dynamics of classical Heisenberg chains”. In: *Physical Review E* 55.6 (1997), p. 7612.

[122] Debarshee Bagchi. “Spin diffusion in the one-dimensional classical Heisenberg model”. In: *Physical Review B* 87.7 (2013), p. 075133.

[123] D Forster. “Frontiers in Physics: Hydrodynamic Fluctuations, Broken Symmetry, and Correlation Functions”. In: *Reading: Benjamin Cummings* (1975).

[124] EF Shender et al. “Kagomé antiferromagnet with defects: Satisfaction, frustration, and spin folding in a random spin system”. In: *Physical review letters* 70.24 (1993), p. 3812.

[125] Peter Schiffer and István Daruka. “Two-population model for anomalous low-temperature magnetism in geometrically frustrated magnets”. In: *Physical Review B* 56.21 (1997), p. 13712.

[126] R Moessner and AJ Berlinsky. “Magnetic Susceptibility of Diluted Pyrochlore and SrCr 9-9 x Ga 3+ 9 x O 19 Antiferromagnets”. In: *Physical review letters* 83.16 (1999), p. 3293.

[127] L Limot et al. “Susceptibility and dilution effects of the kagomé bilayer geometrically frustrated network: A Ga NMR study of SrCr 9 p Ga 12- 9 p O 19”. In: *Physical Review B* 65.14 (2002), p. 144447.

[128] Richard G Palmer et al. “Models of hierarchically constrained dynamics for glassy relaxation”. In: *Physical Review Letters* 53.10 (1984), p. 958.

[129] Haim Sompolinsky and Annette Zippelius. “Relaxational dynamics of the Edwards-Anderson model and the mean-field theory of spin-glasses”. In: *Physical Review B* 25.11 (1982), p. 6860.

[130] Andrew T Ogielski. “Dynamics of three-dimensional Ising spin glasses in thermal equilibrium”. In: *Physical Review B* 32.11 (1985), p. 7384.

[131] H Pinkvos, A Kalk, and Ch Schwink. “Zero-field μSR measurements in CuMn and AuMn spin glasses interpreted in the frame of a fractal cluster model”. In: *Physical Review B* 41.1 (1990), p. 590.

[132] Amit Keren et al. “Probing the Spin-Spin Dynamical Autocorrelation Function in a Spin Glass above T g via Muon Spin Relaxation”. In: *Physical review letters* 77.7 (1996), p. 1386.

[133] Olivier Cepas and Benjamin Canals. “Heterogeneous freezing in a geometrically frustrated spin model without disorder: Spontaneous generation of two time scales”. In: *Physical Review B* 86.2 (2012), p. 024434.

[134] O Cépas. “Multiple time scales from hard local constraints: Glassiness without disorder”. In: *Physical Review B* 90.6 (2014), p. 064404.